A SUPERCOOLED MAGNETIC LIQUID STATE IN THE FRUSTRATED PYROCHLORE $DY_2TI_2O_7$

A Dissertation

Presented to the Faculty of the Graduate School

of Cornell University

in Partial Fulfillment of the Requirements for the Degree of

Doctor of Philosophy

by

Ethan Robert Kassner

May 2015

A SUPERCOOLED MAGNETIC LIQUID STATE IN THE FRUSTRATED PYROCHLORE $DY_2TI_2O_7$

Ethan Robert Kassner, Ph.D.

Cornell University 2015

A "supercooled" liquid forms when a liquid is cooled below its ordering temperature while avoiding a phase transition to a global ordered ground state. Upon further cooling its microscopic relaxation times diverge rapidly, and eventually the system becomes a glass that is non-ergodic on experimental timescales. Supercooled liquids exhibit a common set of characteristic phenomena: there is a broad peak in the specific heat below the ordering temperature; the complex dielectric function has a Kohlrausch-Williams-Watts (KWW) form in the time domain and a Havriliak-Negami (HN) form in the frequency domain; and the characteristic microscopic relaxation times diverge rapidly on a Vogel-Tamman-Fulcher (VTF) trajectory as the liquid approaches the glass transition.

The magnetic pyrochlore $Dy_2Ti_2O_7$ has attracted substantial recent attention as a potential host of deconfined magnetic Coulombic quasiparticles known as "monopoles". To study the dynamics of this material we introduce a high-precision, boundary-free experiment in which we study the time-domain and frequency-domain dynamics of toroidal $Dy_2Ti_2O_7$ samples. We show that the EMF resulting from internal field variations can be used to robustly test the predictions of different parametrizations of magnetization transport, and we find that HN relaxation *without monopole transport* provides a self-consistent description of our AC measurements. Furthermore, we find that KWW relaxation

provides an excellent parametrization of our DC time-domain measurements. Using these complementary measurement techniques, we show that the temperature dependence of the microscopic relaxation times in $Dy_2Ti_2O_7$ has a VTF form.

It follows that $Dy_2Ti_2O_7$, a crystalline material with very low structural disorder, hosts a supercooled *magnetic* liquid at low temperatures. The formation of such a state in a system without explicit disorder has become a subject of considerable theoretical interest. Recent numerical work suggests that the unconventional glassy magnetic dynamics in $Dy_2Ti_2O_7$ may result from interacting clusters of spins that evolve according to the general principles of Hierarchical Dynamics proposed 30 years ago. In the absence of disorder this may fall analytically into the realm of Many-Body Localization, a relatively new theory that is currently under intense development. $Dy_2Ti_2O_7$ could therefore push forward our understanding of the glass transition and bring together theories both old and new.

BIOGRAPHICAL SKETCH

Ethan Kassner was born in 1987 in Philadelphia, Pennsylvania, and was raised in the nearby suburb of Villanova. He attended the schools of the Lower Merion School District and graduated from Harriton High School in 2006. He then went to Princeton University, where he received his first exposure to physics research. After working for Lyman Page on the Atacama Cosmology Telescope (ACT) project and for Peter Meyers on dark matter detection experiments, Ethan joined the group of Ali Yazdani and found that he loved designing and analyzing condensed matter experiments. While working for the Yazdani lab, he completed a senior thesis that focused on superconducting transitions in thin aluminum films in different field orientations. After graduating from Princeton in 2010, Ethan moved to Ithaca and entered the physics Ph.D. program at Cornell University. He joined the lab of Séamus Davis in early 2011 and began working on experiments that examined solid helium; these experiments gave Ethan valuable experience that would prove very useful during his future projects. He then began developing experiments to measure the dynamics of frustrated magnets; the results of this work are the focus of this dissertation.

To my parents, without whom none of this would be possible.

ACKNOWLEDGEMENTS

I would first like to thank my advisor, Séamus Davis, for supporting my research and giving me the freedom to pursue the projects that I found most interesting. Séamus has a rare combination of intelligence, practical knowledge, and creativity, and when I talk to him I almost always learn something new about physics, experimental design, scientific writing, or the general philosophy of being a scientist. I must also thank Ethan Pratt and Vikram Gadagkar, who cheerfully taught me many things about low-temperature experiments after I joined the group. Despite my inexperience, Vikram was willing to give me serious responsibility during his experiments, and as a result I learned many things that would serve me well during my own projects. I also thank Azar Eyvazov and Ben Pichler for helping to run the dilution refrigerator during the last couple years. I have enjoyed my time in the Davis group in large part because of its friendly and collegial atmosphere, and this derives from my fantastic colleagues: Milan Allan, Stephen Edkins, Inês Firmo, Kazuhiro Fujita, Mohammad Hamidian, Andrey Kostin, Freek Massee, Sourin Mukhopadhyay, Jean-Philippe Reid, Andreas Rost, and Peter Sprau.

I have often utilized Cornell's exceptional facilities during my time here, and a few people in particular have frequently helped me over the past few years. Eric Smith made sure that liquid helium was in constant supply, and his vast knowledge of experimental techniques proved very useful when I ran into various problems during the development of my experiments. Nathan Ellis maintained an excellent student machine shop, and I thank him for patiently teaching me (sometimes repeatedly) how to properly use the many tools available there. Many of the parts for this project were manufactured in the department's professional machine shop, where Rodney Bowman gave me very helpful feedback

about my designs and Stanley McFall expertly made the parts. I also used various tools and the fume hood in the CCMR facilities, where Jon Shu and Steve Kriske have been very helpful over the past few years.

I am thankful for all my friends, who brought some semblance of balance to my life and who have made my time in Ithaca wonderful. I'm also grateful for my family, which has been a source of unending optimism and has always taken great interest in my pursuits. I cannot thank my parents enough for what they have done for me; they raised me well and encouraged me to follow my interests, and they have always been there for me when I needed advice and emotional support. I wouldn't have reached this point without them.

TABLE OF CONTENTS

LIST OF FIGURES

CHAPTER 1

SUPERCOOLED LIQUIDS AND THE GLASS TRANSITION

1.1 Supercooled Liquids

When a pure liquid is cooled to its freezing temperature T_m, it generally undergoes a first-order phase transition into a crystalline state with global ordering. This type of transition involves a latent heat, and there is a discontinuity in physical parameters such as the specific heat, entropy, and specific volume. However, this phase transition is not guaranteed to occur, since nucleation of the crystalline phase depends strongly on free energy differences and time. Below the freezing temperature, creation of a crystalline nucleus within a liquid phase involves two energy contributions: an energy cost from an effective surface tension due to configurational mismatches at the domain wall, and an energy gain from the lower free energy of the crystalline phase relative to the liquid phase [1]. In three dimensions we can therefore write the energy change from the establishment of a crystalline domain of radius R as $\Delta G(R) = \sigma R^2 - \delta g R^3$, where σ is a surface tension and δg is the difference in free energy density between the phases, $g_l - g_s$. The barrier to nucleation is maximized for a critical radius $R_c \propto \sigma/\delta g$, and we can treat this maximum $\Delta G(R_c)$ as the effective barrier that must be overcome for ordering to occur in a given liquid region. Since this is a thermally-activated process, the crystalline nucleation time will generally vary with an Arrhenius form $\tau_n = \tau_{n0} \exp(\Delta G(R_c)/k_B T)$. This time diverges at both the ordering temperature (where $\delta g = 0$) and in the limit $T \to 0$, so in general the nucleation time will have a minimum somewhere below T_m (Figure 1.1). The specific form of τ_n depends intimately on the details of the specific liquid under

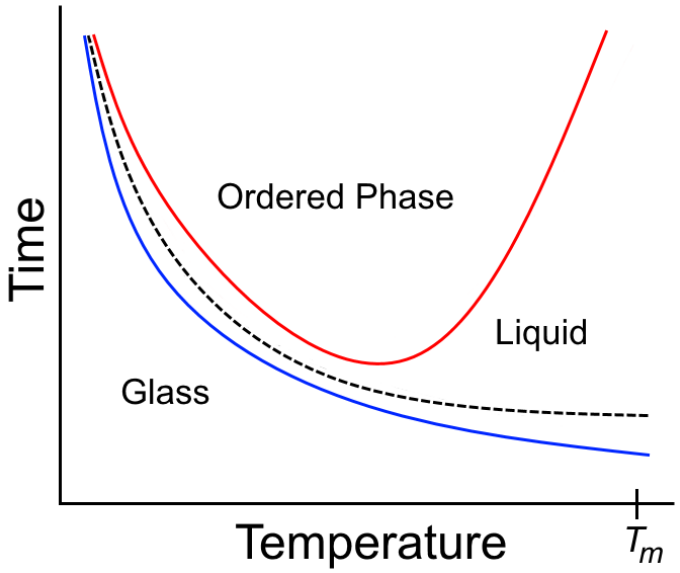

Figure 1.1: General behavior of the nucleation time (solid red curve) and microscopic relaxation time (solid blue curve) in a liquid. At temperatures below the ordering temperature T_m, a transition to a globally-ordered phase will occur after waiting for a long enough time, while a transition to an amorphous glass phase will eventually occur if cooling occurs rapidly. With a suitably-chosen cooling protocol (dashed line), the liquid phase can survive well below T_m. However, relaxation times begin to diverge quickly at low temperatures, and eventually it becomes practically impossible to avoid either a dynamical transition to an out-of-equilibrium glass state or a first-order transition to an ordered phase.

examination.

At temperatures well below T_m, correlations between the liquid components begin to substantially affect their behavior. The microscopic relaxation processes (e.g. shear relaxation rate) have relaxation times that increase rapidly at low temperatures; experiments indicate that this increase is generally sharper than the Arrhenius form $\tau = \tau_0 \exp(\Delta/k_B T)$ [2][3][4]. Once τ becomes larger than experimental timescales, the system can no longer explore its phase space during the course of an experiment; as a result, it undergoes a *dynamical* transition out of equilibrium and into a glass state, where it is constantly undergoing ultraslow relaxation and no longer follows the expectations of standard statis-

tical mechanics. This glass state is characterized by amorphous order that is effectively static on experimental timescales. However, glasses are constantly evolving with relaxation times that far exceed those of our observations. Time translation invariance no longer holds in this state [1]; parameter measurements (i.e. relaxations or correlations) that begin at a time t_0 and end at time t depend on t_0 in addition to $(t - t_0)$, leading to history dependence in measurements.

Since the nucleation time is enormous at T_m, there will in general be a temperature range in which the liquid can be cooled quickly enough to avoid crystallization, but slowly enough to remain ergodic (Figure 1.1). Under these conditions the system remains in a metastable state, and it remains disordered and retains many characteristics of the initial liquid; this is the "supercooled liquid" phase. The temperature range over which this can be achieved under feasible experimental cooling rates varies in different substances and container geometries, but a large variety of liquids have been successfully observed in the supercooled state [2][3][4].

1.2 Phenomenology of Supercooled Liquids

Supercooled liquids (also known as "glass-forming" liquids) have been studied for decades in a wide variety of materials, and over time it has become recognized that liquids in the supercooled regime exhibit a common set of phenomena [1][2][3][4][5][6]. One such phenomenon is a broad peak in the specific heat C_p a bit below T_m (Figure 1.2A); this peak is expected from general thermodynamic considerations. As a liquid enters the supercooled state it retains a heat capacity similar to the high-temperature liquid value; it therefore has

a higher heat capacity than the ordered state and loses entropy more quickly with decreasing temperature. If this were to continue indefinitely down to very low temperatures, below a "Kauzmann temperature" T_K the supercooled liquid state would have a lower entropy than the global ordered state. In 1948 Kauzmann noted that many liquids have specific heats that, when extrapolated, give a non-zero T_K [7]. To avoid this entropy crisis, a liquid can be expected to transition into a glass state at a temperature $T_g > T_K$; in this state the heat capacity is similar to its value in the ordered phase, and therefore between T_m and T_g there is generally a peak in C_p.

The microscopic relaxation times $\tau(T)$ of glass-forming liquids also diverge more rapidly than would generally be expected from simple thermally-activated systems. Instead of following a simple Arrhenius form $\tau = \tau_0 \exp(\Delta/k_B T)$ with some activation energy Δ, supercooled liquids genenerally have relaxation times that follow a Vogel-Tamman-Fulcher (VTF) trajectory [1][2][3] given by

$$\tau = \tau_0 \exp\left(\frac{DT_0}{T - T_0}\right) \tag{1.1}$$

where T_0 is a temperature at which the relaxation time diverges and D characterizes the "fragility" of the liquid. This behavior is depicted in Figure 1.2B. Values of D around 100 or above characterize "strong" liquids that show little deviation from Arrhenius behavior, while lower values around 10 or less are typical of "fragile" liquids that demonstrate a large divergence from standard thermally-activated behavior. This fragility of the supercooled state has been characterized for a large number of materials [3]. Measurements on a variety of liquids indicate that the VTF divergence temperature T_0 and the entropy crisis temperature T_K are similar: $T_K \approx T_0$ [1]. These results come from independent techniques, and they suggest strongly that these temperatures characterize a

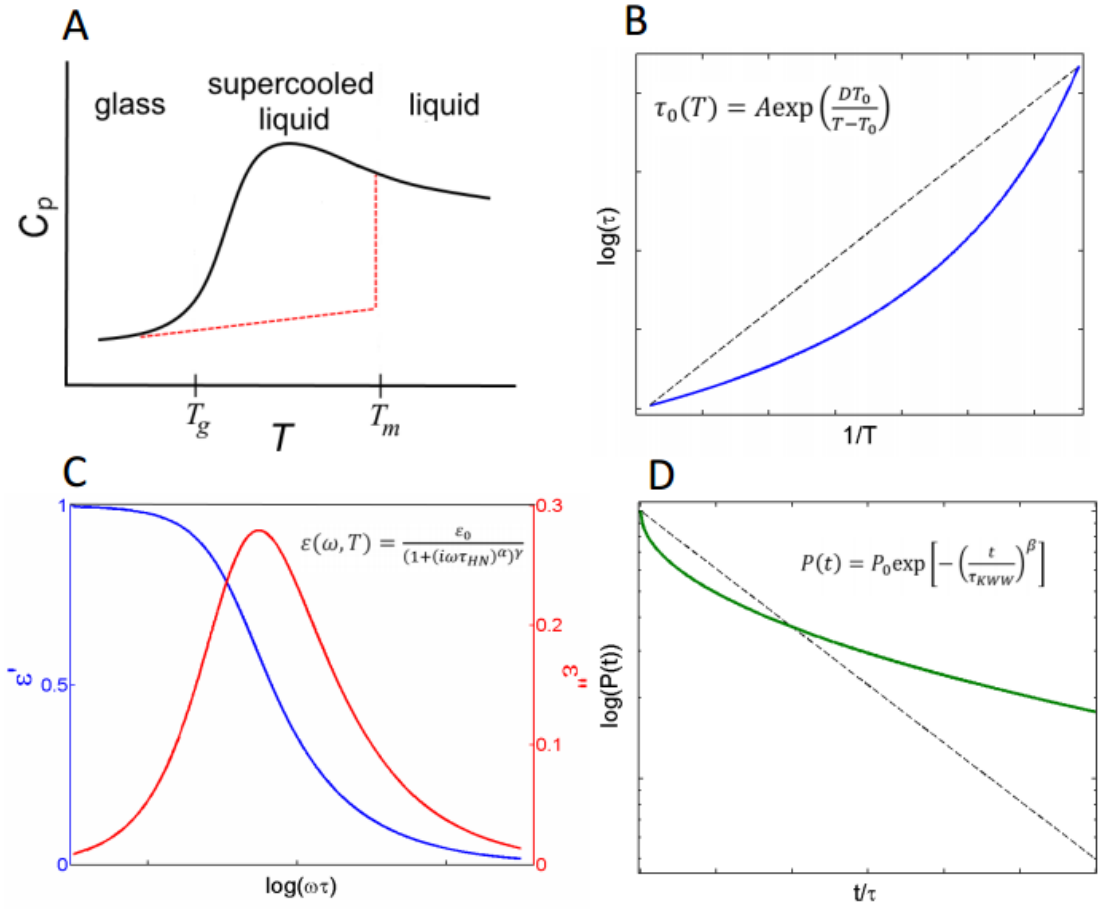

Figure 1.2: Despite being characterized in a wide variety of substances, supercooled liquids have several things in common. **(A)** There is generally a broad peak in the specific heat below the ordering temperature T_m and above the glass transition temperature T_g. This peak prevents the liquid from having a negative entropy at low temperatures. **(B)** Microscopic relaxation times do not increase according to a standard Arrenius form (dashed line) as the temperature decreases; instead they increase along a super-Arrhenius trajectory given by the VTF parametrization (blue). **(C)** The complex dielectric relaxation has a HN form in frequency space; here we show typical behavior of Re[$\epsilon(\omega)$] (blue) and Im[$\epsilon(\omega)$] (red). **(D)** The time-domain relaxation of physical parameters (such as the polarization $P(t)$) typically shows stretched-exponential KWW relaxation (green) rather than a simple Debye relaxation (dashed line).

real lower bound on the temperature by which a liquid must either undergo a phase transition into an ordered phase or a dynamical transition into a glass state.

We can determine microscopic relaxation times by measuring complex relaxation in the time and frequency domains. In the frequency domain (Figure 1.2C), supercooled liquids typically have dielectric functions $\epsilon(\omega, T)$ that follow a Havriliak-Negami (HN) parametrization [8]:

$$\epsilon(\omega, T) = \epsilon_\infty + \frac{\epsilon_0}{(1 + (i\omega\tau_{HN})^\alpha)^\gamma} \tag{1.2}$$

where ϵ_0 is a relaxation amplitude, τ_{HN} is a characteristic microscopic relaxation time, and the exponents α and γ describe the width and asymmetry, respectively, of the relaxation in frequency space. ϵ_∞ is a purely-real quantity that gives the relaxation in the $\omega \to \infty$ limit; it is expected to be non-zero due to the non-instantaneous heat transfer between dipoles and the lattice on which they lie [9]. This parametrization is a generalization of the simplest relaxation forms: $\alpha = \gamma = 1$ yields Debye relaxation, $\alpha = 1$ yields Davidson-Cole relaxation [10], and $\gamma = 1$ yields Cole-Cole relaxation [11]. Glass-forming liquids typically have $\alpha < 1$, $\gamma < 1$ [12], indicating the presence of a complex landscape of excitations and dynamics; typical relaxation behavior is shown in Figure 1.2C.

Supercooled liquids also show unconventional relaxation in the time domain (Figure 1.2D) that typically takes a Kohlrausch-Williams-Watts (KWW) form given by [13]

$$Q(t) = Q_0 \exp\left[-\left(\frac{t}{\tau_{KWW}}\right)^\beta\right] \tag{1.3}$$

where $Q(t)$ is some quantity (e.g. polarization), τ_{KWW} is a relaxation time, and β is a "stretching" exponent. $\beta = 1$ corresponds to simple Debye relaxation with a single relaxation time for the entire material, while $\beta < 1$ ("stretched exponen-

tial" relaxation) indicates the presence of more complex dynamics. Supercooled liquids generally exhibit the latter type of behavior [2]. Although the KWW function has no analytical Fourier transform, it has been known for decades that the time-domain KWW and frequency-domain HN parametrizations are numerically equivalent and describe the same microscopic phenomena. The full relaxation functions can be written as sums of simpler relaxations with a distribution of relaxation times $G(\ln\tau)$:

$$\exp\left[-\left(\frac{t}{\tau_{KWW}}\right)^{\beta}\right] = \int_0^\infty \exp\left(-\frac{t}{\tau}\right) G(\ln\tau) d(\ln\tau) \tag{1.4}$$
$$\frac{1}{(1+(i\omega\tau_{HN})^{\alpha})^{\gamma}} = \int_0^\infty \frac{1}{1+i\omega\tau} G(\ln\tau) d(\ln\tau)$$

The distribution G can be calculated from relaxation in one domain and then used to calculate the relaxation in the other domain, allowing us to directly find the KWW and HN parameters that give self-consistent relaxation time distributions. This procedure yields the following connections between the two parametrizations [14]:

$$\ln\left(\frac{\tau_{HN}}{\tau_{KWW}}\right) = 2.6(1-\beta)^{0.5}\exp(-3\beta) \tag{1.5}$$
$$\alpha\gamma = \beta^{1.23}$$

We can therefore utilize time-domain and frequency-domain measurements as complementary probes of a single set of microscopic phenomena. This HN/KWW characterization has been used extensively to identify glass-forming liquids [1][2][4][5][6].

1.3 Spin Glasses

Glassiness in the context of magnetic systems began receiving substantial attention in the 1970s and 1980s, when many "spin glasses" were discovered and characterized. An excellent overview of the field can be found in [15]. Spin glass materials contain magnetic moments, but they do not transition to a magnetically-ordered state at low temperatures. Instead their moments remain disordered, and below a "freezing temperature" T_f they exhibit history dependence indicative of a glass state. This behavior was first discovered in dilute magnetically-doped metallic alloys (e.g. Mn-doped Cu and Fe-doped Au), but spin glass properties have also been observed in several doped insulators.

Despite the diversity of materials that can behave as spin glasses, there are several phenomenological features that seem to uniquely identify this state. First, the real part of the complex susceptibility $\chi'(\omega, T)$ has a cusp as the temperature is varied; typical behavior in CuMn [16] is shown in Figure 1.3. These data have two characteristics commonly observed in spin glasses: the spin glass maxima in χ' are generally sharp, and the maxima are quite symmetric when plotted against temperature. The temperature at which χ' reaches its maximum can be regarded as a freezing temperature T_f. The onset of freezing can also be demonstrated by examining the sample magnetization as a function of field and temperature. Above T_f zero-field-cooled (ZFC) samples and field-cooled (FC) samples yield the same magnetization; however, this equivalence is broken below T_f (where the sample likely falls out of equilibrium), and results at lower temperatures depend on the sample history. Figure 1.4 shows history-dependent behavior of the static susceptibility (which is proportional to the magnetization) observed in CuMn [17]; ZFC samples exhibit the typical spin

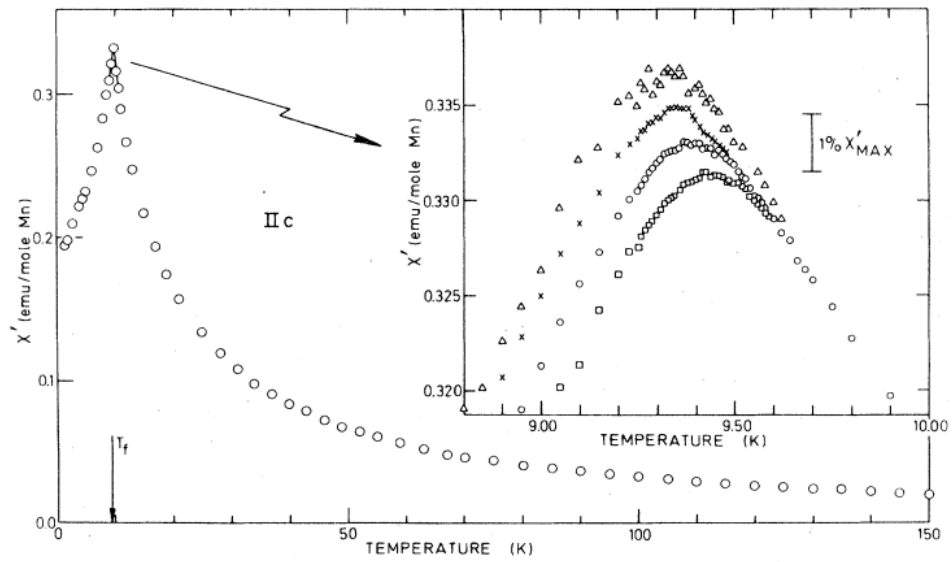

Figure 1.3: Real part of the zero-field magnetic susceptibility measured at 234 Hz. The susceptibility reaches a maximum at a sharp cusp at ~ 5 K; the sharpness of this feature is typical of spin glasses. Inset: behavior of the susceptiblity in the vicinity of the maximum at 2.6 Hz (triangles), 104 Hz (crosses), 234 Hz (circles), and 1.33 kHz (squares). Figure from [16].

glass maximum in χ', but below $T_f \approx 15$ K very little temperature dependence is observed in FC samples. This indicates that the sample may fall out of equilibrium and enter a dynamical glass state at these lower temperatures. The freezing temperature generally depends rather strongly on the applied field, with higher fields suppressing freezing behavior and decreasing T_f [15].

The dissipative susceptibility component $\chi''(\omega, T)$ reveals more similarities in the diverse spin glass population. χ'' in spin glasses typically shows a single-peaked behavior, indicating the presence of some characteristic central relaxation time. However, the peak widths are usually very large, with χ'' typically spanning many decades in frequency [18][19][20]; this indicates that there is an extremely broad distribution of relaxation times and dynamics in these systems. Figure 1.5 shows a typical example of this behavior. χ'' is also generally much smaller (by ~ an order of magnitude or more) than χ'.

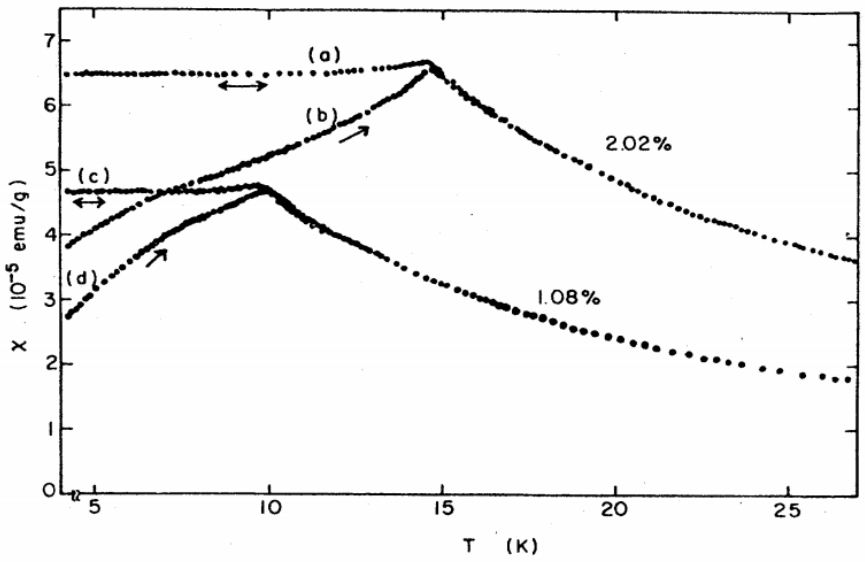

Figure 1.4: Static susceptibility of CuMn at two different doping concentrations in an applied field of 5.90 G. The susceptibility of the ZFC samples show the typical sharp spin glass maximum at T_f. However, FC samples have magnetizations that depend very weakly on temperature below T_f, indicating the onset of history dependence in the measurements. Figure from [17].

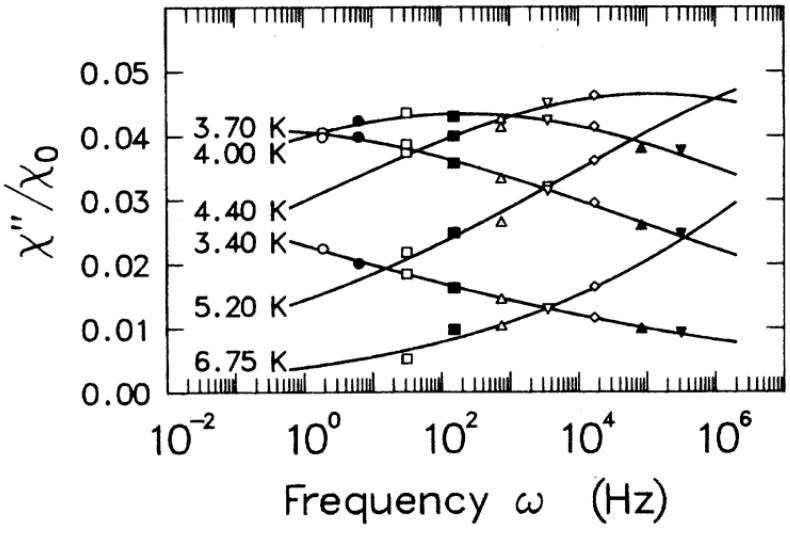

Figure 1.5: Frequency dependence of the dissipative susceptibility component χ'' in the spin glass Rb_2CuCoF at several temperatures just above $T_f \approx 3.4$ K. The peaks in χ'' span many decades of frequency, suggesting the existence of an enormous (~ 10 decades wide) distribution of relaxation times in the system. Figure from [20].

All these characteristics of spin glass materials will prove very useful when discussing the unconventional magnetism present in $Dy_2Ti_2O_7$. Spin glasses were some of the first magnetic systems known to resist ordering down to temperatures far below the Curie-Weiss temperature T_{cw} predicted from high-temperature measurements, and their microscopic origins in structural disorder are fairly well-understood (Section 1.4). This will make them very useful for comparisons when we characterize the behavior observed in our own experiments.

1.4 Theory of the Glass Transition

Universal understanding of the glass transition remains even today a prominent outstanding problem in physics [21]. Theories of glasses and their antecedent supercooled liquids tend to focus on "frustration", the inability of a single favored ordering configuration to cover an entire sample space. In the case of structural glasses, it has been proposed that glasses can form because the local ground state arrangements of mobile liquid particles cannot cover the sample space [6]. If crystalline nucleation (which can in theory tile the entire space) fails to occur, then the geometrical frustration of the liquid state favors amorphous order that can be analyzed using the interactions of defects present between regions of different local order.

For magnetic materials, theory has focused on the role of disorder in spin glasses [15]. Spin glass theories incorporate disorder via random interactions of the form $-\sum_{ij} J_{ij}\mathbf{S}_i \cdot \mathbf{S}_j$, where the exchange interactions J_{ij} are random and the $\mathbf{S}_i$ can be Ising or Heisenberg spins [15][22]. In principle the J_{ij} can vary over

long times as atoms migrate in the lattice, but on the timescales of spin fluctuations the spin exchange interactions are effectively a constant random set $\{J_{ij}\}$; there is "quenched disorder" in a spin glass. Evidence for such disorder has been found from fits of the measured magnetic susceptibility to thermodynamic calculations; deviations from Curie-Weiss behavior as temperatures near the freezing temperature can be described by exchange interactions $J(r)$ that are ferromagnetic or antiferromagnetic, depending on the distance r between moments [23]. Interaction randomness in crystalline spin glasses (dilute alloys and concentrated insulators) derives from the random positioning of dopants within the bulk material, while for other spin glass materials this disorder likely derives from a lack of crystalline order. In the presence of both ferromagnetic ($J_{ij} > 0$) and antiferromagnetic ($J_{ij} < 0$) interactions of comparable strength, no single ordered magnetic ground state can tile the entire sample, and cooling produces an amorphous glassy state.

In recent years there has been a flurry of theoretical work on the behavior of many-body systems in the presence of disorder; one theory that has become increasingly prominent is that of Many Body Localization (MBL) [24][25], which builds off of Anderson's work on the localization of single-particle wavefunctions in a disordered lattice [26]. Anderson considered the behavior of single-particle wavefunctions that evolve in a Hamiltonian of the following form:

$$H = \sum_i E_i c_i^\dagger c_i + \sum_{i \neq j} V_{ij} c_j^\dagger c_i \tag{1.6}$$

where $c^\dagger$ and c are creation and annihilation operators and the on-site energies $\{E_i\}$ are random with a probability distribution of characteristic width W. The "hopping" terms V_{ij} may or may not be similarly random. A high-enough level of randomness in E_i reduces the states available near any site i for transport,

and as long as the hopping strength V is small compared to W a particle can maintain a probability distribution localized near its initial lattice site, even in the $t \to \infty$ limit. In this case no global transport or diffusion takes place.

MBL generalizes this approach to many-body states, often with quenched disorder in the spirit of spin glass theories [25]. However, some MBL studies have examined the theory in the context of systems without explicit structural or interaction disorder. In these cases the effective disorder necessary for localization comes from heterogeneous initial conditions, for example in on-site occupations $\{n_i\}$ that give different initial energies $\{E_i\}$ according to a function $E(n)$ that is the same for all sites. The many-body configuration states $|n\rangle = |n_1 n_2 ... n_N\rangle$ in these systems can evolve in Hamiltonians of the form

$$H = \sum_{i=1}^{N} \left[E_i(n_i) + \sum_{i \sim j} J b_i^\dagger b_j \right] \tag{1.7}$$

where $b^\dagger$ and b are bosonic creation and annihilation operators and $n_i = b_i^\dagger b_i$ is a number operator. If $E(n_i)$ is non-linear in n and J is suitably weak, the probability of nearby sites having energy differences smaller than the hopping interaction can become small. Examining the possibility of localization in such a system then becomes equivalent to determining if in the large-N limit the number of degenerate states is small enough that states in different parts of the lattice remain disconnected. The possibility of such a path to glassiness in general ordered environments is still unsettled [24][25], but some groups have shown that localization may be possible in a particular stochastic spin model with nearest-neighbor interactions [27] and in systems containing fast- and slow-moving particles [28][29]. In the latter models, configurations of slow-moving particles provide effective randomized potentials that may generate very large or divergent relaxation times.

Though the translationally-invariant problem remains unsettled analytically, it can also be tackled via numerical dynamics simulations. Chakraborty *et al.* showed in principle that some glassy relaxation signatures, such as a VTF-like relaxation time, can be found in a frustrated model on a hexagonal lattice [30]. However, their rather artificial interaction model makes it difficult to translate their results to realistic frustrated magnetic systems. Recently a more evocative and intuitive investigation [31] was performed by using general principles introduced 30 years ago for "Hierarchically Constrained Dynamics" [32]. This theory proposes that liquids can evolve dynamically into glasses under two general conditions: (1) there are different levels (hierarchies) of relaxation with different characteristic timescales, and (2) these hierarchies are connected dynamically by constraints. Cépas and Canals incorporated these principles by studying frustrated spin systems on a kagome lattice and utilizing spin-flip probabilities that depend on the number of connected spins being flipped [31]. This work found stretched-exponential relaxation and persistent spin configuration heterogeneity in a system that was otherwise without any disorder; it therefore seems that this plan of action could be a promising way to attack the problem of glassiness on an ordered lattice. We will return to this work later in the context of $Dy_2Ti_2O_7$.

CHAPTER 2

SPIN ICE AND DYNAMICS IN $DY_2TI_2O_7$

2.1 Structure and the ground state

Much of the fascinating physics of $Dy_2Ti_2O_7$ (DTO) derives from its geometry and the anisotropic behavior of its large Dy^{3+} magnetic moments. DTO has a pyrochlore structure [33], which gets its name from an eponymous mineral (chemical formula $NaCaNbTaO_6F$) that turns green when exposed to fire. This structure consists of distinct interpenetrating sublattices of corner-sharing equilateral tetrahedra whose centers lie on diamond lattice sites (Figure 2.1); one lattice holds the highly magnetic Dy^{3+} ions, while the other lattice hosts nonmagnetic Ti^{4+} ions that do not contribute to the magnetism of the material [34]. Oxygen atoms are positioned anisotropically around the Dy^{3+} ions with distorted bond lengths. The sublattices can also be visualized as alternating 2D trigonal and kagome layers. The nearest-neighbor distance between moments is $a = 3.58$ Å, and the distance between tetrahedra centers is the diamond lattice constant $a_d = \sqrt{3/2}a = 4.38$ Å [35].

High-temperature fits of the magnetic susceptibility to a Curie-Weiss law (for example, [36] and [37]) imply that Dy^{3+} has a large angular momentum $J = 15/2$. This ordinarily would imply a 16-fold degeneracy in the angular momentum ground states in zero applied field, but magnetocaloric [38] and spectroscopic neutron scattering [39] studies have found that the Dy^{3+} ions instead have a ground-state doublet $|15/2, \pm 15/2\rangle$, and along the local [111] directions these ground states lie ~ 400 K below the excited J states [39]. DTO moments therefore experience a very strong anisotropy, and each Dy^{3+} moment is effec-

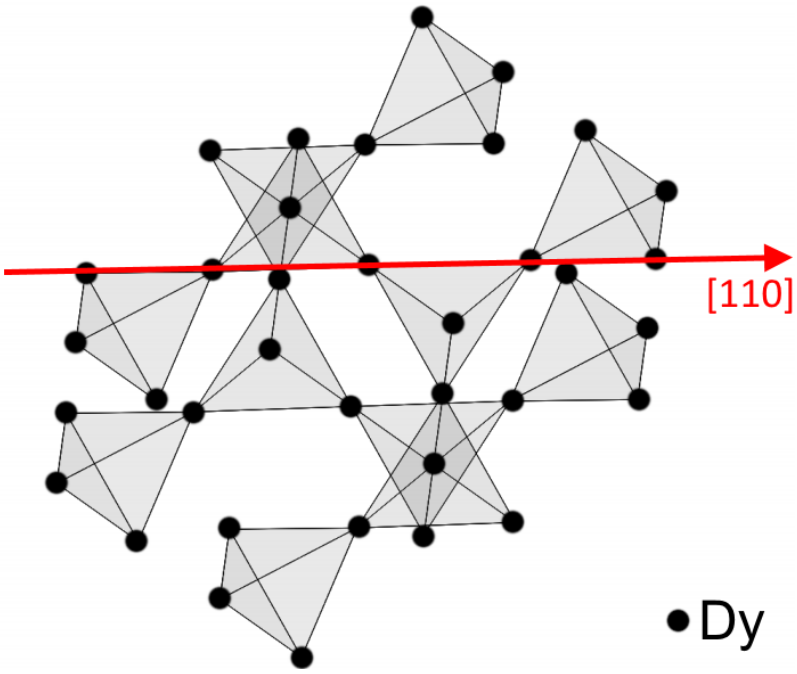

Figure 2.1: The Dy^{3+} moments (black circles) in DTO lie on the vertices of corner-sharing tetrahedra; Ti^{4+} ions lie on a similar interpenetrating lattice but play no significant role in the magnetism of the material. A large crystal field anisotropy forces the moments to point along their local [111] directions, toward or away from the centers of the tetrahedra on which they lie.

tively an Ising spin of size $\mu = g_J J \mu_B \approx 10\mu_B$ that points toward or away from a tetrahedron center.

Despite the presence of these large moments, no low-temperature long-range ordering has been observed in DTO. At high temperatures ($T >\sim 15$ K), magnetic susceptibility measurements on single crystals of DTO find that $\chi(T)$ has a Curie-Weiss form consistent with localized Dy^{3+} moments $\mu = 10\mu_B$ and a ferromagnetic ordering temperature $T_{cw} \approx 1.2$ K [36]. However, no transition to ferromagnetic order is observed even at temperatures well below T_{cw}. In a conventional magnetic system, we would expect a sharp peak in the heat capacity at T_{cw} due to the large magnetic entropy change of the ordering transition. In DTO many groups have instead measured a broad peak in C_p with a maximum at

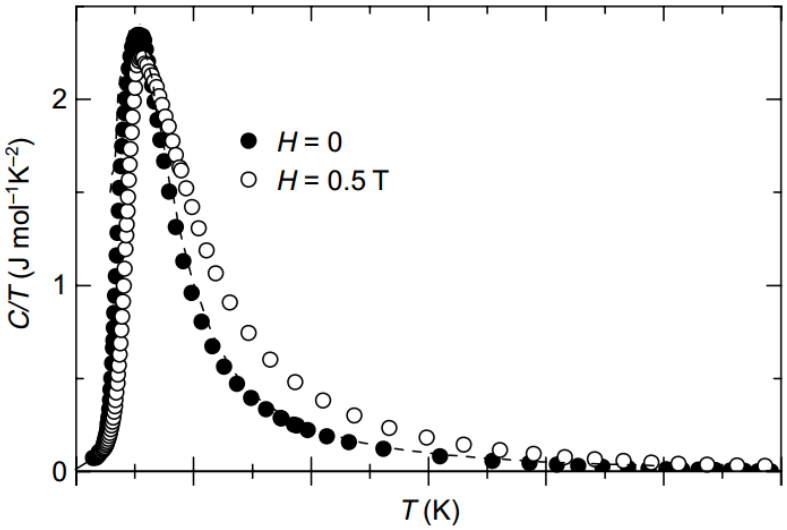

Figure 2.2: Heat capacity measured in a powder sample of DTO; similar data have been measured in single-crystal samples. There is a broad peak in C/T at $\sim$ 1.1 K that is not accompanied by any magnetic ordering transition. Figure from [40].

$T \sim 1.1$ K [40][41][42][43][44]. Figure 2.2 shows results typical of these thermal measurements. Despite the presence of this peak, neutron scattering studies [45][46] have not observed any magnetic Bragg spot behavior associated with long-range ordering; the C_p behavior is associated with no magnetic phase transition despite its proximity to the predicted ordering temperature T_{cw}.

To account for this behavior we must consider dipole interactions in addition to the standard magnetic exchange. Since DTO contains ions with large magnetic moments, both dipole and exchange interactions contribute to the overall magnetism of the system. The result $T_{cw} > 0$ implies that the combined nearest-neighbor interactions have a ferromagnetic form $-J_{eff} \sum \mathbf{S}_i \cdot \mathbf{S}_j$, $J_{eff} > 0$; we will consider J_{eff} in more detail in Section 2.3. Given the anisotropic constraints on the moments, this imposes ground state configurations in which each pyrochlore tetrahedron has two moments pointing toward its center and two moments pointing away from its center. There are six such states for each tetra-

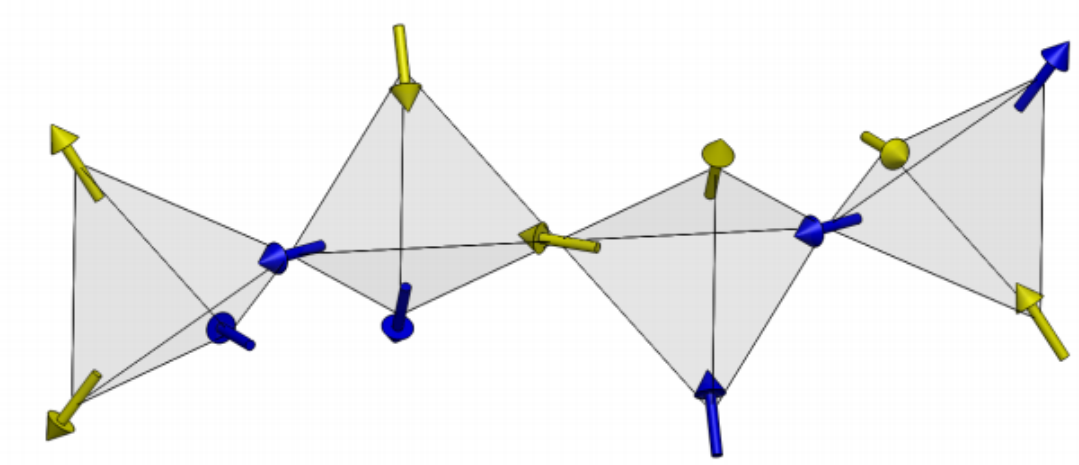

Figure 2.3: A configuration of four neighboring DTO tetrahedra that satisfies the Bernal-Fowler rules for the magnetic ground states. Each tetrahedron has two spins pointing toward its center and two spins pointing away from its center.

hedron; one configuration that satisfies these constraints for four tetrahdedra is shown in Figure 2.3. These rules map directly onto the Bernal-Fowler rules for asymmetric hydrogen bonding in water ice, where each oxygen atom has four nearest neighbors with which it shares hydrogen bonds. The lowest-energy ice configurations have two hydrogens close to and two hydrogens away from each oxygen [47].

In the 1930s Pauling calculated an expected "residual entropy" for water ice by counting the states allowed by the Bernal-Fowler rules [47]. In water ice, each oxygen is surrounded tetrahedrally by 4 other oxygen atoms, and therefore for each oxygen there are 16 possible bond configurations of which only 6 satisfy the ice rules. Each bond is shared between two oxygens, so the number of ground state configurations for N_t oxygen atoms is

$$\Omega = \left(2^2 \cdot \frac{6}{16}\right)^{N_t} = \left(\frac{3}{2}\right)^{N_b/2}$$

where $N_b = 2N_t$ is the total number of bonds. Therefore, the residual entropy

per hydrogen bond is expected to be

$$S_{pauling} = \frac{1}{N_b} k_B \ln \Omega = \frac{k_B}{2} \ln\left(\frac{3}{2}\right)$$

This elegant calculation is within a couple percent of the actual value deduced from differences between the entropy calculated from spectroscopic measurements and the entropy calculated via integration of the heat capacity [48].

Experiments on DTO have accessed an effective residual entropy using a similar strategy adapted for a magnetic system. Applying Pauling's calculation to the spins in the DTO ground states yields an entropy *per spin* given by the ice result:

$$S_{pauling} = \frac{1}{N_s} k_B \ln \Omega = \frac{k_B}{2} \ln\left(\frac{3}{2}\right)$$

which is ~ 0.3 times the expected high-temperature spin entropy $S/N = k_B \ln 2$. In DTO any residual entropy can be found from the difference between the entropy calculated from heat capacity measurements and the high-temperature zero-field entropy value for Ising spins, $S/N = k_B \ln 2$. In 1999 Ramirez *et al.* found that integrating the measured DTO heat capacity from 0.2 K to 12 K did not yield the expected molar entropy value $\int C/T dT = R \ln 2$; the result was smaller by an amount within 5% of the Pauling value [40]. This finding, shown in Figure 2.4, indicates that the ground states of DTO, a magnetic system, can be mapped directly onto those of water ice. For this reason DTO is known as a "spin ice".

Further evidence for the "2-in, 2-out" ground states has been provided by neutron scattering measurements. The expected structure factor for such divergence-free conditions has been worked out in various contexts [49][50]. Larger values of the magnetization $|\mathbf{M}|$ can be satisfied by fewer spin configurations, so increasing $|\mathbf{M}|$ carries an entropy cost. The zero-field free energy can be

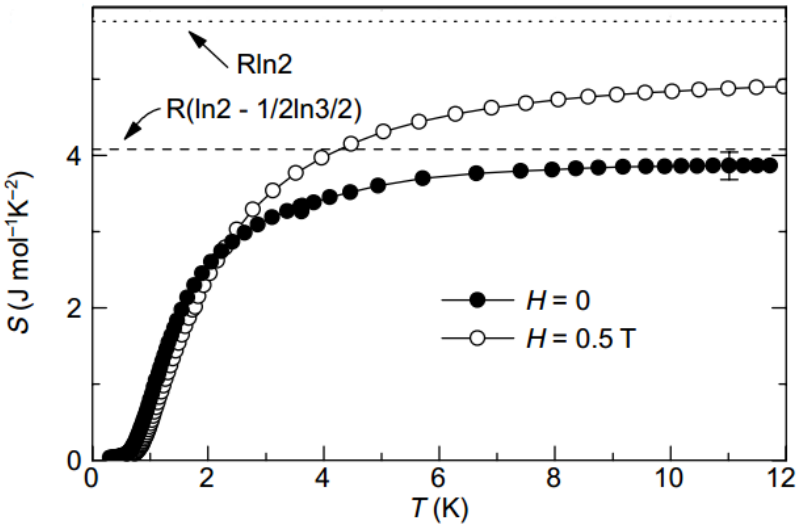

Figure 2.4: Entropy calculated from low-temperature measurements of the heat capacity in DTO. The integrated entropy is smaller than the generic high-temperature Ising expectation by an amount close to the Pauling water ice entropy; this indicates that the Bernal-Fowler ice rules are applicable to DTO magnetic ground states. Figure from [40].

expressed as a functional of $|\mathbf{M}|$:

$$F[|\mathbf{M}(\mathbf{r})|] = \frac{k_B T}{V} \int d^3\mathbf{r} \frac{1}{2} K |\mathbf{M}(\mathbf{r})|^2$$
$$F[|\mathbf{M}(\mathbf{k})|] = k_B T \int d^3\mathbf{k} \frac{1}{2} K |\mathbf{M}(\mathbf{k})|^2 \tag{2.1}$$

where V is the volume and K is some effective "stiffness". The probability of a particular magnetization is proportional to $\exp(-F(M)/k_B T)$, so in reciprocal space we naïvely expect $\left\langle M_\mu(-\mathbf{k}) M_\nu(\mathbf{k}) \right\rangle = \delta_{\mu\nu}/K$, where μ and ν are Cartesian coordinates. However, the Bernal-Fowler rules effectively impose a $\nabla \cdot \mathbf{M} = 0$ constraint on the magnetization; this means that in reciprocal space $\mathbf{k} \cdot \mathbf{M}(\mathbf{k}) = 0$, so the magnetization must be orthogonal to $\mathbf{k}$. Projecting out the components parallel to $\mathbf{k}$ leads to the full prediction for the magnetization correlations:

$$\left\langle M_\mu(-\mathbf{k}) M_\nu(\mathbf{k}) \right\rangle = \frac{1}{K} \left[\delta_{\mu\nu} - \frac{k_\mu k_\nu}{|\mathbf{k}|^2} \right] \tag{2.2}$$

which should yield "pinch points" in the structure factor [49][51]. These pinch

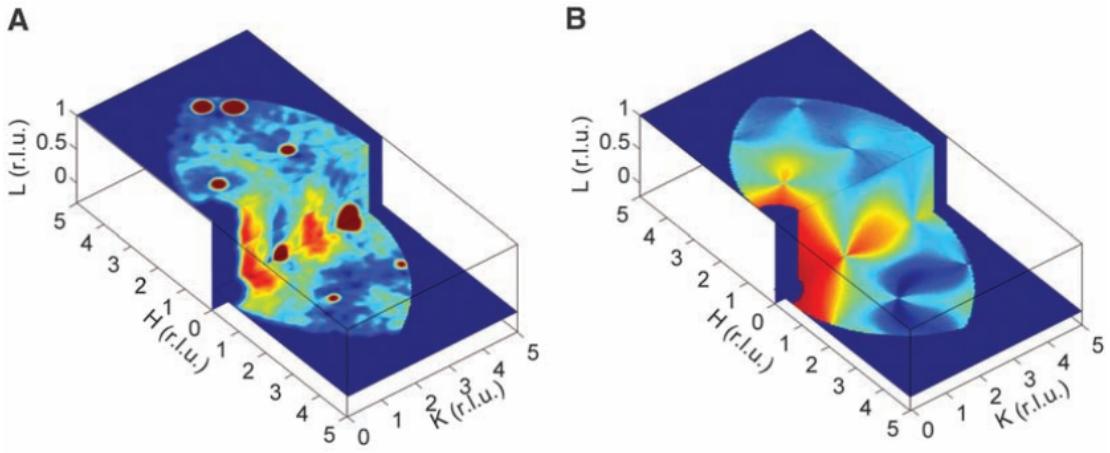

Figure 2.5: **(A)** Observed scattering intensity of zero-field polarized neutron scattering in DTO. The dark red spots are Bragg peaks unrelated to the magnetic correlations. A "pinch point" is apparent in the scattering intensity, revealing the presence of dipolar correlations. These data are in very good agreement with **(B)** calculations performed by applying the correlations of Equation (2.2) to the highly-anisotropic DTO moments. Figure from [41].

points have indeed been observed in DTO [41] (Figure 2.5), providing further evidence that the ground states are described by Bernal-Fowler ice configurations.

Numerical simulations have predicted that the spin ice degeneracy should be broken at around 180 mK, where a first-order transition occurs to an ordered state that can be characterized by a uniform magnetic ordering vector and an ordering parameter [52]. These simulations, which utilized synchronized flips of spin loops in addition to single spin flips, also found that the nature of the predicted transition was independent of the nearest-neighbor exchange interaction strength, indicating that it is driven by long-range dipolar interactions. However, no such transition at $T \approx 200$ mK has been observed so far; magnetic susceptibility [36] and μSR measurements [53] have observed no onset of magnetic ordering down to 50 mK (Figure 2.6).

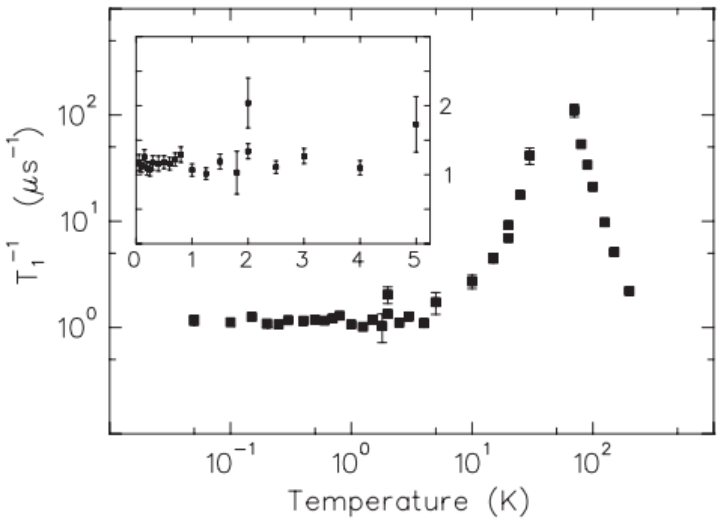

Figure 2.6: Relaxation rate of muons injected into DTO at low temperatures in zero field. The relaxation rate remains flat below 5 K, and there is no indication of the ordering transition predicted to occur at 180 mK. Figure from [53].

Several groups have postulated that this apparent absence of ordering could be due to microscopic relaxation times that become larger than typical experimental timescales at low temperatures. If this were the case, low-temperature observations on short timescales would observe out-of-equilibrium glass properties instead of a transition to an ordered ground state. This was recently tested by thermal measurements that sat at stable temperatures for as long as several days [44]; the results of these very-long-time observations are shown in Figure 2.7. These measurements are consistent with other measurements of the heat capacity [40][41][42][43] above ~ 0.6 K, but below this temperature the ultralong waits revealed new thermal features. The beginnings of what could be a new low-temperature peak in C_p became apparent below ~ 0.5 K, and integration of these results gave a residual entropy that was lower than the Pauling result and showed no signs of stabilizing at a non-zero value.

Crucially, the authors in [44] performed the same analysis on only the first 600 seconds of their thermal relaxation data and found that their early-time re-

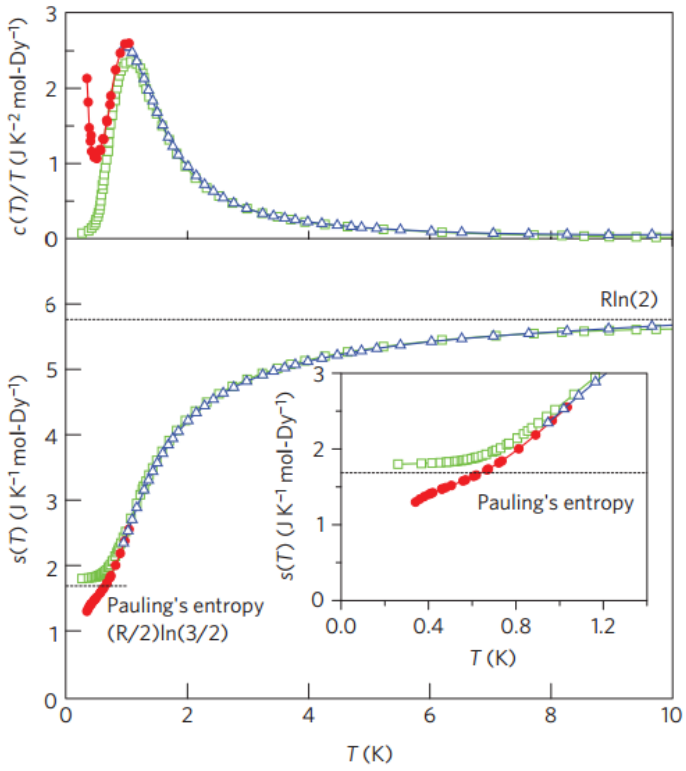

Figure 2.7: Comparison of long-time thermal measurements performed for up to ~ 100 hrs (red circles, [44]) with the results of other heat capacity measurements (green squares, [40]; blue triangles, [42]) performed on shorter timescales. The ultra-long measurements reveal new features in the heat capacity below ~ 0.6 K; C/T begins to increase sharply below 0.5 K, and integration of these new features yields an entropy that no longer stabilizes at the Pauling ice value. Figure from [44].

sults were in line with previous studies. This shows that the microscopic relaxation times of DTO become very large below ~ 600 mK, but nevertheless the system continuously evolves toward some equilibrium state. These large relaxation times can explain the lack of ordering features in neutron scattering and μSR measurements, which take place on much shorter timescales than thermal measurements. The low-temperature measurements of DTO are all consistent with diverging relaxation times that make dynamical glass transitions increasingly likely below ~ 0.6 K.

The approach to a dynamical glass phase can be examined by measuring the history dependence of a sample's magnetization; this was an important strategy during investigations of the spin glasses (Figure 1.4). Field-cooling experiments have demonstrated such history dependence in the magnetization of DTO below ~ 0.6 K (Figure 2.8), indicating that sample equilibration becomes very difficult below this temperature [37]. This is consistent with the observation of discrepancies in thermal relaxation measurements below 0.6 K [44]. The freezing temperature T_f, where the magnetization history dependence begins, is very weakly dependent on the applied field. In fact, T_f actually *increases* slightly with the applied field, in stark contrast to the strong decreasing response of T_f in spin glasses (Section 1.3).

It is important to note that the degenerate spin ice description only holds in low applied magnetic fields, where the Zeeman energy is too small to lift the ground state degeneracy. In higher fields DTO can transition into a variety of partially-ordered and fully-ordered phases; fields applied along the [111] direction reveal a particularly rich phenomenology. Magnetization plateaus [54]; neutron scattering structure factors [55]; and peaks in the field-dependent specific heat [56], magnetostriction, and dielectric constant [57] have all been used to pinpoint high-field DTO ordering transitions. At very low temperatures, fields with strengths ~ 0.25 T completely polarize the spins in the trigonal layers of the magnetic pyrochlore lattice, effectively decoupling the remaining 2D kagome layers. The kagome spins have relatively small components parallel to the [111] field, so between 0.25 T and ~ 1 T they retain a reduced ground state degeneracy while obeying the Bernal-Fowler rules; this is the "kagome ice" state. Fields above ~ 1 T completely polarize the crystal such that all tetrahedra are in a "1-in, 3-out" state. At higher temperatures thermal energy can also break the

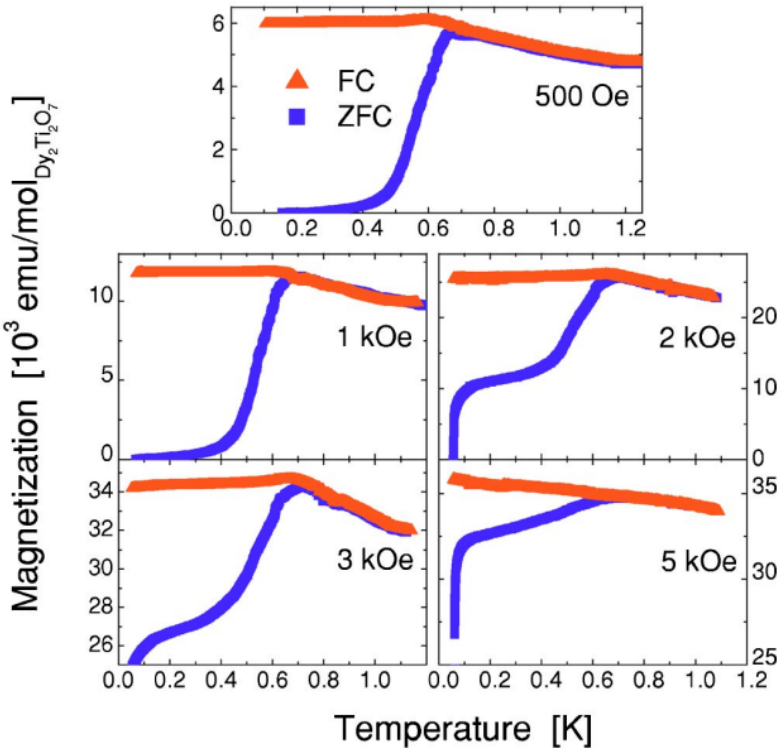

Figure 2.8: Magnetization of polycrystalline DTO samples in several applied fields after zero-field cooling (ZFC) and field cooling (FC). DTO demonstrates history-dependent glassy behavior below ~ 0.6 K, but curiously the effective freezing temperature where ZFC and FC results diverge is very weakly dependent on the magnetic field. Figure from [37].

Bernal-Fowler rules; spin ice correlations (Equation (2.2)) are completely absent in neutron scattering measurements at $T = 20$ K [45].

Similar Zeeman and thermal energy considerations apply for fields in other directions. The specific phase diagram varies with the field direction (for example, a [001] field will fully polarize DTO tetrahedra in a single allowed ice configuration), but in all cases the spin ice degeneracy can be broken by sizeable magnetic fields. In our experiments we always apply small fields ($\mu_0 H \sim 1$ G or less) and remain at low temperatures, allowing us to examine DTO in the spin ice regime.

2.2 Dynamics

No magnetic ordering is observed in DTO even at temperatures as low as 50 mK, which is far smaller than T_{cw}. At temperatures below $\sim$ 15 K DTO magnetism begins to deviate from ideal Curie-Weiss behavior, and the complex AC susceptibility $\chi = \chi' - i\chi''$ presents a rich phenomenology. Over the past 15 years this susceptibility has been accurately measured in both polycrystalline [37][58] and single-crystal rod [59][60][61] samples. In polycrystalline samples a dip in χ' and small peak in the dissipative component χ'' appear as the temperature is cooled to $T \approx 15$ K [58][62], indicating that some kind of magnetic transition may occur at this temperature. No other significant features are apparent in χ until DTO reaches temperatures $\sim$ a few Kelvin or less. Since these temperatures are where neutron scattering reveals spin-ice structure factors [45], we will consider $T < 15$ K to be the spin ice temperature range.

For the rest of this work we will focus on DTO behavior at very low temperatures ($T < 4$ K), where theory has predicted the existence of exotic magnetic excited states (Section 2.3.2). Figure 2.9 shows the typical observed temperature dependence of χ [37]. Two things become apparent upon comparison with the spin glasses (Section 1.3): the maxima in $\chi'(T)$ are much broader and more asymmetric in DTO than would be expected in a spin glass, and χ''/χ' is substantially larger in DTO (where it is $\sim 1/2$) than it is in spin glasses (where it is $\sim 1/10$ or less). Furthermore, the dissipative susceptibility $\chi''(\omega)$, shown in Figure 2.10A and C, is much more sharply peaked than the dissipation in spin glasses. At a given temperature there is a single peak in χ'', indicating that the system has some characteristic central relaxation time, but the DTO peak widths are less than 2 decades; this is a substantial departure from the much broader

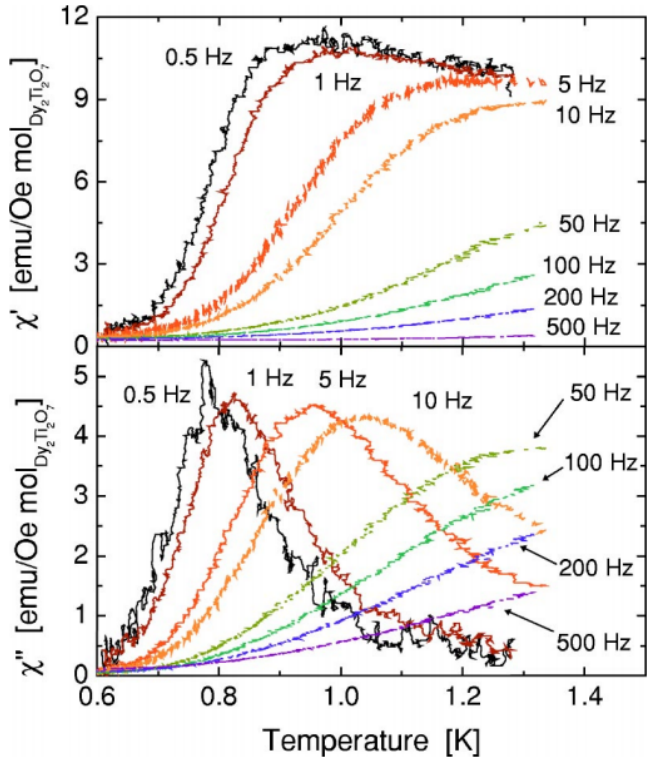

Figure 2.9: Real (top) and imaginary (bottom) components of the complex susceptibility χ in a polycrystalline DTO sample at low temperatures. The maxima in χ' and χ'' have a strong frequency dependence, and the $\chi'(T)$ peaks are fairly broad and asymmetric. These data look very different from what is typically observed in disordered spin glass materials. Figure from [37].

spin glass behavior shown in Figure 1.5. These observations, along with magnetization measurements (Figure 2.8), indicate that DTO may be influenced by physics very different from what has previously been found in glassy magnetic systems.

Figure 2.10 also shows that the χ'' peak positions shift rapidly toward small frequencies as DTO cools below $\sim$ 1 K, indicating that microscopic relaxation times begin to diverge rapidly at low temperatures. These data do not follow the simple Debye form $\chi = \chi_0/(1 + i\omega\tau)$ generally used for systems with a single relaxation time τ; the χ'' peaks are too wide and there is an asymmetric weighting toward higher frequencies. Instead of a single thermally-activated microscopic

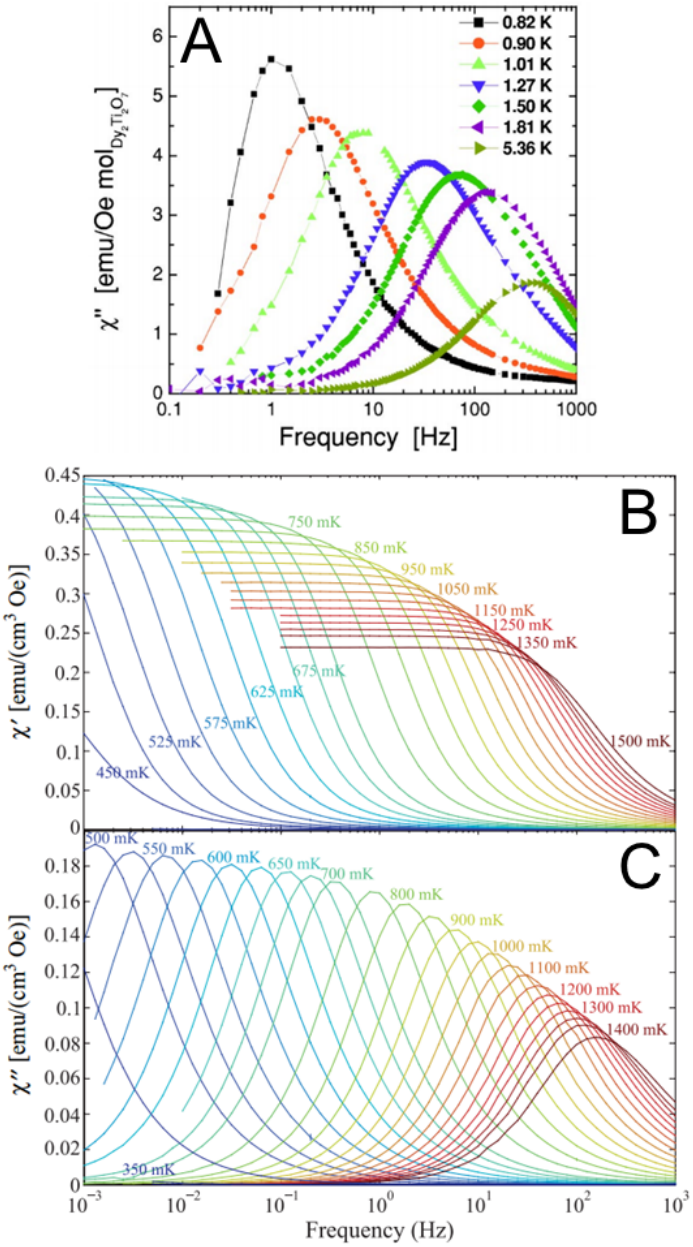

Figure 2.10: (A) Dissipative component χ'' of the AC susceptibility measured in polycrystalline DTO. The figure is from [37]. These results are similar to measurements of **(B)** χ' and **(C)** χ'' in single-crystal rod samples (figures from [61]). In both cases χ'' has a single peak at each temperature, indicating the presence of a characteristic relaxation time, but Debye relaxation cannot quantitatively describe the data. The peak positions shift rapidly to lower frequencies as the temperature approaches 500 mK, indicating the divergence of microscopic relaxation times.

relaxation process, there is a more complex landscape of excitations and dynamics in the system. Despite the multiplicity of past measurements of $\chi(\omega, T)$, no one has found a self-consistent parametrization of an analytic function of χ that characterizes the data over a wide range of frequencies and temperatures.

Time-domain relaxation measurements provide an additional window into the fascinating dynamics occurring in DTO at low temperatures. Several groups have performed accurate magnetization relaxation measurements on single crystal rods; typical results [60] are shown in Figure 2.11. DTO exhibits ultraslow relaxation at low temperatures; at several hundred mK the DTO magnetization can relax over *days*. Other low-temperature relaxation measurements have observed similarly-long magnetization decays [63][64], and this ultraslow behavior offers an empirical explanation for the onset of magnetization history dependence (Figure 2.8) and discrepancies in short- and long-time thermal measurements (Figure 2.7). Figure 2.11 shows that below $\sim$ 500 mK DTO does not fully relax within 1000 s, which is the time window typically examined by the thermal relaxation measurements [42] and static magnetization measurements [37]. Many previous measurements of DTO properties have therefore measured its out-of-equilibrium properties at temperatures below 500-600 mK. The apparent residual Pauling entropy in thermal measurements results from a "freezing-in" of magnetic dynamics on the timescales probed by these experiments; the typical lowest-T data shown in Figure 2.4 is characteristic of a DTO glass state.

Attempts to fit the time-domain relaxation in DTO over a large parameter space have been largely unsuccessful. Even though AC measurements indicate that some characteristic relaxation time describes DTO dynamics, a simple Debye parametrization, $M(t) = M_0 \exp(-t/\tau)$, does not fit any of the measured DC

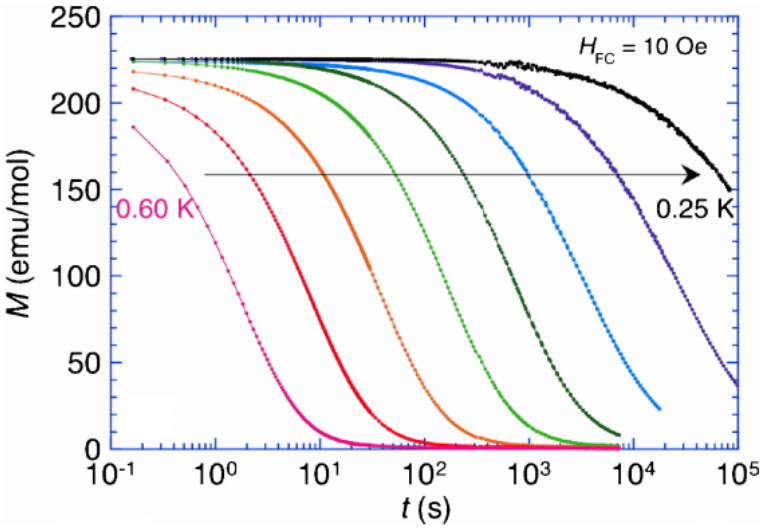

Figure 2.11: Magnetization relaxation of a single-crystal rod of DTO after turning off an applied field. Temperatures are equally spaced from 0.25 K to 0.6 K. As the temperature cools below 0.6 K, characteristic relaxation times increase rapidly; temperature changes of 100 mK can increase the relaxation time by more than an order of magnitude. Figure from [60].

data [60][63][64]. Thermal relaxation measurements have also observed substantial departures from simple exponential behavior [42][44]. Functions with multiple exponentials or multiple discrete relaxation times have been unable to fit DC observations over a significant range of temperatures and times, indicating that these are ill-fated approaches to the problem. We will return to this puzzle later in the context of our own experiment.

2.3 Theory of $Dy_2Ti_2O_7$ magnetism

2.3.1 The Dipolar Spin Ice Model

The model that has become widely used in theoretical attempts to understand DTO is the Dipolar Spin Ice Model (DSIM), in which the Hamiltonian takes the

form [65]

$$H_{DSI} = -J \sum_{\langle ij \rangle} \mathbf{S}_i \cdot \mathbf{S}_j + Da^3 \sum_{j>i} \left[\frac{\mathbf{S}_i \cdot \mathbf{S}_j}{|\mathbf{r}_{ij}|^3} - \frac{3(\mathbf{S}_i \cdot \mathbf{r}_{ij})(\mathbf{S}_j \cdot \mathbf{r}_{ij})}{|\mathbf{r}_{ij}|^5} \right] \tag{2.3}$$

where J is the nearest-neighbor exchange energy, a is the pyrochlore lattice constant, and $D = \mu_0 \mu^2/(4\pi a^3) \approx 1.4$ K is the energy scale of nearest-neighbor dipole interactions. This model incorporates both nearest-neighbor exchange interactions and long-range dipole interactions, which should be significant because of the large size of the Dy^{3+} magnetic moment. D is typically treated as a fixed constant since it depends on the size of μ_{Dy} and the lattice constant, which are both well-known quantities. DSIM simulations perfomed using single-spin-flip simulation steps were able to fit the observed peaks in the heat capacity with $J = -3.72$ K [65]; DTO behavior therefore seems to derive from competition between antiferromagnetic exchanges and dipole interactions that are effectively ferromagnetic when subjected to anisotropic pyrochlore constraints.

When simulations also consider closed loops of spins that can coherently flip and satisfy the Bernal-Fowler rules, the DSIM predicts the existence of a sharp heat capacity peak at ~ 200 mK. This feature signifies a breaking of the spin ice degeneracy and a transition to a single state with long-range magnetic order [52], as described in Section 2.1. The inclusion of loops in the simulation is necessary to achieve this result because at low temperatures single spin flips, which break the ice rules and carry a significant energy penalty $\Delta E \approx 5$ K, rapidly become statistically unlikely; this makes ergodicity increasingly difficult to achieve within the computing time feasible for simulations.

Correlated loop algorithms have also provided new perspectives about neutron scattering data. Simulations of the DSIM given by Equation (2.3) capture many features of neutron scattering results (Figure 2.12A) at low temperatures

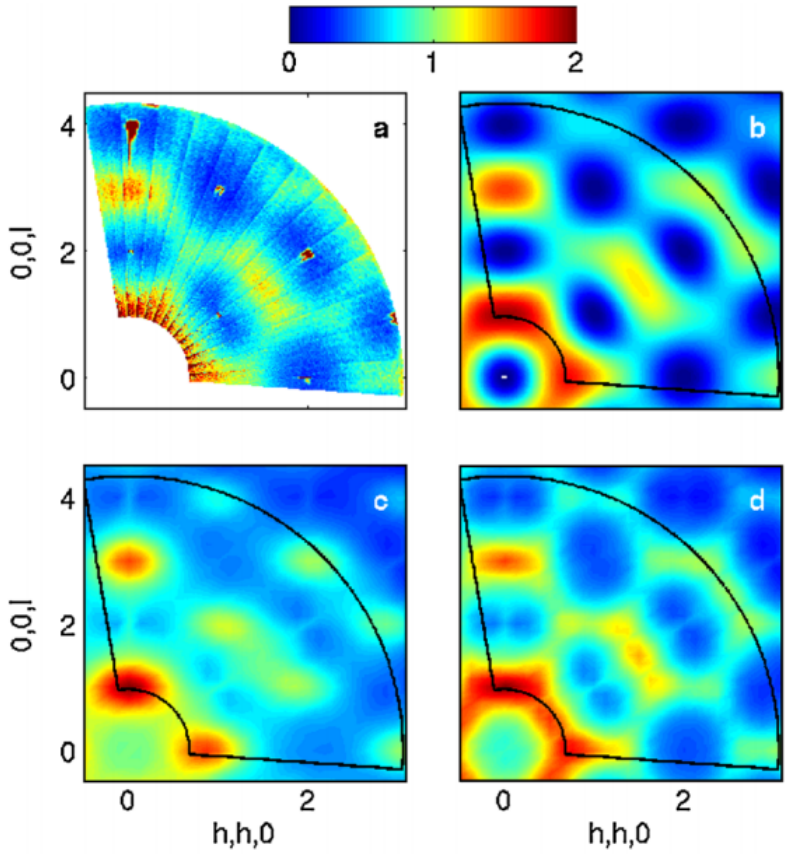

Figure 2.12: **(A)** Neutron scattering intensity in single-crystal DTO at 300 mK; measurements were performed in [45]. **(B)** Scattering intensity predicted by simulations of zero-magnetization hexagonal loops of spins. This rather crude model captures more of the empirical observations than the standard DSIM predictions, which are shown in **(C)**. **(D)** Scattering intensity predicted by a generalized DSIM that includes second-nearest and third-nearest neighbor exchange interactions. Figure from [35].

[35], but there is substantial room for improvement (Figure 2.12C). In fact, an improved description of the scattering data can be achieved by simulating a crude phenomenological model that divides the DTO spins into zero-magnetization hexagonal loops that can undergo circulation, with no correlations between separate loops (Figure 2.12B). Microscopically, it was found that two additional exchange interactions (second-nearest-neighbor exchange J_2 and third-nearest-neighbor exchange J_3) were necessary for a "generalized" DSIM to accurately

describe the observed DTO magnetic structure (Figure 2.12D). The best fits were achieved with an antiferromagnetic $J_1 = -3.41$ K (close to the simple DSIM result), a ferromagnetic $J_2 = 0.14$ K, and an antiferromagnetic $J_3 = -0.025$ K [35]. It therefore seems that the standard DSIM of Equation (2.3) may be incomplete, and the success of the phenomenological spin cluster model may point to a different method with which we can understand DTO.

2.3.2 Monopoles

DTO has attracted substantial recent attention as a potential host of a dilute gas of deconfined Coulombic magnetic quasiparticles; these are known evocatively as "monopoles". A "dumbbell model" gives a particularly clear way to derive the existence of such a state from the DSIM [66]. In this model each Dy^{3+} moment is recast as a pair of positive and negative fractionalized charges $q_m = \pm\mu/a_d$ separated by the tetrahedra center distance a_d (Figure 2.13A and B). Since each tetrahedron has four spins, in this new view there are four fractionalized charges at each tetrahedron center site. Charges separated by a non-zero distance interact via a magnetic Coulomb interaction, and there are exchange-like interactions between charges at the same location:

$$V(r_{ij}) = \begin{cases} \frac{\mu_0}{4\pi}\frac{q_i q_j}{r_{ij}}, & r_{ij} \neq 0 \\ \nu_0 q_i q_j, & r_{ij} = 0 \end{cases} \tag{2.4}$$

$$\nu_0 = \left(\frac{a_d}{\mu}\right)^2 \left[\frac{J}{3} + \frac{4}{3}\left(1 + \sqrt{\frac{2}{3}}\right)D\right]$$

This definition of ν_0 exactly reproduces the interaction between nearest-neighbor spins, and the fractionalized Coulombic charges reproduce the long-

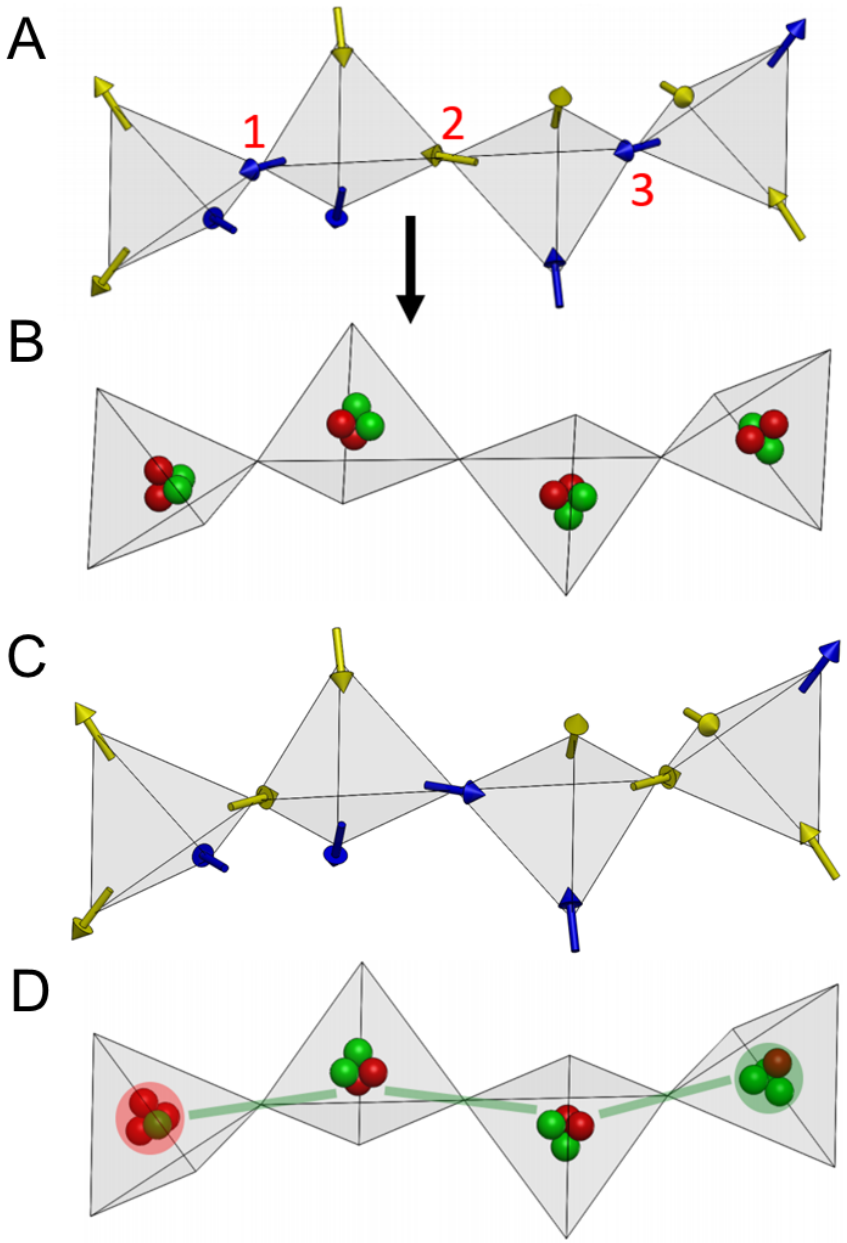

Figure 2.13: (A) A configuration of moments (arrows) that satisfies the Bernal-Fowler ice rules for the DTO ground states. **(B)** In the dumbbell model each Dy^{3+} moment is recast as a positive (green) and negative (red) charge separated by the diamond lattice constant a_d. Each pyrochlore tetrahedron now hosts four fractionalized charges at its center. **(C)** Flipping moments 1, 2, and 3 in (A) creates a separated pair of tetrahedra that violate the ice rules. **(D)** In a monopole picture, flipping moment 1 in (A) creates negative (red) and positive (green) monopoles in neighboring tetrahedra. Subsequently flipping moments 2 and 3 separates the monopoles.

distance dipolar interactions of the DSIM. Any discrepancy between the dumbbell model and the DSIM falls off at least as quickly as $1/r^5$. We can rewrite Equation (2.4) in an even more evocative form by considering the sums of charges in each tetrahedron, $Q_i \equiv Q(\mathbf{r}_i) = \sum_j q_j \delta(\mathbf{r}_j - \mathbf{r}_i)$. With this variable definition we can rewrite the total energy $\sum V(\mathbf{r}_{ij})$ as

$$V_{monopole} = \frac{\mu_0}{4\pi} \sum_{j>i} \frac{Q_i Q_j}{|\mathbf{r}_{ij}|} + \frac{\nu_0}{2} \sum_i Q_i^2 \tag{2.5}$$

This expression differs from the initial dumbbell potential, $\sum V(\mathbf{r}_{ij})$, by a constant term $\frac{1}{2}\sum q_i^2$. Constant terms in the energy do not affect the resulting dynamics, so the two expressions yield identical physics and we have now successfully recast the DSIM into a description based on Coulombic monopoles with charge Q_i. The first term in Equation (2.5) is a magnetic Coulomb interaction, and the second term takes into account the self-energy of monopole creation. We emphasize that this description is essentially identical to the DSIM, with any discrepancies falling off very quickly with the distance between monopoles.

If the monopole self-energy becomes very large ($\nu_0 \to \infty$), the total system energy will be minimized if all $Q_i = 0$; this means that each tetrahedron contains two positive and two negative charges, and the system satisfies the Bernal-Fowler ice rules. We expect that this limit will be applicable in the $T \to 0$ limit, when thermal excitations become more and more costly. When ν_0 is finite we have to consider possible excitations out of the "monopole vacuum". Because there are four individual charges $q = \pm\mu/a_d$ in each tetrahedron, monopoles can have charge $Q = 0, \pm 2\mu/a_d, \pm 4\mu/a_d$ corresponding to zero-spin, single-spin, and double-spin violations of the ice rules. From Equation (2.5) the energy needed to flip one spin and create a pair of monopoles with the lowest non-zero charge

is

$$\Delta_{pair} = 2\left(\frac{\nu_0}{2}\right)Q^2 - \frac{\mu_0 Q^2}{4\pi a_d} \tag{2.6}$$
$$= 5.64 \text{ K}$$

Since $\Delta_{pair} \sim Q^2$, creation of double-spin-flip violations requires, to leading order (tetrahedra share only a single spin, so creation of a doubly-excited monopole pair requires the additional creation of two other singly-excited monopoles) an energy $\Delta_2 \approx 4\Delta_{pair}$. Such excitations will be suppressed by a factor $\sim \exp(-3\Delta/k_BT)$ compared to single-spin-flip excitations; at 2 K, the high end of the putative monopole model range (see below), there will be ~ 2 charges $Q_2 = 4\mu/a_d$ for every 10000 single charges $Q = 2\mu/a_d$. For simplicity we will take all monopole charges to be $Q_m = \pm 2\mu/a_d$, since this is an excellent approximation of the full monopole ensemble.

As shown in Figure 2.13C and D, after their creation a pair of monopoles can separate via additional spin flips with neighboring neutral tetrahedra. This movement requires no additional violations of the ice manifold; the only energy cost is the work done against the Coulomb attraction, so monopoles are mobile. At suitably low temperatures, Δ_{pair}/k_BT will be large enough that monopoles will occupy a relatively small fraction of tetrahedra; there will be a dilute neutral plasma of mobile monopoles.

The energetics of such a system have been analyzed by modifying the Debye-Hückel theory of electrolytes [67] for use in a monopole "magnetolyte" [68]. More specifically, the Debye Hückel theory applied to a neutral plasma ($N_+ = N_- = N/2$) of hard-sphere ions with charge $\pm q$ is directly applicable to the monopole picture of DTO. There are two contributions to the total monopole free energy: a contribution from the entropy and self-energy of monopoles

themselves, and an electrostatic contribution from inter-monopole Coulomb interactions. From the second term in Equation (2.5), the self-energy of a single monopole is $\Delta_{single} = \nu_0 Q^2/2$. The energy density of N monopoles on N_t tetrahedra is then simply $U = \rho N_t \Delta_{single}$, where $\rho \equiv N/N_t$ is the fraction of tetrahedra occupied by monopoles. The number of possible distinct configurations of $N/2$ positive and $N/2$ negative monopoles on N_t tetrahedra is $W = N_t!/[(N/2)!(N/2)!(N_t - N)!]$. The entropy $S = k_B \ln W$ can be easily calculated using Stirling's approximation $x! \approx x \ln x - x$; using this approximation and the expression for the free energy $F = U - TS$, we find that the free energy per spin ($N_s = 2N_t$) due to the creation of monopoles themselves is given by

$$\frac{F_{self}}{N_s} = \frac{\rho}{2}\Delta_{single} + \frac{k_B T \rho}{2} \ln\left(\frac{\rho/2}{1-\rho}\right) + \frac{k_B T}{2} \ln(1-\rho) \tag{2.7}$$

Now we need to find the energy contribution from monopole interactions. In an electrolyte, an ion of a given charge will attract a cloud of oppositely-charged ions that screens the electrostatic potential. For hard-sphere ions the potential satisfies the conditions

$$\nabla^2 \phi(r) = \begin{cases} 0, & r \le a \\ -\frac{4\pi}{\epsilon}\rho_q(r), & r > a \end{cases}$$

Now consider a positive ion fixed at $r = 0$. The charge density $\rho_q(r)$ outside this ion has the form $\rho_q(r) = q(\rho_{++}(r) - \rho_{--}(r))$, where ρ_{+i} are charge densities in the field of a + ion. We can approximate the ρ_{+i} with a Maxwell-Boltzmann distribution $\rho_{+i}(r) = \rho_0 \exp(-q_i \phi(r)/k_B T)$, where $\phi(r)$ is the electrostatic potential a distance r from the fixed ion. In the limit of low electrostatic energy, $q\phi << k_B T$,

this yields a simple expression for the potential in the region $r > a$:

$$\nabla^2\phi(r) = \kappa^2\phi(r),$$
$$\kappa = \sqrt{\frac{4\pi q^2\rho_e}{\epsilon k_B T}}$$

where $\rho_e = N/V$ is the total combined density of the ions and κ is an inverse "Debye length". κ^{-1} gives the characteristic distance over which the central ion potential becomes screened.

To find an expression for $\phi(r)$ over all space, we must solve the Laplace equations $\nabla^2\phi = 0$, $r \leq a$ and $\nabla^2\phi = \kappa^2\phi$, $r > a$, subject to the constraints that ϕ and $\mathbf{E} = -d\phi/dr$ must be continuous at $r = a$. Doing so gives the following form for the potential at distances $r \leq a$:

$$\phi(r) = \frac{q}{\epsilon r} - \frac{q\kappa}{\epsilon(1+\kappa a)} \tag{2.8}$$
$$= \phi_{ion} + \phi_{cloud}$$

The potential experienced by the central ion due to the surrounding cloud is given by the second term in the above expression. The total electrostatic energy of the entire plasma can now be calculated by charging all ions simultaneously from 0 to q:

$$F_{el} = N\int_0^q dq'\phi_{cloud}(q') \tag{2.9}$$

Evaluation of the integral yields the full Debye-Hückel free energy for a neutral electric plasma:

$$f_{el} = -\frac{k_B T V}{4\pi a^3}\left[\ln(\kappa a + 1) - \kappa a + \frac{1}{2}(\kappa a)^2\right] \tag{2.10}$$

The total free energy of the monopole ensemble can now be found by translating the Debye-Hückel result to a magnetic system ($a \to a_d$, $q \to Q_m$,

$\rho_e \rightarrow \rho_m = N/V$, $1/\epsilon \rightarrow \mu_0/4\pi$) and adding it to the free energy of monopole creation (Equation (2.7)). When written as a function of the tetrahedra occupation fraction $\rho = N/N_t$, the total free energy per spin takes the following form [68]:

$$\begin{aligned}\frac{F}{N_s} = & \frac{\rho}{2}\Delta_{single} + \frac{k_B T \rho}{2}\ln\left(\frac{\rho/2}{1-\rho}\right) + \frac{k_B T}{2}\ln(1-\rho) \\ & - \frac{k_B T}{3\sqrt{3}\pi}\left[\frac{\alpha^2(T)\rho}{2} - \alpha(T)\sqrt{\rho} + \ln[1+\alpha(T)\sqrt{\rho}]\right], \\ \alpha(T) = & \sqrt{\frac{3\sqrt{3}\mu_0 Q_m^2}{8 a_d k_B T}}\end{aligned} \tag{2.11}$$

The monopole density $\rho(T)$ can be found by minimizing Equation (2.11) with respect to ρ; this yields an expression that cannot be solved analytically, but can instead be numerically evaluated with an iterative approach. The calculated $\rho(T)$ implies that this dilute monopole plasma model is applicable over a finite range of temperatures. At $T \sim 2$ K the expected monopole separation becomes comparable to the minimum separation distance a_d, while at temperatures less than a few hundred mK relaxation timescales become so large that predicting DTO behavior becomes very challenging (Section 2.3.1). The evocative monopole plasma picture is therefore expected to be most applicable in a temperature range ~ 0.5 K $< T < \sim 2$ K [68].

The minimized free energy $F(\rho(T))$ can be used to calculate various thermodynamic quantities; the specific heat is of particular interest since it has been measured in DTO by numerous experiments (Section 2.1). The only free parameter in Equation (2.11) is the self-energy Δ_{single}, which is a function of the exchange energy scale J. As in earlier DSIM simulations [52][65], $\Delta_{single}(J)$ can be adjusted until the best fit to the data is achieved. Figure 2.14 shows that Debye-Hückel calculations with $\Delta_{single} = 4.35$ K capture a large amount of the heat capacity behavior at very low temperatures. This self-energy value is very

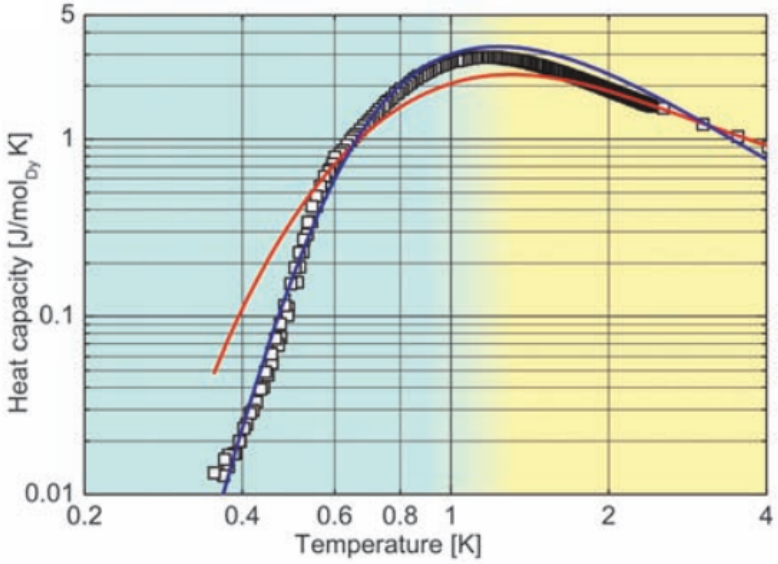

Figure 2.14: The low-temperature heat capacity of a single-crystal sample of DTO (squares) along with theoretical fits to the data. Fits to a Debye-Hückel magnetolyte model (blue line) capture a large amount of the $T < 2$ K heat capacity variation, unlike a nearest-neighbor model that takes only single-tetrahedron interactions into account (red line). Figure from [41].

close to the DSIM simulation expectation of $\Delta_{single} \approx 4.23$ K, indicating that this monopole model seems to be a very good approximation of the full DSIM. Simulations of DTO that use a monopole gas model also predict the DTO relaxation time more effectively than a standard Arrhenius model with an energy barrier given by $\Delta_{pair}/2$, which is the effective creation energy of a single monopole [69] (Figure 2.15). The monopole model thus seems to be an improvement over simpler models of DTO, and its predicted delocalized Coulombic magnetic excitations constitute a state of matter that has never before been observed in other materials.

However, we must note that although monopole fits offer improved descriptions compared to more naïve models, these fits are not perfect. For example, there are significant deviations between the measured heat capacity and monopole fits above 1 K (note the log scale in Figure 2.14). Fits to dynamical

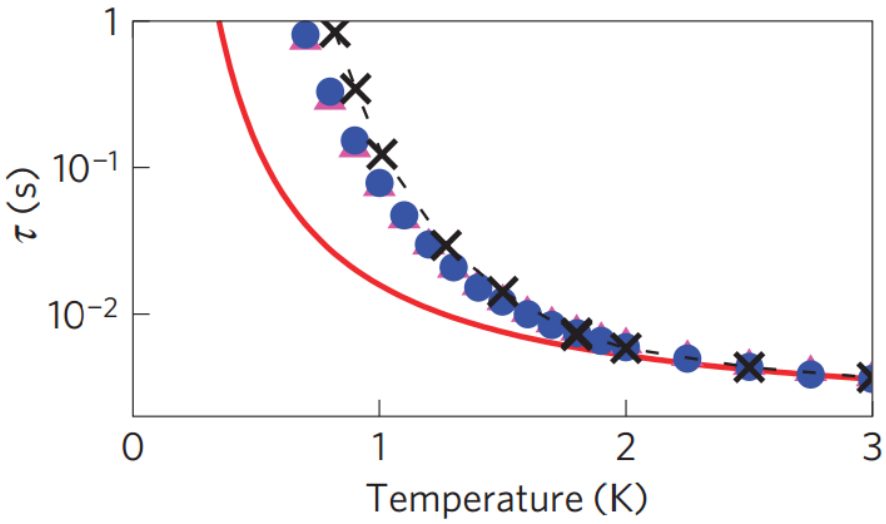

Figure 2.15: The rapid increase of DTO relaxation times at low temperatures (crosses, from data in [37]) is described more effectively by simulations of a monopole gas (pink triangles for fixed chemical potential, blue circles for a chemical potential that varies with concentration) than by a simple thermally-activated Arrhenius model (red line). However, these simulations still significantly underestimate the divergence of $\tau(T)$ below 1 K. Figure from [69].

quantities are even more problematic; monopole simulations still significantly underestimate the rate at which DTO relaxation times diverge with decreasing temperature (Figure 2.15), and DSIM simulations have so far been unable to describe measurements of the complex AC susceptibility [70].

Efforts to predict monopole dynamics thus may benefit from a different approach. Such an approach was provided by Ryzhkin, who thought about a non-interacting monopole system in terms of its transport properties [71]. This work adapted Jaccard's analysis of the thermodynamics of defects in water ice [72], and it relies on two main assumptions: monopole currents can be related directly to changes in the magnetization, and the thermodynamics of monopole transport can be calculated from the principles of entropy production in irreversible processes. We first define a "configuration vector" density $\mathbf{\Omega} = \mathbf{M}/Q_m$ that characterizes the net dipole moment due to monopole positions. A single

spin flip along a direction $\hat{\mathbf{x}}$ changes $\mathbf{\Omega}$ by $\hat{\mathbf{x}}/V$; this is equivalent to a positive monopole being displaced by $a_d\hat{\mathbf{x}}$ or a negative monopole being displaced by $-a_d\hat{\mathbf{x}}$. If we expand our observation volume enough that $a_d\hat{\mathbf{x}} \to d\mathbf{x}$ and see N_+ positive and N_- negative monopoles pass through V in a time dt, the coarse-grained configuration vector change can be written $d\mathbf{\Omega} = \frac{1}{V}(N_+ d\mathbf{x} - N_- d\mathbf{x})$. Using the monopole number current densities $\mathbf{j}_i = n_i d\mathbf{x}/dt$, this leads to the first fundamental monopole transport relation:

$$\frac{d\mathbf{\Omega}}{dt} = \mathbf{j}_+ - \mathbf{j}_- = 2\mathbf{j}_+ \tag{2.12}$$

where we assume that our *macroscopically small* observation volume is large enough that $\mathbf{\Omega}$ and $\mathbf{j}$ vary smoothly with time.

To further develop this monopole transport theory, Ryzhkin used the thermodynamics of irreversible processes in a manner analogous to Jaccard's analysis of the electrical properties of water ice. Monopoles flow in response to an applied magnetic field; the entropy change due to this transport is given by [71]

$$T\frac{dS}{dt} = \mathbf{j} \cdot Q_m\mathbf{B} + T\frac{dS_c(\mathbf{\Omega})}{dt} \tag{2.13}$$

where $S_c(\mathbf{\Omega})$ is the configurational entropy density corresponding to a given configuration vector. As discussed in Section 2.1, larger values of $|\mathbf{M}| = Q_m|\mathbf{\Omega}|$ are possible in fewer spin configurations, and therefore increasing $\mathbf{\Omega}$ carries an entropy cost. In the context of the Bernal-Fowler rules on a pyrochlore lattice, this entropy cost was calculated to be [73]

$$S_c(\mathbf{\Omega}) - S_c(0) = -\frac{4}{\sqrt{3}}a_d k_B |\mathbf{\Omega}|^2$$

Taking the time derivative of this result and inserting it into Equation (2.13) allows us to write the entropy change in a more evocative way:

$$T\frac{dS}{dt} = \mathbf{j} \cdot \left(Q_m\mathbf{B} - \frac{8}{\sqrt{3}}a_d k_B T\mathbf{\Omega} \right) \tag{2.14}$$

where $\mathbf{j} = 2\mathbf{j}_+$. This has the form of the work rate of a generalized thermodynamic force, $P = \mathbf{j} \cdot \mathbf{F}$. Now we assume that the charged monopole current $\mathbf{J}_m = Q_m \mathbf{j} = d\mathbf{M}/dt$ has a linear response to the applied force characterized by a mobility u; the average monopole velocity is $\mathbf{v} = u\mathbf{F}/Q_m$. The current can then be written in the following form:

$$\mathbf{J}_m = \frac{d\mathbf{M}}{dt} = Q_m n_m u \frac{\mathbf{F}}{Q_m} = Q_m n_m u \left(\mathbf{B} - \mu_0 \chi_m^{-1} \mathbf{M} \right), \tag{2.15}$$
$$\chi_m = \frac{\sqrt{3}\mu_0 Q_m^2}{8 a_d k_B T} \approx \frac{8.3 \text{ K}}{T}$$

Now we predict the magnetic dynamics of a monopole gas in an AC field, since Equation (2.15) can be easily solved in Fourier space. Ryzhkin took $\mathbf{B} = \mu_0 \mathbf{H}$, and substituting $\mathbf{M}(\omega) = \chi(\omega)\mathbf{H}(\omega)$ yields a simple form for χ:

$$\chi_B(\omega) = \frac{\chi_m}{1 + i\omega\tau} \tag{2.16}$$
$$\tau = \frac{\chi_m}{\mu_0 Q_m n_m u}$$

Some subsequent experimental investigations into DTO [59][74] attempted to use this result to fit their data. However, the derivation of Equation (2.16) assumes that interactions between moments are negligible; we would need to use the full macroscopic field expression $\mathbf{B} = \mu_0(1 + \chi)\mathbf{H}$ to account for interactions between moments. Debye-Hückel fits to the heat capacity (Figure 2.14) show that in a monopole model we need to account for interactions to reasonably describe experimental data; interactions are therefore very significant in this problem and we cannot expect Equation (2.16) to be correct. The better way to solve Equation (2.15) involves the substitution of the complete macroscopic field relation $\mathbf{B} = \mu_0(1 + \chi)\mathbf{H}$; this yields the expression

$$i\omega\chi(\omega) = \mu_0 n_m Q_m u \left(1 + (1 - \chi_m^{-1})\chi(\omega) \right)$$

Solving for the susceptibility, we find the self-consistent solution for χ in an interacting system:

$$\chi(\omega) = \frac{(1-\chi_m^{-1})^{-1}}{1-i\omega\tau}, \qquad \tau = \frac{1}{\mu_0 Q_m n_m u(1-\chi_m^{-1})} \tag{2.17}$$

The differences in these results for the monopole susceptibility are not merely of pedagogical importance; in Chapter 4 we will show that they lead to vastly different predictions about the fields created by monopole currents.

We can further account for monopole interactions by using the density $n_m(T)$ that minimizes the full Debye-Hückel free energy (Equation (2.11)). From Equation (2.17) we see that the relaxation time is inversely proportional to n_m, so we expect screening in a monopole magnetolyte to alter $\tau(T)$. This is indeed the case, and Debye-Hückel calculations yield results similar to the simulation findings shown in Figure 2.15 [68]. However, this also means that even the full Debye-Hückel theory underestimates the rise of $\tau(T)$ in DTO below 1 K, indicating that it may be an incomplete description of DTO dynamics.

CHAPTER 3

THE EXPERIMENT

3.1 The Dilution Refrigerator

The ^{3}He-^{4}He dilution refrigerator is a workhorse of low-temperature physics; it offers high continuous cooling power down to temperatures ~ 10 mK. Though they are isotopes of the same element, ^{3}He and ^{4}He have markedly different properties at low temperatures. ^{3}He has spin $S = 1/2$ and is therefore a fermion, while ^{4}He has $S = 0$ and is a boson. This, along with a difference in zero-point motion due to the different isotope masses, gives rise to a phase diagram [75][76] that can be exploited to achieve very low temperatures. Figure 3.1 shows the low-temperature phase behavior of mixtures of ^{3}He and ^{4}He at saturated vapor pressure. Under its own vapor pressure pure ^{4}He becomes a superfluid at $T_c = 2.17$ K, but increasing the concentration c_3 of ^{3}He lowers T_c. ^{4}He cannot enter the superfluid phase when $c_3 \geq 67.5\%$; at these concentrations the mixture either remains normal or, if the temperature is low enough, separates into a ^{4}He-rich layer and a ^{3}He-rich layer.

However, a finite amount of ^{3}He remains in the ^{4}He-rich layer even in the $T \rightarrow 0$ limit. ^{3}He, due to its smaller mass, has greater zero-point motion than ^{4}He and therefore occupies a greater volume in the liquid phase. Since both isotopes interact via the same van der Waals forces [75], ^{3}He has a greater binding energy when it is mixed into ^{4}He than it can achieve in its pure liquid phase, where the atoms are further apart. ^{3}He also obeys Fermi statistics, so additional ^{3}He atoms must fill higher-energy states; increasing the concentration c_3 therefore also carries an energy cost. At very low temperatures, the chemical poten-

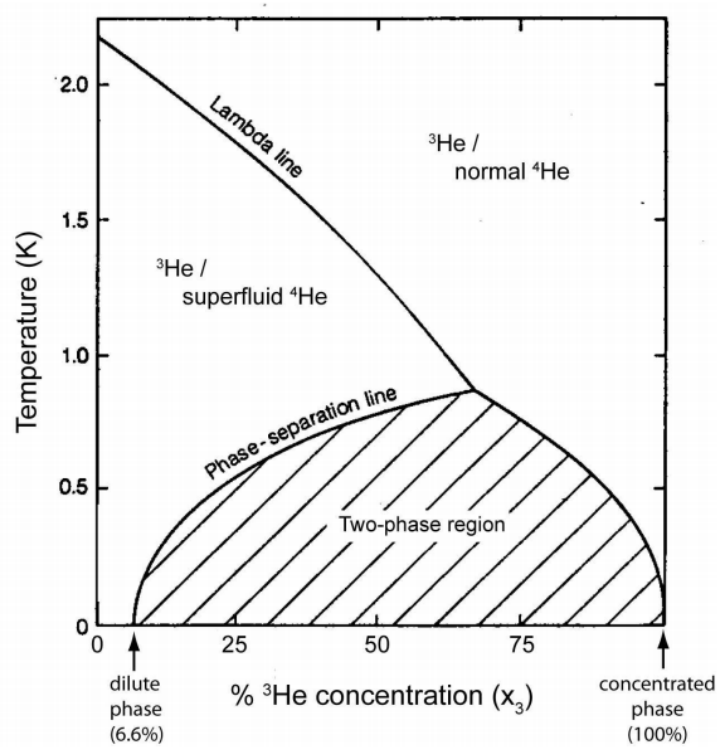

Figure 3.1: Phase diagram of the ^{3}He-^{4}He mixture under its own vapor pressure at low temperatures. The ^{4}He superfluid transition temperature T_c (the "lambda line") is depressed at higher ^{3}He concentrations, and a superfluid cannot exist at all when the mixture is more than 67.5% ^{3}He. A mixture with these ^{3}He concentration levels separates into a ^{4}He-rich phase and a ^{3}He-rich phase at low temperatures. A non-zero amount of ^{3}He remains in the ^{4}He-rich liquid even in the $T \rightarrow 0$ limit, allowing for continuous refrigeration down to very low temperatures. Figure from [76].

tial of pure ^{3}He becomes equal to the combined binding energy gain and Fermi energy cost of adding more ^{3}He to a mixture when $c_3 = 6.6\%$. The enthalpy of ^{3}He is higher in this ^{3}He-dilute layer than in the ^{3}He-rich layer [75], so even at very low temperatures we can cool objects by using their thermal energy to drive ^{3}He from the top ^{3}He-rich liquid layer to the bottom ^{3}He-dilute layer.

Figure 3.2 gives a general schematic for a dilution refrigerator that achieves continuous cooling via the enthalpy difference of He mixture layers [77]; the actual Davis group dilution refrigerator is shown in Figure 3.3. The entire cryostat

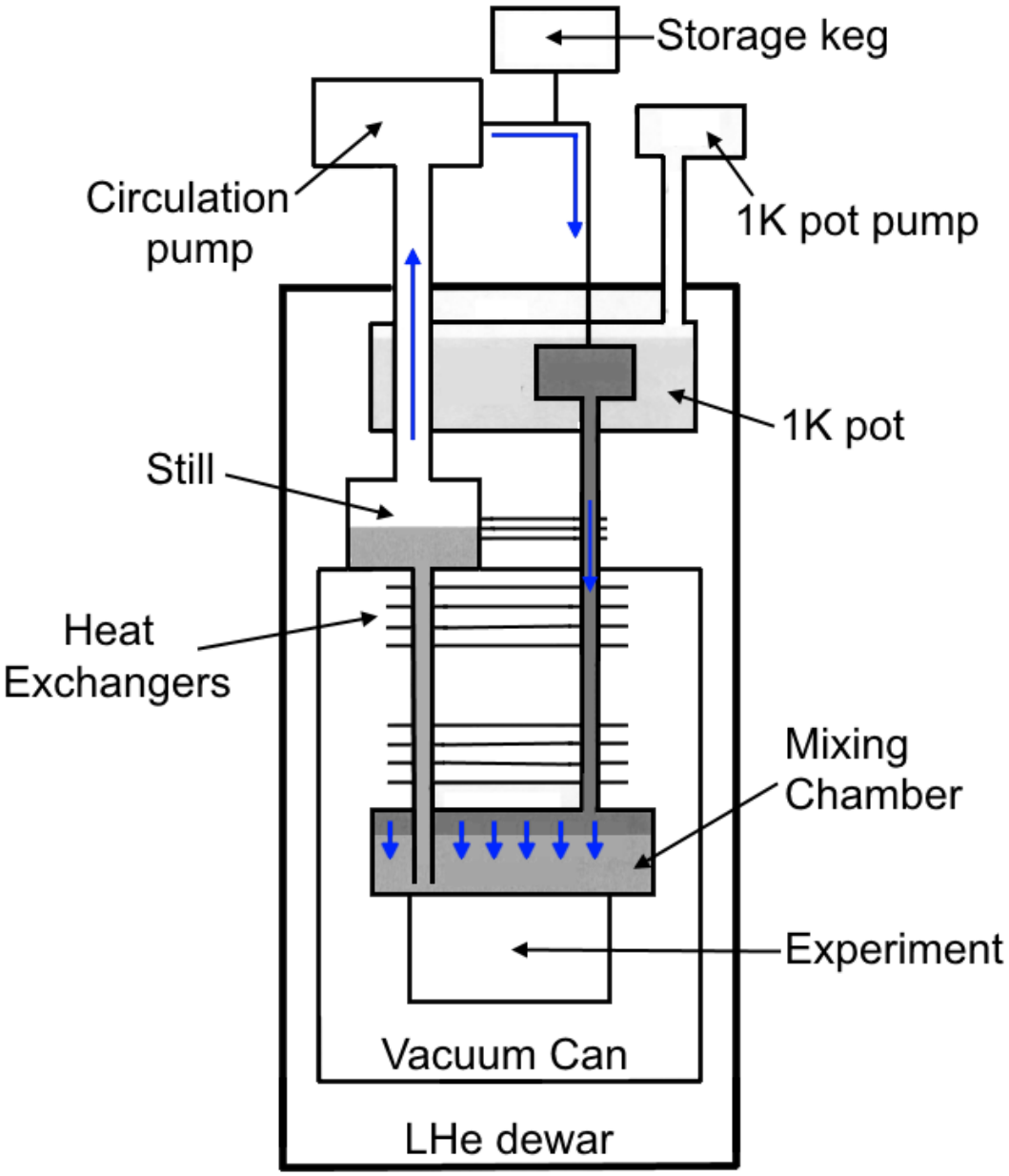

Figure 3.2: General schematic for a dilution refrigerator. ^{3}He is continuously pumped from the heavier ^{3}He-dilute layer and circulated to allow for continuous movement of the isotope between the ^{3}He-rich (dark gray) and ^{3}He-dilute (light gray) layers of the ^{3}He-^{4}He mixture in the mixing chamber. Figure adapted from [77].

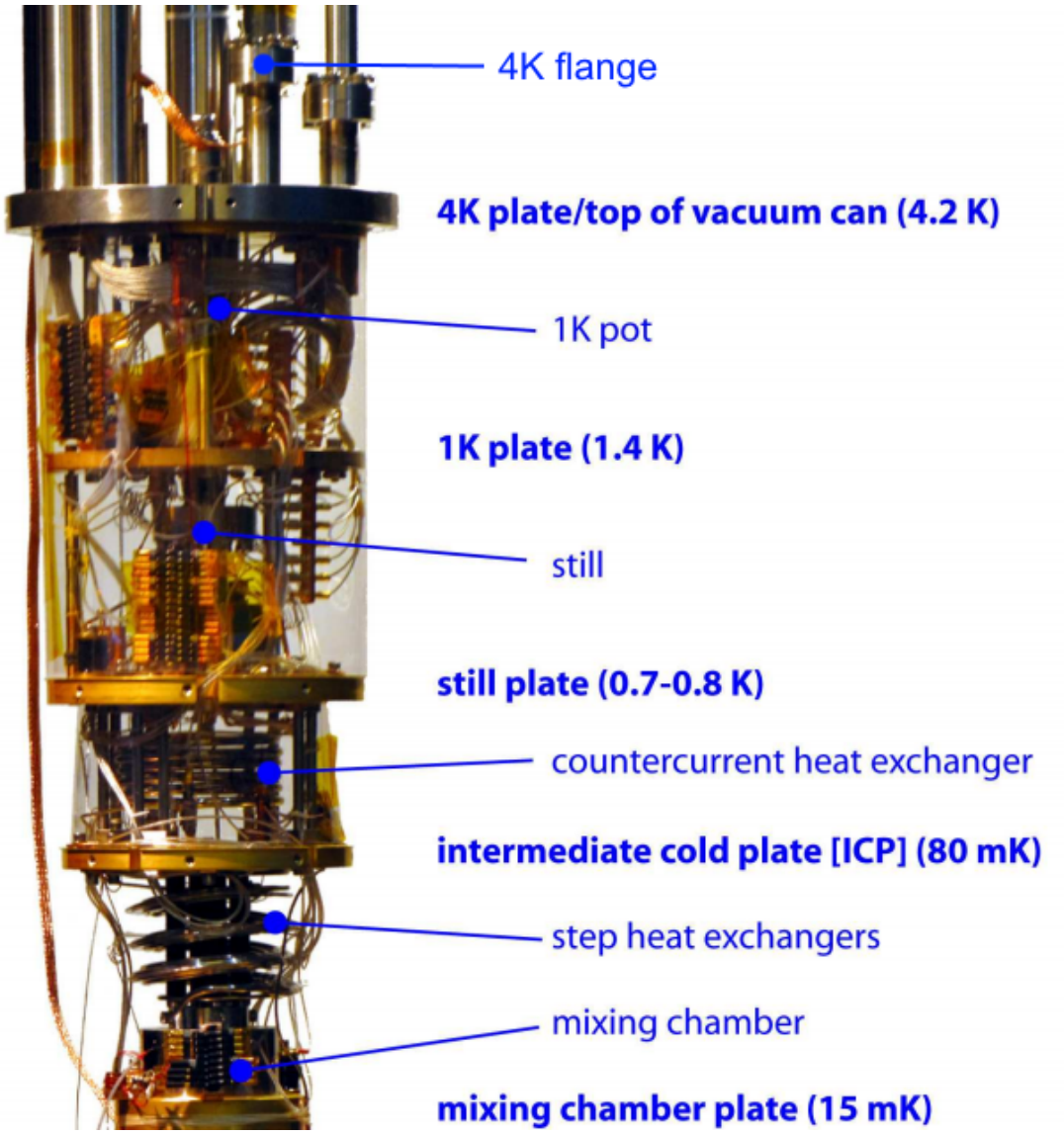

Figure 3.3: The Davis group dilution refrigerator. The cryostat sections from room temperature to the 1K pot were designed and built at Cornell, while the refrigerator sections below the pot were built by Janis Research. Picture adapted from the dissertation of Ben Hunt.

is immersed in a bath of liquid ^{4}He at 4.2 K, and a stainless-steel vacuum can encloses the dilution refrigerator sections that operate below 4 K. The experiment is thermally linked to a mixing chamber (MXC) that contains the He mixture. The terminology of dilution refrigerators has been partly adapted from that of distillation, and in this spirit the mixture is often called "mash". To achieve continuous movement of ^{3}He across the mixture layers we must remove the isotope from the bottom dilute layer; this is done by pumping on a "still" that in our case operates at ≈ 0.7 K. At this temperature the vapor pressure of ^{4}He is negligible compared to that of ^{3}He, so during standard operation the circulating gas is comprised almost entirely of ^{3}He.

Gas returning to the refrigerator is cooled in several stages. First, it cools to 4.2 K as it passes through a tube immersed in the external ^{4}He bath. It then cools to ~ 1 K as it passes by a "1K pot", a container that siphons ^{4}He from the external bath and cools to ~ 1 K as a pump continually removes the resulting vapor. The now-liquid ^{3}He is then cooled further by heat exchangers that link it thermally to the still and to the "outgoing" liquid from the mixing chamber. Eventually the incoming liquid reaches the lighter ^{3}He-rich layer of the mash, transitions to the heavier dilute layer by taking thermal energy from the experiment, and begins its circulation route again. With continuous circulation our fridge achieves cooling powers of $\approx 5\ \mu$W at 30 mK with no active heating of the still; we can increase the cooling power if necessary by heating the still and increasing the ^{3}He circulation rate. There are resistive thermometers on each plate (Figure 3.3), and temperatures are monitored with a Lakeshore 370 Resistance Bridge. We manipulate temperatures and liquid evaporation rates with resistive heaters located on each plate, and experimental temperatures are controlled by connecting the Lakeshore bridge to the MXC heater and using a PID feedback

loop.

During normal operation, gas is pumped from the still by a rotary pump (Pfeiffer DUO 35 M) whose outlet is connected to a gas handling system shown schematically in Figure 3.4. As it moves from the pump to the dilution refrigerator (blue path in Figure 3.4), circulating helium passes through an activated charcoal trap immersed in liquid nitrogen (LN) and a charcoal trap immersed in liquid helium (LHe) before finally reentering the cryostat. Activated charcoal, a highly porous material, has a large surface area available for the adsorption of foreign substances; this makes it an excellent filter of non-helium chemicals when it is cooled down to cryogenic temperatures. Helium has a vapor pressure far higher than other elements at 4.2 K, so after passing through the LHe trap our circulating gas is quite pure. This minimizes the risks of non-helium elements freezing and blocking circulation lines in the refrigerator. Our circulation pump has rotary vanes magnetically coupled to the driving motor, a design that in theory should minimize oil pollution in the circulating mixture. In practice, however, some oil remains in the gas even after passing through glass wool and commercial oil filters, and we filter this oil with the LN trap to avoid overloading the LHe trap. During this experiment the system operated very cleanly; we found that we only had to clean (i.e. heat while pumping on the charcoal) the LN trap ~ once per month to avoid trap saturation.

3.2 How to Measure $Dy_2Ti_2O_7$ in a Toroidal Geometry

In Section 2.3.2 we described a theory that predicts the presence of a dilute gas of mobile "monopoles" in DTO at low temperatures. However, unambiguous

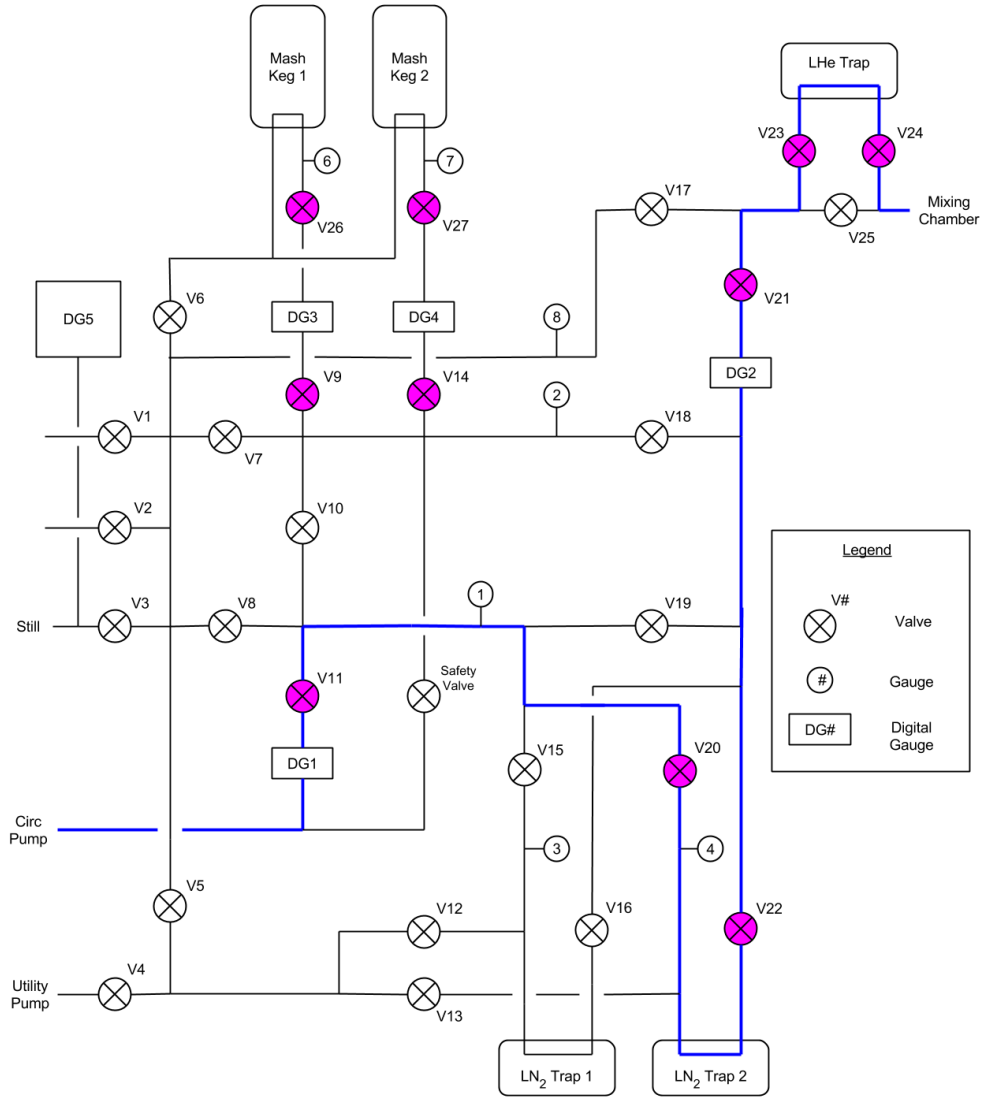

Figure 3.4: A schematic diagram of our gas circulation setup outside the cryostat. The valve configuration shown here is used during standard operation; white valves are closed and magenta valves are open. The path highlighted in blue is the path taken by circulating ^{3}He as it moves from the circulation pump to the cryostat. Valves near the storage kegs were left open so that the He mixture could enter them via a safety valve in the event of an unexpected overpressure.

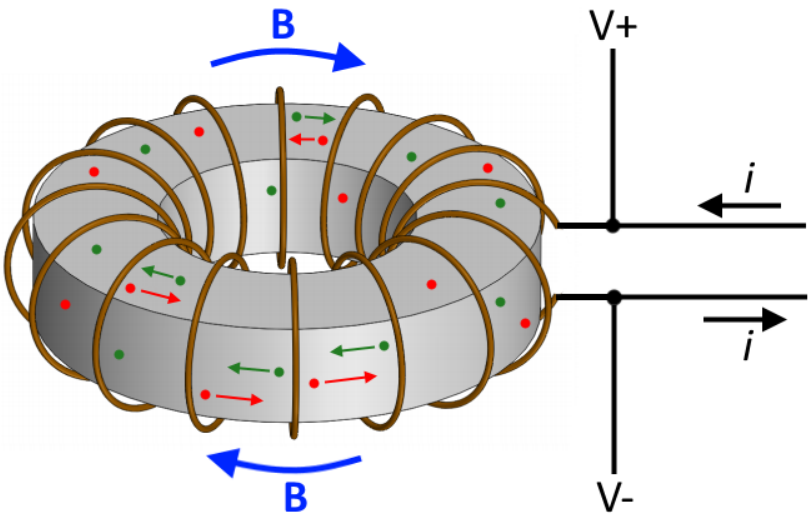

Figure 3.5: Schematic illustration of toroidal measurements of DTO dynamics. Superconducting wire is wrapped around a torus of DTO, and current running through this coil produces a toroidal magnetic field (blue arrows). This field drives positive (green dots) and negative (red dots) monopoles in opposite directions, producing twice the current of a single species. Changes in the DTO magnetization will produce a measureable EMF; we measure this signal and apply currents using a 4-probe I-V circuit configuration.

observation of the dynamics of such a state has proven difficult to achieve. We address this problem by introducing a novel high-precision measurement technique in a boundary-free topology. In conventional rod-shaped samples, the application of a magnetic field can be expected to simply move monopoles of opposite charge to opposite ends of the sample. In a toroidal geometry with a toroidal magnetic field $\mathbf{H}\hat{\phi}$, however, there are no crystal boundaries in the monopole trajectories. This is therefore the ideal topology with which to study the magnetic dynamics of these quasiparticles.

To study DTO in such a configuration, we performed measurements shown schematically in Figure 3.5. We wrap superconducting wire around a torus of single-crystal DTO, forming a "superconducting toroidal solenoid" (STS), and

with this STS we can simultaneously apply fields and measure EMFs resulting from the sample's magnetic dynamics. This setup has several important advantages: first, it removes crystal boundary constraints on DC monopole transport; second, the periodic boundary conditions of such a system minimize demagnetization factors that can complicate the analysis of magnetic measurements; and third, an azimuthal field $\mathbf{H}\hat{\phi}$ will drive oppositely-charged monopoles in opposite directions, generating a net current that should dramatically affect the observed dynamics.

The samples used in this experiment were synthesized using an optical floating-zone technique by the group of Graeme Luke at McMaster University. Sample boules were cut into disks with thickness ~ 1 mm and diameter ~ 6 mm; we then drilled holes of diameter ~ 2.5 mm in these disks to create DTO tori (Figure 3.6). Though DTO is fairly robust under compression, it is rather brittle and prone to shattering when subjected to machine cutting. To overcome this difficulty, we utilized diamond-tipped drills and used milling machines in Cornell's student machine shop to drill through the samples in increments of ~ 0.001". Though some samples were sacrificed while developing this process, we eventually raised the probability of sample survival to $\sim 50\%$ or higher. The Luke group generously provided a large number of samples to us, so we were able to successfully make several DTO tori.

After creating these tori, we then made the STSs by wrapping CuNi-clad NbTi wire (diameter 0.1 mm) around each sample. To efficiently make these coils, we applied dabs of super glue (Loctite 495) after every 3-4 coil loops until the STS covered the sample circumference; at that point we dipped the sample assemblies in Lakeshore varnish (VGE 7031, formerly known as "GE var-

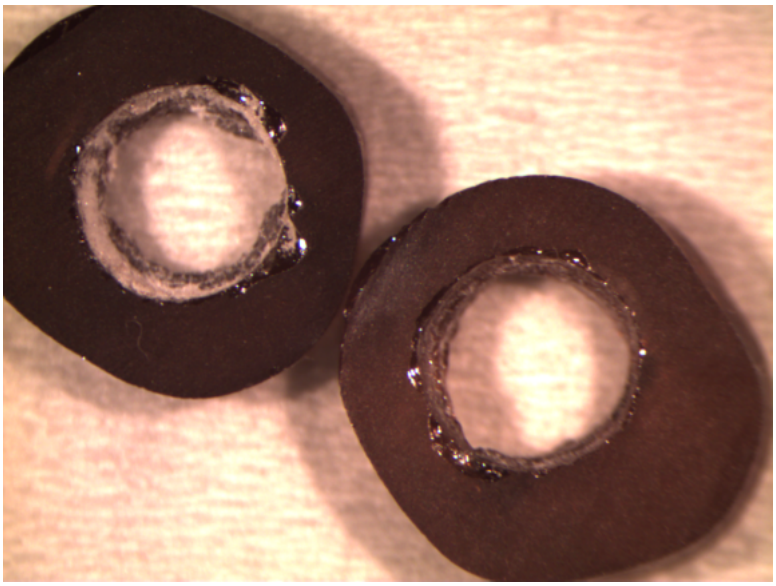

Figure 3.6: Two tori of DTO after completion of the drilling process. These tori have inner diameter ~ 2.5 mm, outer diameter ~ 6 mm, and thickness ~ 1 mm.

nish") to protect the wires. Figure 3.7 shows two samples wrapped in toroidal solenoids. The samples had some unavoidable irregularities in their shapes, so the wire loops in these solenoids do not all lie in a perfect single layer over the entire sample circumference. These irregularities do not substantially affect our measurements, as we found that the coils behave as inductors with inductances very close to what is expected from naïve geometrical considerations (Section 3.3.1). We also machined a torus from Stycast 1266 (Figure 3.8), a rigid non-magnetic epoxy, with dimensions similar to those of the DTO samples. In our parameter space we expect no significant magnetic activity from this material, so it was used as a control sample during initial tests of the experiment.

To achieve good signal strength we applied currents of ~ 25 mA in the STSs; if such a current were to go through a normal resistance of even ~ 0.1 Ω in the vacuum can it would produce milliwatts of heating power. At the very least this would eliminate our ability to achieve ultralow temperatures. In the vicinity of the heating source superconducting current-carrying wires could also poten-

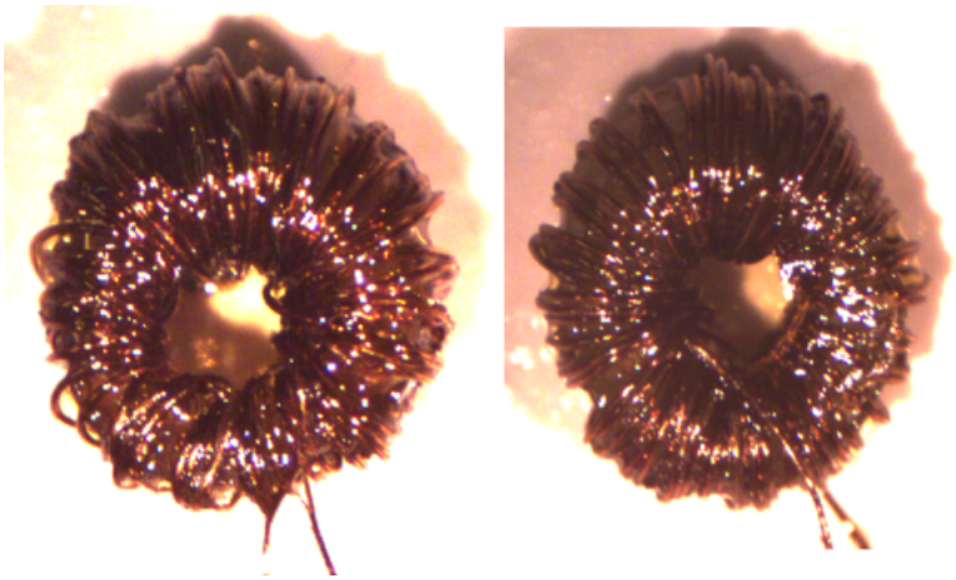

Figure 3.7: Two DTO samples after being wrapped with superconducting wire and dipped in Lakeshore varnish. The outer diameter of these samples is ~ 6 mm.

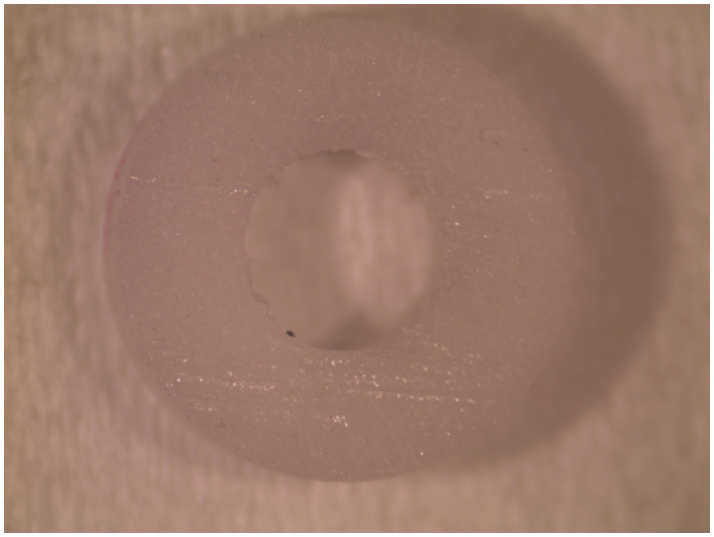

Figure 3.8: A torus of Stycast 1266 with dimensions similar to those of the DTO tori studied in this experiment. This sample was used for control tests after being wrapped in superconducting wire.

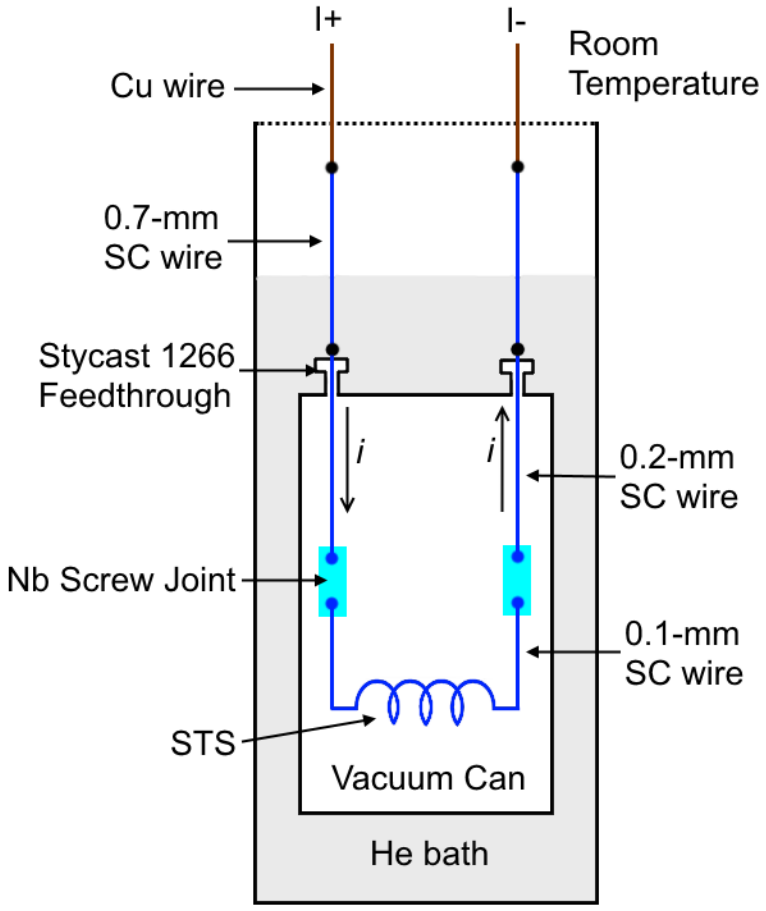

Figure 3.9: Schematic diagram of the wiring installed to satisfy the high current requirements of this experiment. Control instruments interface with Cu wires via hermetic feedthroughs at the top of the cryostat. The Cu wires are soldered to thick superconducting wires near the top of the storage dewar, and from there superconducting wires go down to the experiment. These wires go through the dewar space and liquid helium bath, enter the vacuum can via leak-tight feedthroughs made from Stycast 1266, and then connect to the STS wiring via superconducting niobium bars.

tially heat above T_c and become resistive, causing a large spike in resistivity and possible damage to the circuit from the subsequent surge in heat dissipation. The requirement of high current in a vacuum therefore dictates that the vacuum can circuitry be constructed from superconducting elements.

To accomplish this we installed wiring shown schematically in Figure 3.9.

Control instruments connect to room-temperature hermetic feedthroughs located at the top of the cryostat. From there copper wires go down into the dewar space, where they connect to 0.7-mm diameter, CuNi-clad NbTi wires; this thickness was chosen to minimize heat dissipation due to currents (a decreasing function of wire diameter) while providing relatively weak thermal links (an increasing function of diameter) to the warm upper dewar space. These relatively thick wires go into the helium bath and connect to 0.2-mm diameter, CuNi-clad NbTi wires via additional solder joints. The thinner wires then travel into the vacuum can via a homemade cryogenic vacuum-tight feedthrough (Figure 3.10) and eventually terminate at niobium screw pads. Wires from the STS terminate at the other ends of these pads, and by exposing the superconducting wire cores and pressing them tightly onto niobium sheets we achieved low-dissipation wire connections within the vacuum can. We found that we could apply currents of ≈ 30 mA to the STSs while remaining near the fridge base temperature (~ 20 mK), allowing us to achieve good signal strength during our subsequent measurements.

After making the STSs, we mounted them with Lakeshore varnish on the experimental apparatus shown in Figure 3.11A. Experimental temperatures were measured with a RuO_2 ("Rox") thermometer from Lakeshore Cryotronics, and cryogenic coaxial cable (also from Lakeshore) carried EMF signals to hermetic feedthroughs at the top of the cryostat. The experiment was placed on a hexagonal insert (Figure 3.11B) attached to the bottom of the mixing chamber plate. The experimental structures and mixing chamber insert were assembled from gold-plated copper components; these parts were machined by the department machine shop (see Appendix A for machine drawings) and electroplated by Anoplate Corporation in Syracuse. We observed that thermometers on the mix-

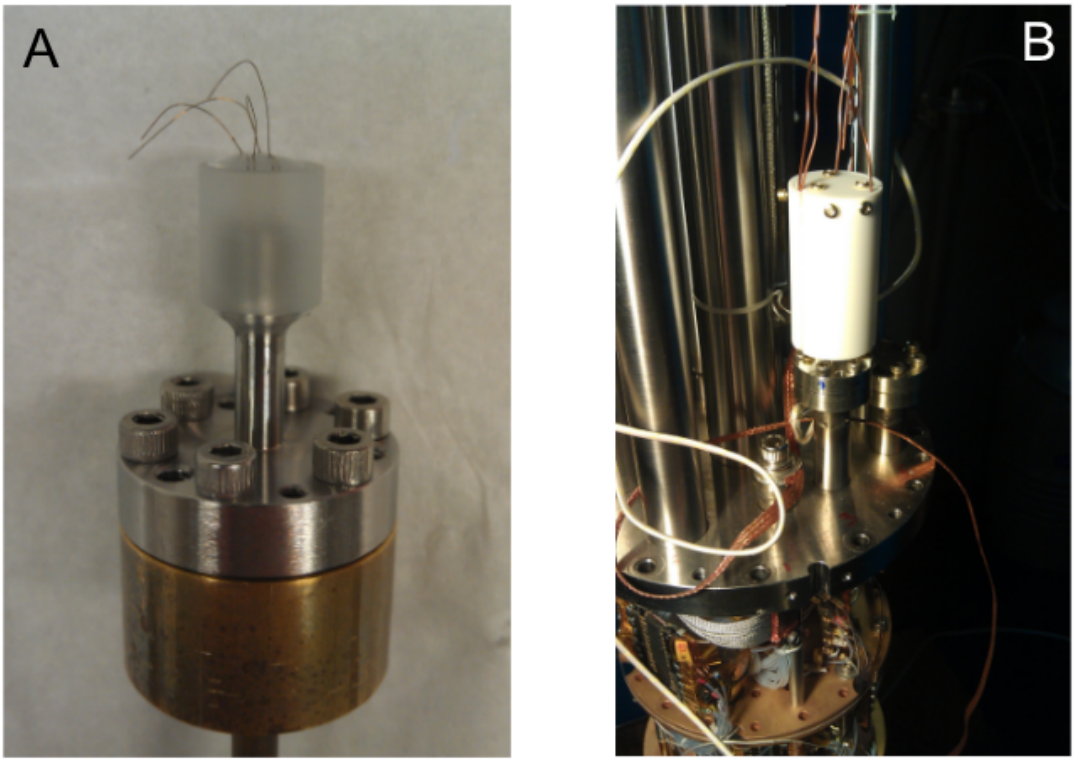

Figure 3.10: (A) Prototype of the hermetic cryogenic feedthrough used to feed high-current wires into the vacuum can. A cap machined from Stycast 1266 fits tightly around a stainless-steel tube and is sealed with the addition of more Stycast 1266. The steel piece mates with a flange on top of the 4K plate. **(B)** The feedthrough after installation on our cryostat; four wires go from the dewar space into the vacuum can. The assembly is protected by an outer shell made from macor.

ing chamber plate and experiment tracked each other well during refrigerator cooldowns, indicating that the new structures had good thermal contact with the mixing chamber.

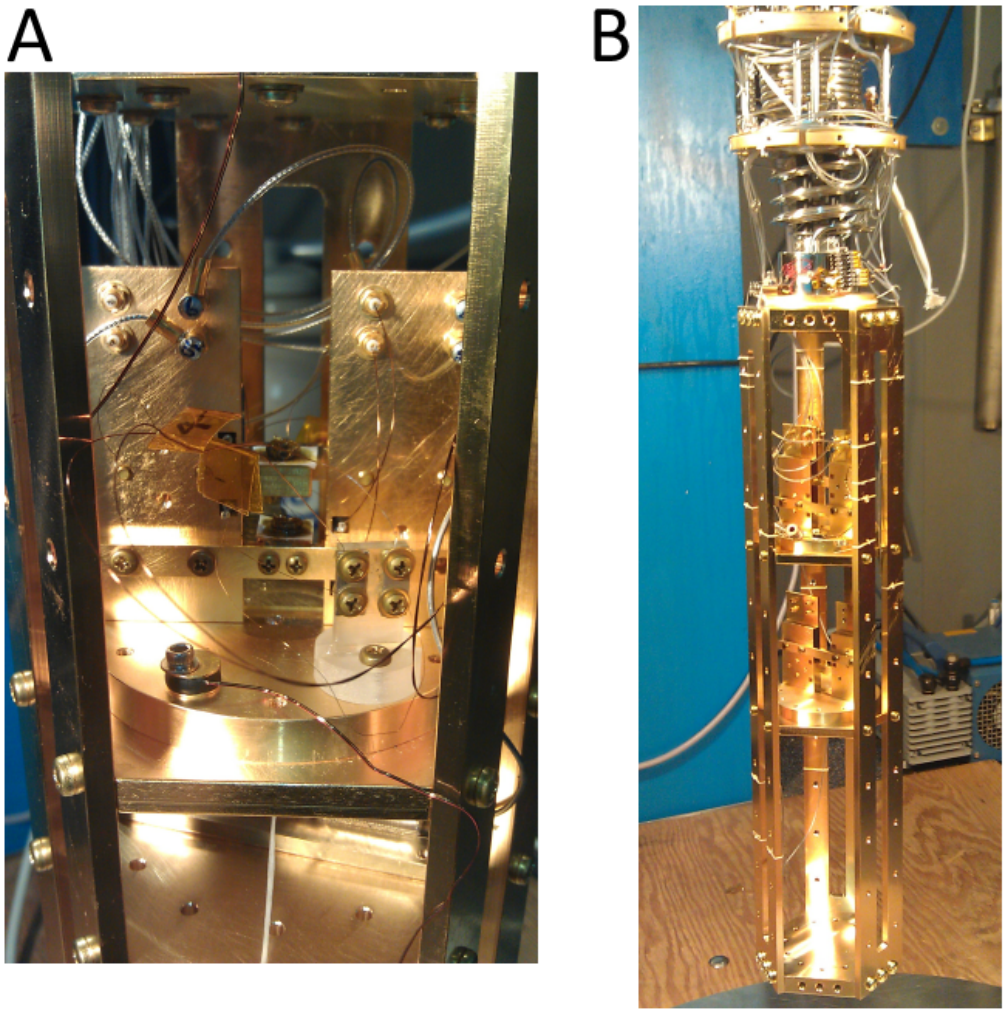

Figure 3.11: (A) Fully-assembled experimental apparatus for the measurement of DTO dynamics. Two samples (center) can be mounted on each assembly. The samples are mounted on the experiment with Lakeshore varnish, and each STS connects to current-carrying wires via a niobium screw pad (right of center) and to EMF-measuring coaxial wires (above center) via a short segment of superconducting wire. A RuO_2 thermometer (below and left of center) is used to measure experimental temperatures. **(B)** Experimental insert mounted on the bottom of the mixing chamber plate. The insert has plenty of space for experiments, with ≈ 18″ of vertical clearance and ≈ 4.5″ of horizontal clearance. The open hexagonal structure offers good mechanical stability while keeping installed experiments accessible for alterations.

3.3 Initial Experimental Tests

3.3.1 AC Measurements

Our AC measurements, shown schematically in Figure 3.12, used two lock-in amplifiers. One amplifier (Signal Recovery model 7265, "lock-in #1") functioned as the current source and measured the EMF across the STS under examination, and the second amplifier (Stanford Research Systems model SRS830, "lock-in #2") measured the voltage drop across a 10-Ω resistor placed in series with the STS. All measurements were referenced to the lock-in #1 reference function; this allowed us to measure the EMF with a well-defined phase. The 10-Ω resistance and 50-Ω oscillator output impedance are much larger than the low-temperature resistance of the cryostat current circuit (Figure 3.9), so during our experiments the lock-in oscillator functioned as a stable current source. We applied AC currents with amplitudes as high as 30 mA, resulting in applied fields ~ 1 G or less. Our measurements were therefore taken in the low-field limit $\mu B << k_B T$.

After installing the experiment and cooling the dilution refrigerator, we tested the critical current I_c of our STS assemblies by increasing the lock-in #1 output voltage while measuring our actual applied current with lock-in #2. When an STS remains superconducting, the 10-Ω resistor and 50-Ω output impedance of the lock-in oscillator combine to give an effective circuit resistance of $R_{eff} = V_{osc}/I \approx 60\ \Omega$. A substantial increase of R_{eff} indicates the onset of normal resistance in a sample assembly due to applied currents $I > I_c$. We performed these tests at our maximum measurement temperature $T = 3$ K, where I_c is at a minimum, and during our measurements we always used currents $I < I_c(3\text{ K})$ to ensure that the STSs remained in the superconducting state.

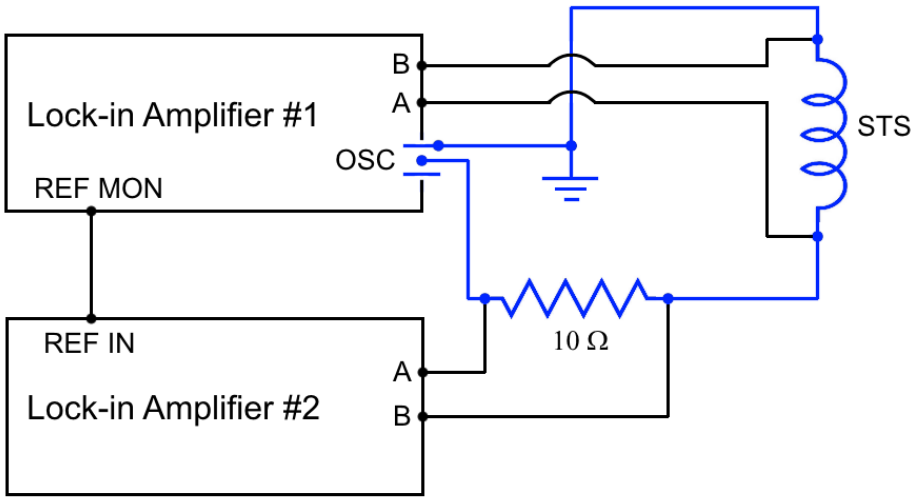

Figure 3.12: Schematic diagram of the measurement circuit used for AC dynamics experiments. The oscillator of lock-in amplifier #1, which functions as a current source here, is connected to a 10-Ω resistor. Currents of up to 30 mA run through this resistor and the STS before going to ground (blue path). A second lock-in amplifier measures the voltage across the resistor and functions as a low-noise current meter.

Before deducing anything about DTO dynamics, we first needed to perform some test measurements to understand what exactly we were observing in this novel setup. From the Maxwell-Faraday law, $\nabla \times \mathbf{E} = -d\mathbf{B}/dt$, changes in the applied field $\mathbf{H}(t)$ and the sample magnetization density $\mathbf{M}(t)$ generate an EMF in the STS:

$$\mathbf{V} = -\mu_0 NA\left(\frac{d\mathbf{H}}{dt} + \frac{d\mathbf{M}}{dt}\right) \tag{3.1}$$

where N is the number of coil turns in the STS and A is the effective cross-sectional area of an STS loop. Our measured signals have a complex form $V = V_x + iV_y$, where the phase of the applied current is defined to be zero. If we were measuring vacuum we would still expect a non-zero signal, since $d\mathbf{H}/dt$ is non-zero for an applied AC current. Previous susceptibility measurements have indicated that DTO has negligible magnetic activity (i.e. $\chi \to 0$) in our measured frequency range of 2-10000 Hz at temperatures of several hundred mK [61]; we

therefore measured STS signals at 50 mK to characterize background EMFs from the measurement circuit itself. All AC data points presented in the following figures are the averages of dozens or hundreds of lock-in readings taken with time separations of $5\tau_{amp}$, where τ_{amp} is the lock-in time constant. For measurements below 10 Hz we set $\tau_{lock} = 3$ s, and at higher frequencies we used $\tau_{lock} = 0.3$ s.

Typical background signals are shown in Figure 3.13; we have observed similar behavior in three DTO samples and a stycast sample. The in-phase signal V_x (Figure 3.13A) indicates that we have indeed achieved very low dissipation in our sample assembly, with effective resistances $R_{eff} < 1$ mΩ throughout our parameter space. This dissipation may derive from the solder joints used to connect our EMF measurement wires to the STS leads; these connections were made to the resistive CuNi layer of the STS wires, and therefore some small amount of dissipation should be expected. An in-phase signal could also result from some non-trivial crosstalk with nearby metal surfaces. The electrical resistivity of CuNi alloys is essentially constant below 4 K [78], and the cross-talk due to our stable applied AC currents should be T-independent. We therefore expect that this background V_x can be subtracted from higher-T measurements to reveal DTO behavior.

The out-of-phase background signal (Figure 3.13B) also shows non-trivial behavior in our sample assemblies. At high frequencies the STS behaves like a simple inductor, with $V_y \propto \omega$. However, at low frequencies the EMF shows capacitive $1/\omega$ behavior, indicating that there is some effective capacitive coupling near our coil. The STSs were mounted on brass surfaces (wire insulation and Lakeshore varnish prevented electrical shorts), so it is quite possible that this capacitive behavior derives from the close proximity of the STS wires to a

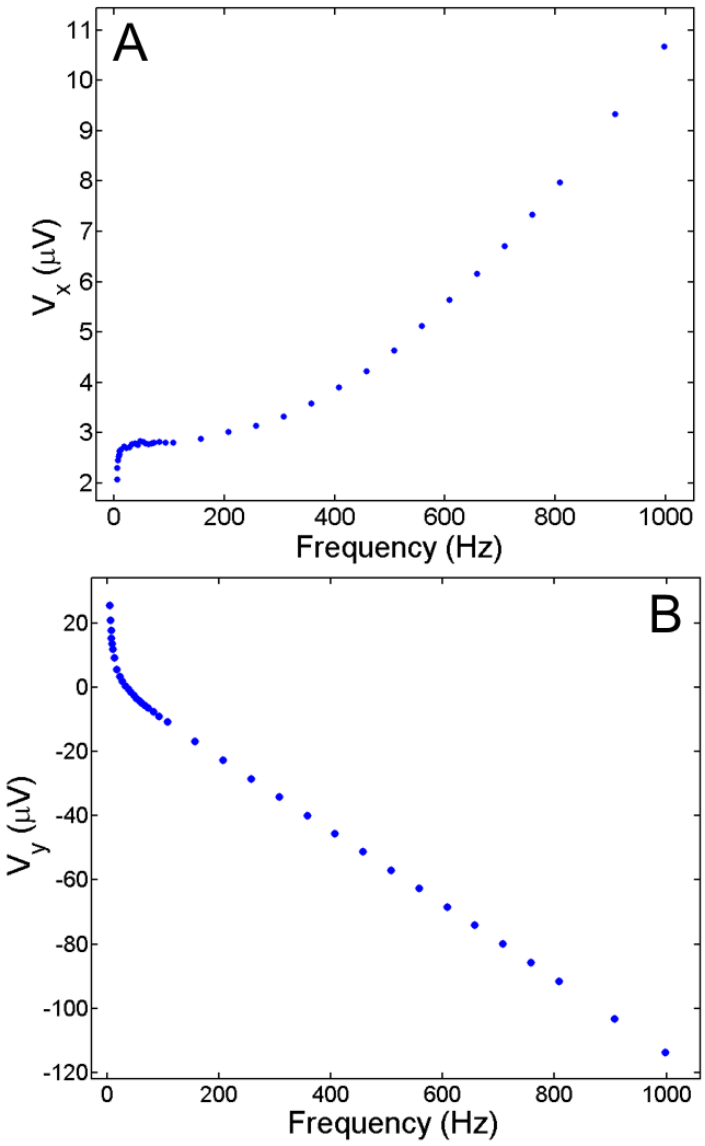

Figure 3.13: Typical STS background EMF measured at 50 mK with an applied current of 20 mA. **(A)** Background signals in phase with the applied current. Throughout the measured frequency range the effective residual resistance in the coil is quite small and < 1 mΩ. **(B)** Out-of-phase background signals. At high frequencies the STS EMF is $\propto \omega$, indicating that the system behaves as an inductor in this limit. At low frequencies the EMF has a capacitive form $\propto 1/\omega$; this likely derives from some capacitive coupling between the coil and nearby metal surfaces.

fairly large conducting surface. This EMF should only depend on the apparatus geometry and applied current, both of which do not change significantly with temperature; we therefore expect that, like V_x, the V_y background can be subtracted from higher-T signals to isolate DTO contributions.

Figure 3.14 shows typical DTO data with the 50-mK background subtracted. There is negligible signal change at temperatures as high as 0.5 K, while increasing the temperature by an additional few hundred mK reveals clear T-dependent behavior. This indicates that we can treat 500-mK data as a background, a realization that allows us to account for possible systematic effects more completely. To reach temperatures higher than $\sim$ 0.8 K we found it necessary to constrict the still in our dilution refrigerator before initiating temperature sweeps; this reduces the mixing chamber cooling power so that we can heat the experiment without applying dangerous currents to the resistive heater. Because of some mild hysteresis in the valve used to accomplish this constriction, different temperature sweeps were performed under different fridge conditions. We accounted for any fridge-related environmental frequency-dependent effects by starting every measurement at 500 mK and subtracting that background from higher-T measurements.

We performed similar measurements on a STS wrapped around a Stycast 1266 torus. Since Stycast 1266 is a non-magnetic material, it served as a good control sample with which we could uncover any T-dependent EMFs due to the experimental apparatus and circuit. As Figure 3.15 shows, we found no significant temperature dependence in the stycast EMF; as expected, we observed no indicators of magnetic dynamics in a non-magnetic sample. We therefore conclude that the proper empirical quantity that derives from DTO dynamics is

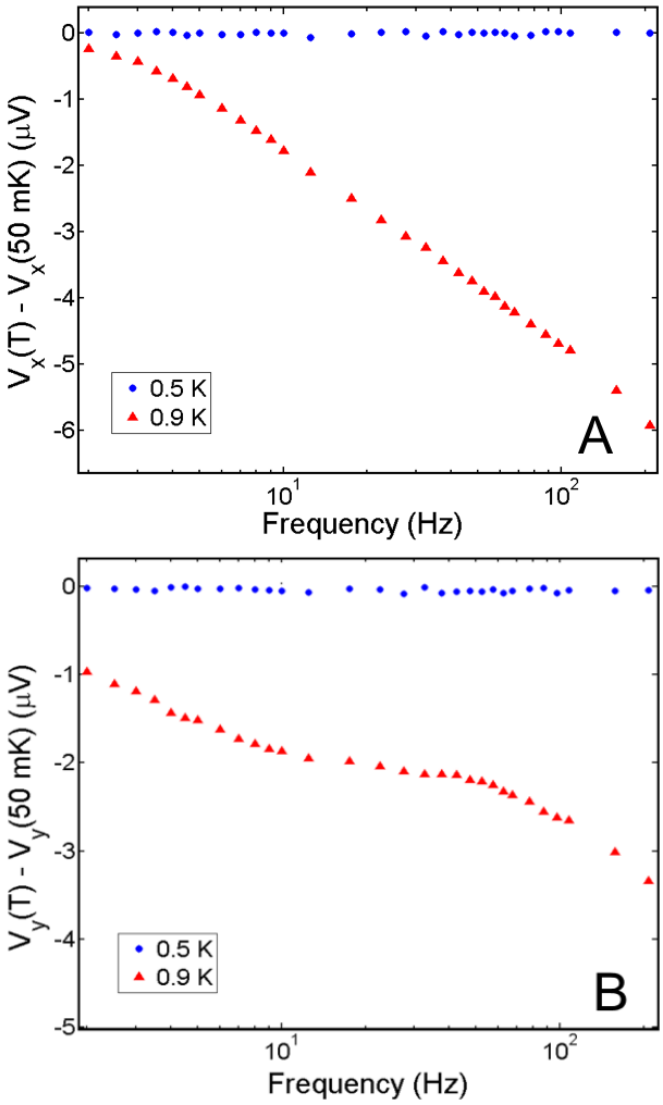

Figure 3.14: (A) In-phase and **(B)** out-of-phase DTO EMF data after subtracting the 50-mK background data. Signal changes are negligible at 0.5 K in our frequency range, while at 0.9 K we can see very clear T-dependent EMFs.

ΔV, the *change* of the STS EMF from its low-temperature behavior; this removes the contribution of the T-independent applied field from Equation (3.1).

The results of the stycast measurements show that our experimental geometry does not vary significantly in the measured temperature range; any temperature dependence of ΔV derives solely from the behavior of the DTO magnetization. The background EMF does have a nontrivial frequency dependence

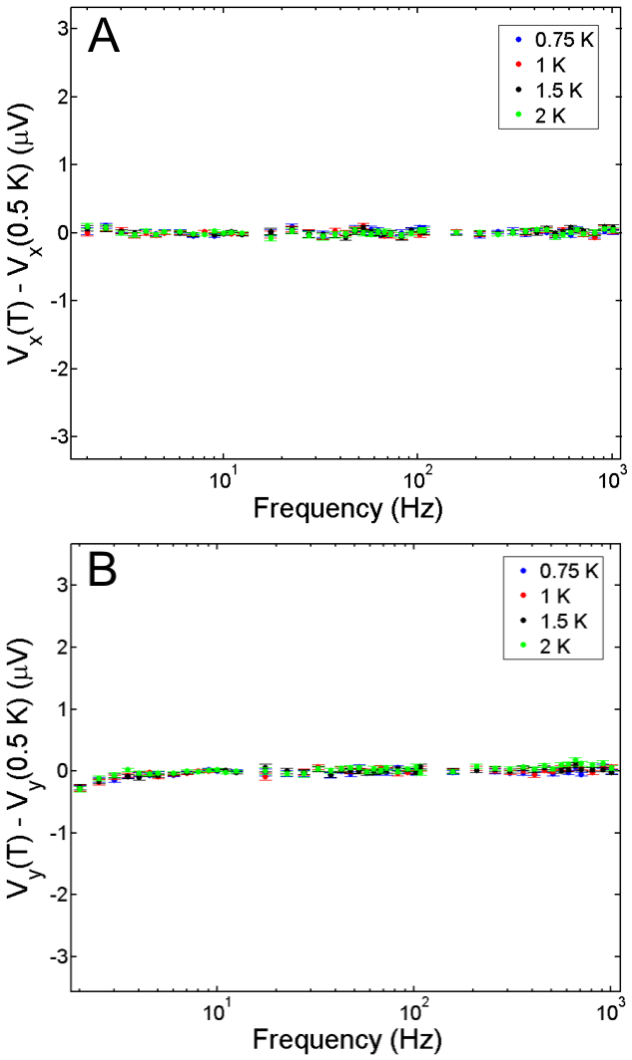

Figure 3.15: (A) In-phase and **(B)** out-of-phase EMF data taken on a Stycast 1266 sample after subtracting the 500-mK data. The T-dependent signal in this control sample is negligible, indicating that the T-dependent signals observed in DTO samples are real effects of DTO dynamics.

(Figure 3.13), but this does not contribute to DTO signals because each sample is contained entirely inside its solenoid coils. It follows from the Maxwell-Faraday equation, $\nabla \times \mathbf{E} = -d\mathbf{B}/dt$, that coil EMFs deriving from changes within a sample depend only on the sample and the frequency-independent solenoid inductance $L = \mu_0 nNA$, where n is the turns per length of the STS. Variations of $\Delta V(\omega, T)$ due to changing frequencies and temperatures derive directly from the

behavior of the DTO magnetization $\mathbf{M}(\omega, T)$. In an applied AC field we expect that $\mathbf{M} = \mathbf{M}_0 \exp(i\omega t)$, and therefore $d\mathbf{M}/dt = i\omega\mathbf{M}$. From Equation (3.1) we can now write the exact temperature and frequency dependence of ΔV:

$$\Delta V(\omega, T) = V(\omega, T) - V(\omega, 0.5\text{ K}) = -i\mu_0 NA\omega\mathbf{M}(\omega, T) \tag{3.2}$$

We will later consider linear-response magnetization models of the form $\mathbf{M}(\omega) = \chi(\omega)\mathbf{H}(\omega)$. Equation (3.2) shows that $\Delta V \propto M$, so before applying linear-response theory to our measurements we must first verify that our EMFs are actually proportional to the applied field. As shown in Figure 3.16, this is an excellent approximation for our experiment; the only noticeable nonlinearities in ΔV occur at high frequencies, and they are $\sim$ 2-3% of the signal strength. We can therefore confidently apply linear response theories during our data analysis.

The microscopic relaxation times of DTO increase rapidly as temperatures are lowered below $\sim$ 1 K, so sample properties are very sensitive to temperature changes. It was therefore essential to verify that our sample did indeed reach the desired experimental temperatures. We determined thermalization times by taking lock-in amplifier readings for several hours after changing frequencies and temperatures; Figure 3.17 shows a typical STS response during these measurements. After frequency changes the EMF readings settled almost immediately to values that were stable for hours. After temperature changes we observed relaxation to long-time stable values that took less than 10 minutes; to accommodate this behavior we waited at least 15 minutes after every temperature change during our temperature sweeps.

To complete our initial AC tests, we measured STS signals at very low temperatures for frequencies $\sim$ 50 kHz, far above the frequency bandwidth where any kind of DTO dynamics occur. As we found earlier (Figure 3.13), at

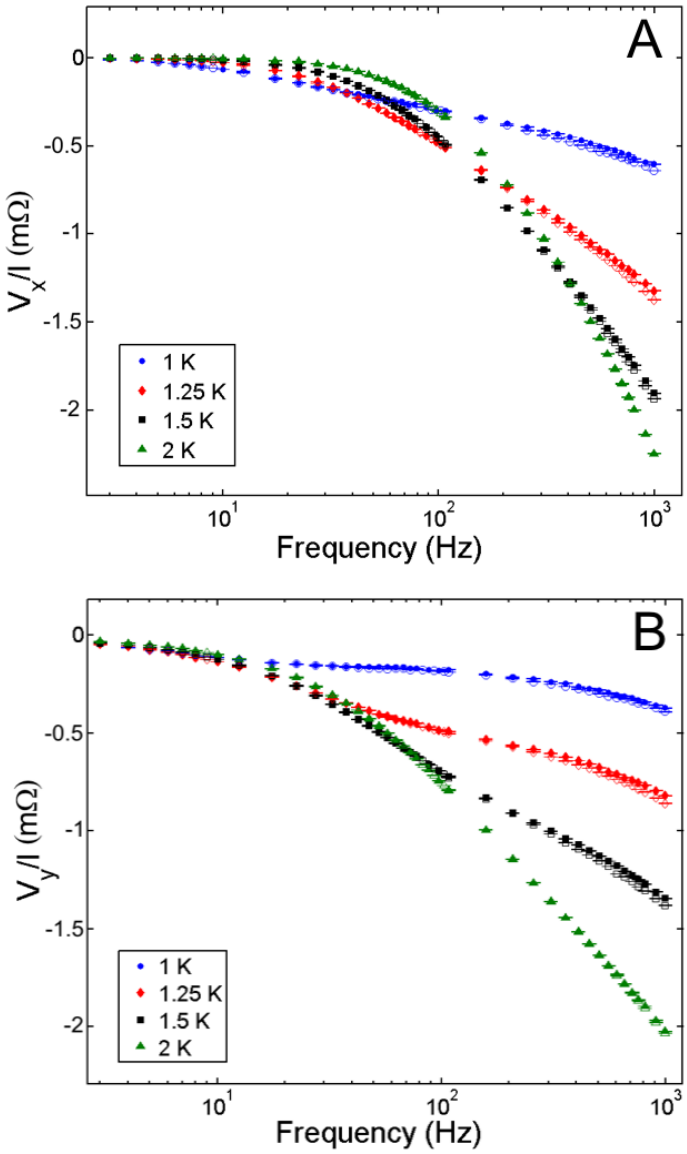

Figure 3.16: **(A)** In-phase and **(B)** out-of-phase DTO EMFs divided by the applied current amplitude I, giving effective resistances $R = \Delta V/I$. EMFs resulting from applied currents of 10 mA (filled symbols) and 20 mA (open symbols) give very similar results for R, with small non-linearities ~ 2-3% of the signal size at high frequencies.

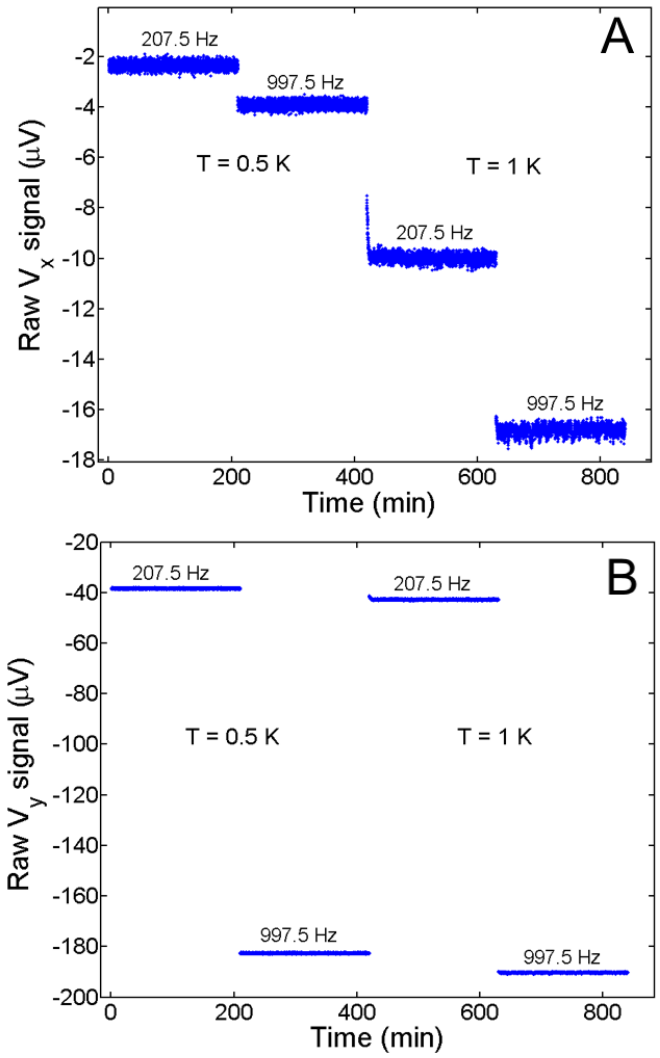

Figure 3.17: Time series of **(A)** in-phase and **(B)** out-of-phase DTO EMFs during a sequence of frequency and temperature changes. The AC signals settled to stable long-time values within a few seconds after frequency changes and within 10 minutes after temperature changes.

high frequencies our STSs behave very much like conventional inductors with $V_y = -I\omega L$. We determined an effective geometric inductance L from the slope of our very linear high-f data (Figure 3.18); the calculated inductances for the three measured DTO STSs were between 1 and 2 μH, in line with expectations from the geometry of the samples and coils.

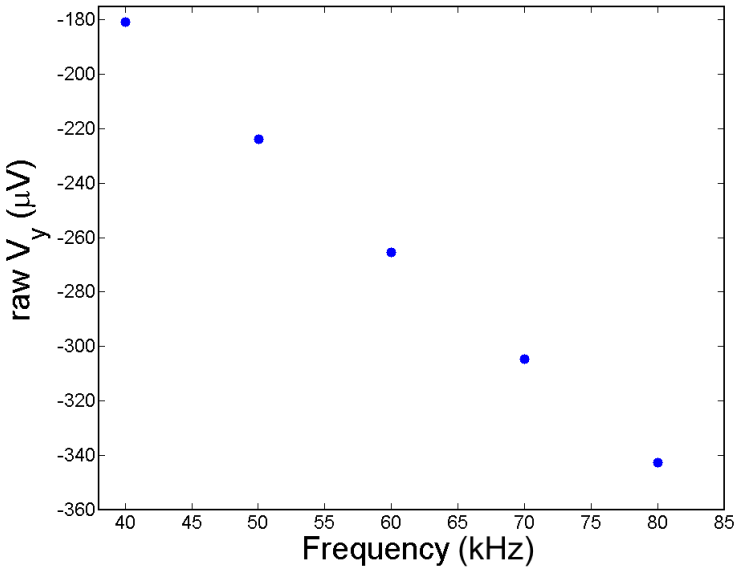

Figure 3.18: Out-of-phase EMF in a DTO STS at very high frequencies with an applied current of 0.5 mA at 30 mK. At these frequencies the capacitive contribution to the background EMF is negligible, and the STSs behave like standard inductors. We determine the inductance L from the slope of these linear high-f data.

3.3.2 DC Measurements

Our DC measurements, shown schematically in Figure 3.19, used the same 4-probe I-V circuit topology as the AC measurements. We used a function generator (Agilent model 33210A) to apply DC voltages, and once again we connected output voltages to a 10-Ω resistor. We used a dual-channel nanovoltmeter (Keithley model 2182A) to measure both the applied current (via the voltage across the resistor) and the STS EMFs. To resolve our signal it was necessary to sample the EMF at intervals of at least 1/60 s so that the nanovoltmeter could internally average its readings over an AC power cycle; this placed a hard lower bound on our time resolution and limited the measurement accuracy of signals that varied extremely rapidly. We probed the DC responses of our samples by measuring STS EMFs during the following current application protocol: first,

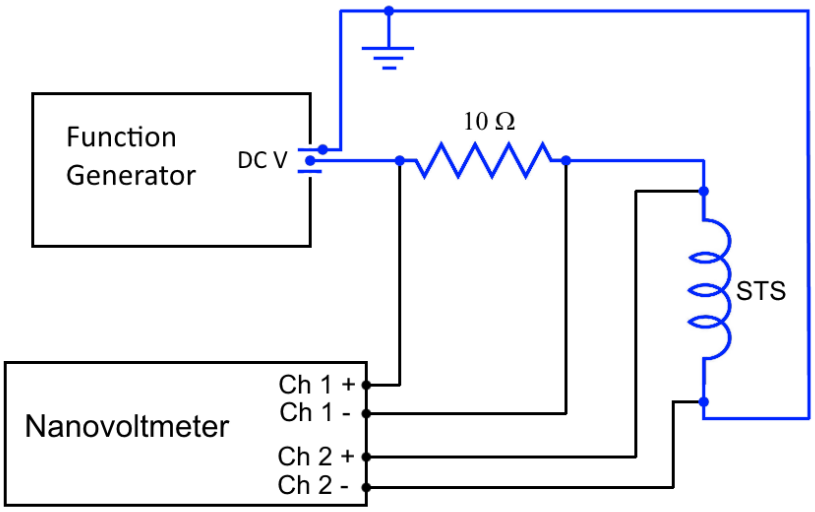

Figure 3.19: Schematic diagram of our DC measurement circuit. We used a function generator as a DC current source, and current flowed through a 10-Ω resistor and the STS on its way to electrical ground (blue path). We measured both the applied current and the STS EMF with a dual-channel nanovoltmeter.

turn on a current I for a time interval t_{dc}; next, turn off the current for t_{dc}; third, turn on the current in the reverse direction for a time t_{dc}; and finally, turn off the current for time t_{dc} and then repeat the cycle. We measured DC signals for time intervals up to $t_{dc} = 30$ s; measurements that lasted substantially longer than this began to be affected by background drift noise. We typically averaged hundreds of current cycles at a given temperature to achieve good statistics; typical STS responses are shown in Figure 3.20. After each current change, there is an initial spike followed by a longer decay with a T-dependent amplitude and relaxation time.

We first consider the STS responses in the long-time limit. The most objective way to study this limit is to take the difference of signals measured in opposite current polarities; this compensates for systematic offsets that are unrelated to the applied currents. Figure 3.21 shows that this analysis yields no significant

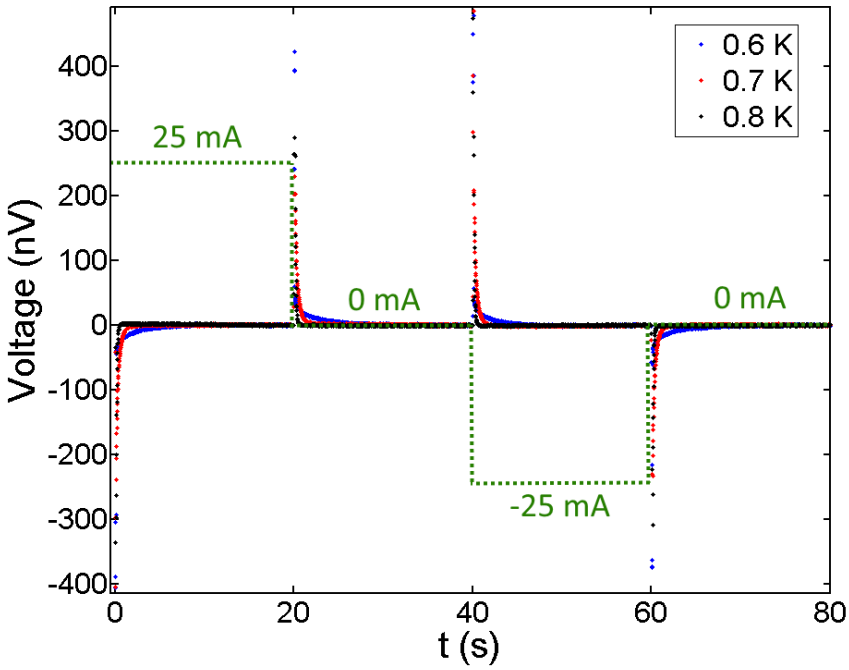

Figure 3.20: DTO responses during a current cycle (green dashed line) at several temperatures. Large signal spikes occur ≈ 60 ms after current changes; these signals are dominated by contributions from the measurement circuit. T-dependent decays due to DTO dynamics follow these spikes.

non-zero signal at long times within our experimental uncertainty. This is readily apparent from visual inspection of the decay curves in Figure 3.21A, and we can place quantitative limits on the signal by analyzing data taken at times long after the transients decay below our noise levels. Figure 3.21B shows the results of this analysis. There are two independent contributions to the total experimental uncertainty: statistical uncertainty ("white noise") due to thermal fluctuations and systematic drift noise ("pink noise") due to more correlated fluctuations. The averages of measurements at $t \geq 19$ s are spread around zero with no clear temperature dependence, indicating that the spread of these means is likely due to some small long-time drift in the STS signal. From the data in Figure 3.21B we find a drift noise estimate $\delta V_{drift} \approx 0.65$ nV, and the errorbars at each temperature give a statistical uncertainty $\delta V_{stat} \approx 0.4$ nV. We assume that these

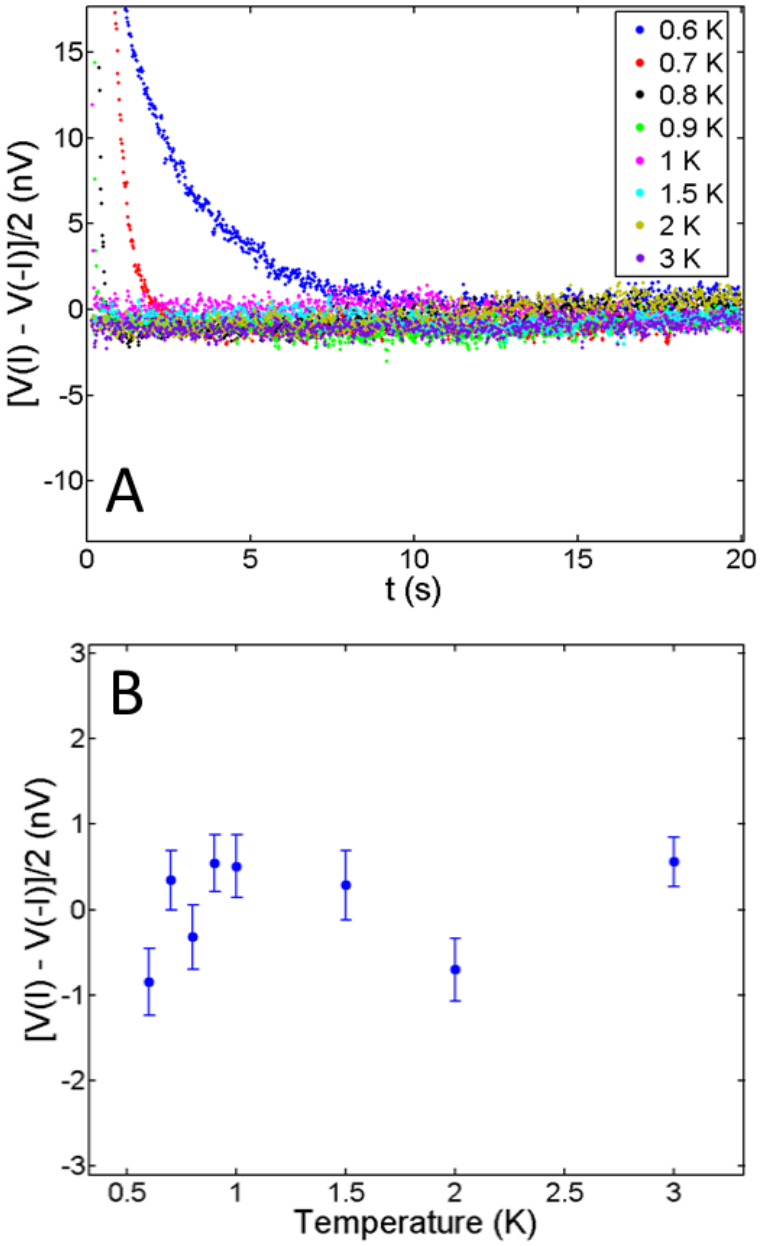

Figure 3.21: Long-time DC signals in DTO at temperatures ≤ 3 K. **(A)** Decay curves after taking the difference of responses to currents of opposite polarities. There is no indication that the transient DTO relaxation decays to a non-zero voltage at any temperature. This is more easily quantified in **(B)**, which shows the average and standard deviation of measurements at times $t \geq 19$ s. There is no clear temperature dependence in these results, indicating that their spread around 0 derives from drift noise.

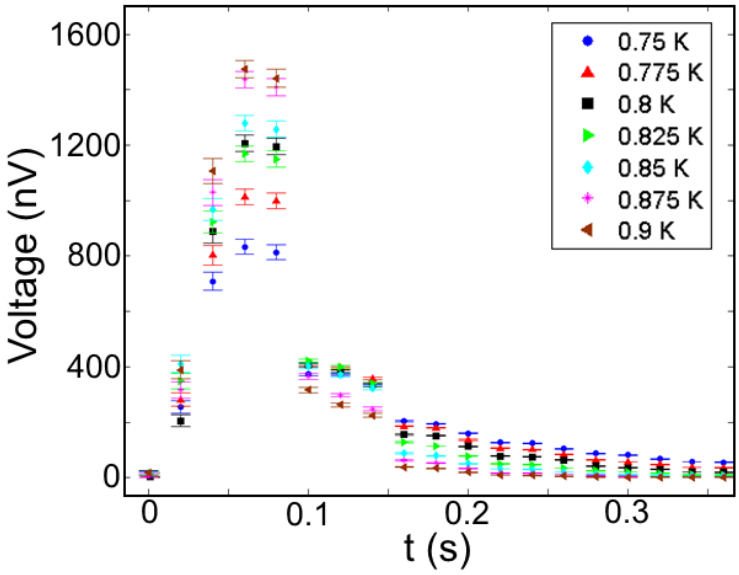

Figure 3.22: DC measurements at times immediately after turning off a 25-mA current at t = 0. After 200 ms the responses settle into smooth, T-dependent curves that can be accurately analyzed.

are independent sources of uncertainty, and therefore we conclude that there is no long-time DC signal within a total uncertainty of $\delta V = \sqrt{\delta V_{stat}^2 + \delta V_{drift}^2} \approx 1.5$ nV.

Since there is no significant long-time DC response, we compensate for the small drift noise by using current cycle time intervals t_{dc} substantially longer than the time it takes for transient relaxation curves to decay below our noise levels. We can then treat the long-time data $t \geq t_{long}$ of each curve as a background to be subtracted. For the rest of this work we plot and analyze the averages of N background-subtracted responses:

$$\bar{V}(t) = \frac{1}{N} \sum_{i=1}^{N} \left[V_i(t) - \bar{V}_i(t \geq t_{long}) \right]$$

Now we can accurately analyze the behavior of the STSs immediately after current changes; Figure 3.22 shows early-time DC responses in more detail. The initial signal spikes have some temperature dependence, but these spikes occur

at a T-independent time $t = 60$ ms; these data are influenced by some substantial systematic instrumental effects. The signals decrease extremely rapidly after reaching their maxima, and the nanovoltmeter time resolution limits our ability to measure these rapidly-changing EMFs. This causes the large discrete steps that we see between 80 ms and 200 ms before the responses finally settle into smooth, T-dependent decay curves.

The observed EMF is governed by Equation (3.1); there are contributions from a term proportional to $d\mathbf{H}/dt$ and a term proportional to $d\mathbf{M}/dt$. To disentangle the two sources we examined the DC behavior at 50 mK, where we expect DTO moments to be essentially frozen out on the timescales accessible to this experiment (Section 2.2). Figure 3.23 shows the low-temperature STS response after turning off an applied current. As in Figure 3.22 there is a large initial signal spike, but in this case there is no apparent subsequent decay; the signal rises and completely falls away within 100 ms. This indicates that the T-dependent longer decays in Figure 3.22 are due to DTO dynamics, while a large part of the initial EMF response derives from the circuit itself. From now on we will focus on DC data at $t \geq 200$ ms, since these longer-time signals can be resolved smoothly and are clearly dominated by the DTO dynamics we wish to examine.

So far we have only showed data taken after turning fields off. For very small applied fields we expect that switching the field on and switching the field off will produce the same EMF responses, aside from a polarity change. Figure 3.24 shows the difference between curves taken after turning on the field and curves taken after turning off the field. There are some moderate ($\sim 10\%$) differences between the responses at very early times, but these disappear quickly

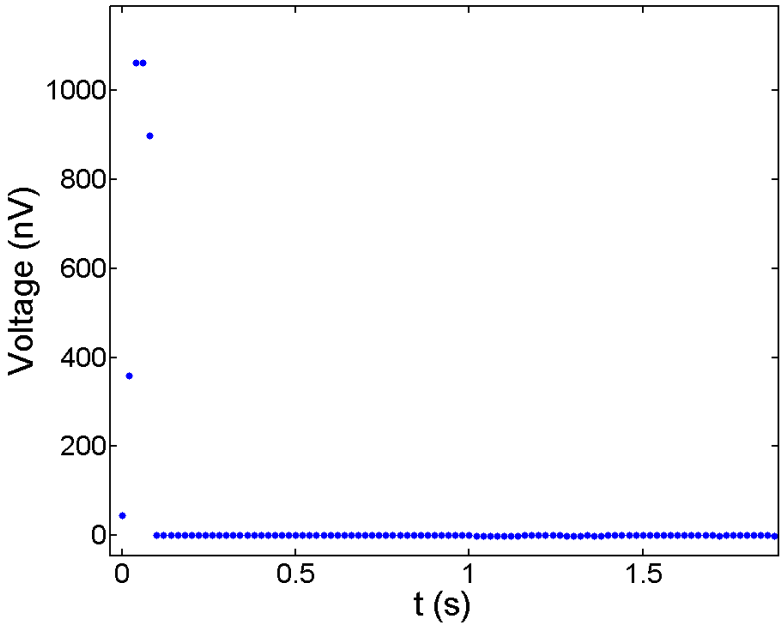

Figure 3.23: Response of a DTO STS at 50 mK after turning off a 25-mA current at $t = 0$. There is a large voltage spike at $t = 40 - 60$ ms that completely decays by $t = 100$ ms. There is no discernible longer-time decay after the large initial response.

and at $t \geq 200$ ms the curves are identical within our noise resolution. The expected current-switching symmetry does in fact exist in this measurement. We will continue to show only data taken after turning currents off, but Figure 3.24 shows that the physical content of the STS responses in different parts of our current cycles is exactly the same.

Standard time-domain linear response analysis relies on the assumption that we can write the magnetization as $\mathbf{M}(t) = \int_{-\infty}^{t} \chi(t-t')\mathbf{H}(t')dt'$, so that multiplying the applied field by α multiplies $\mathbf{M}$ (and its time derivatives) by the same factor α. Figure 3.25 shows the results of linear-response tests for our DC experiment. We find that for currents of at least 25 mA the observed DTO responses are linear in the current amplitude. We can proceed confidently with a linear-response analysis of the EMFs; we develop this theory further in the next chapter.

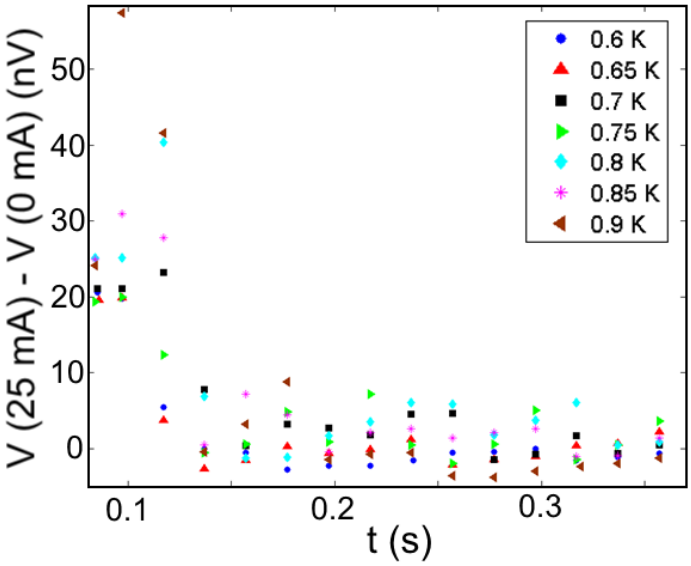

Figure 3.24: Difference between EMFs generated in response to turning a current on and turning a current off. There are some small differences in these response curves at very early times, but after 200 ms the responses are indistinguishable within our voltage resolution.

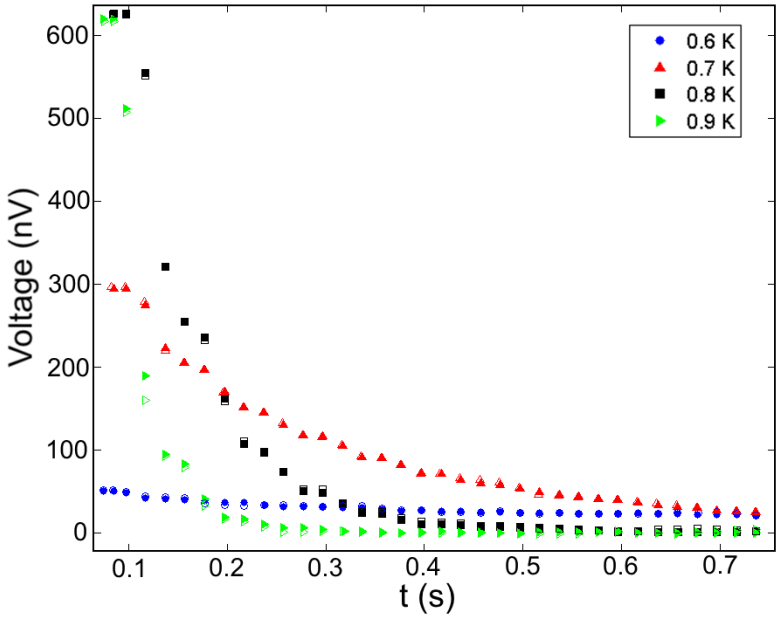

Figure 3.25: DTO relaxation curves after turning off applied currents of 12.5 mA (open symbols, multiplied by 2) and 25 mA (filled symbols). Doubling the applied current doubles the measured responses, indicating that we are operating in the linear response regime in this experiment. The linearity is so strong that the two curves essentially lie on top of each other.

CHAPTER 4

THEORY OF THE STS MEASUREMENTS

4.1 Measurements in the Time Domain

In Section 3.3.2 we showed that our DC measurements can be described by linear response theory with a magnetic susceptibility $\chi(t)$ and sample magnetization $\mathbf{M}(t) = \int_{-\infty}^{t} \chi(t-t')\mathbf{H}(t')dt'$. The EMFs we observe due to DTO dynamics are direct measurements of the time derivative of $\mathbf{M}$:

$$V(t) = -\mu_0 NA \frac{d\mathbf{M}}{dt} \tag{4.1}$$

In our DC measurement we apply fields of the form $\mathbf{H}(t) = \mathbf{H}_0\Theta(t)$, where $\Theta(t)$ is the Heaviside step function. The sample magnetization then becomes

$$\mathbf{M}(t) = \mathbf{H}_0 \int_0^t \chi(t-t')dt'$$

Taking the time derivative of this expression yields

$$\frac{d\mathbf{M}}{dt} = -\mathbf{H}_0\chi(t)$$

The applied field can be calculated using the solenoid expression $H = nI$, where n is the turns/length in the STS and I is the applied current. The EMF can then be written in terms of known experimental quantities and the DTO response χ:

$$\begin{aligned} V(t) &= (\mu_0 nNA)I\chi(t) \\ &= IL\chi(t) \end{aligned} \tag{4.2}$$

where L is the geometric inductance of the STS. This result shows that our DC measurements are direct probes of the DTO time-domain response to a magnetizing field $\mathbf{H}(t)$.

DTO has been predicted to host a delocalized neutral gas of monopoles (Section 2.3.2), and claims of the discovery and observation of such a state [59][64][79] have been accompanied by substantial interest in the possibility of "magnetricity" [79] analogous to standard electricity. Electricity can be driven in stable long-time currents; since our experiment is the first to have a topology that could in principle support such currents, we can examine how a stable DC "magnetricity" current would affect our measurements. It is important to note that the monopole transport equation of motion (Equation (2.15)) predicts zero DC current in the $t \to \infty$ limit; this is a consequence of the hard upper bound on DTO magnetization. However, developing the theory of a stable DC current is still an interesting exercise that may prove useful in future magnetic experiments.

We assume that any stable DC current can be described by Ohm's law with a *magnetic* conductivity σ_m: $\mathbf{J}_m = \sigma_m \mathbf{B}_m$. Since magnetic fields drive oppositely-charged monopoles in opposite directions (Figure 3.5), the total current in an applied field is

$$\mathbf{J} = \mathbf{J}_+ - \mathbf{J}_- = 2\mathbf{J}_+ = 2\sigma_m \mathbf{B}$$

The presence of stable DC magnetic currents would warrant the use of two modified Maxwell's equations: $\nabla \cdot \mathbf{B} = \mu_0 \rho_m$ and $\nabla \times \mathbf{E} = -\mu_0 \mathbf{J}_m$ [80]. Using the latter expression (the Maxwell-Faraday equation for magnetricity), the expected EMF from a single loop of an STS becomes $|dV| = 2\mu_0 A J_+$, and the total STS signal is $V = NdV = 2\mu_0 NAJ_+ = 2\mu_0 NA\sigma_m B$. We can therefore calculate the magnetricity conductivity from a stable DC EMF:

$$\begin{aligned} \sigma_m &= \frac{V}{2\mu_0 NAB} \\ &\approx \frac{V}{2\mu_0 IL} \end{aligned} \tag{4.3}$$

where we have made the substitution $B = \mu_0 H = \mu_0 nI$, which is a lower bound on B since for a macroscopic paramagnetic system we have $B = \mu_0(1+\chi)H \geq \mu_0 H$. During our DC measurements we found no evidence of any stable long-time DC signal larger than our uncertainty $\delta V \approx 1.5$ nV (Section 3.3.2; Figure 3.21). δV and Equation (4.3) place an upper bound on any magnetricity conductivity in DTO:

$$|\sigma_m| \leq (1.8 \times 10^4) \frac{\mathrm{A}}{\mathrm{m \cdot s \cdot T}}$$

Since we observed no significant stable monopole currents, we will focus on the transient decay curves during our full DC data analysis in Chapter 5.

4.2 Measurements in the Frequency Domain

In Section 3.3.1 we found that changes of the AC EMFs from their low-temperature values are direct measures of the sample magnetization:

$$\Delta V(\omega, T) = -i\mu_0 NA\omega M(\omega, T)$$

In a linear response medium $\mathbf{M}(\omega) = \chi(\omega)\mathbf{H}(\omega)$; inserting this into the above expression along with the solenoid relation $H = nI$ gives

$$\Delta V(\omega, T) = -iI\omega L\chi(\omega, T) \tag{4.4}$$

Equating the real and imaginary parts of this expression yields direct relations between the observables, V_x and V_y, and the DTO dynamics contained in $\chi = \chi' - i\chi''$:

$$V_x(\omega, T) = -I\omega L\chi''(\omega, T) \tag{4.5}$$

$$V_y(\omega, T) = -I\omega L\chi'(\omega, T)$$

Equation (4.5) is a *model-independent* expression for the observed EMF; any further deductions from the empirical data require assumptions about how to model $\chi(\omega, T)$. The EMF ratio $R \equiv V_x/V_y$, which is the arctangent of the EMF phase with respect to the applied current, reveals important differences in the predictions of different magnetization models. Using Equation (4.5), we can also write this quantity in the simple form $R = \chi''/\chi'$.

First we consider a Havriliak-Negami (HN) parametrization:

$$\chi(\omega, T) = \chi_\infty + \frac{\chi_0}{[1 + (i\omega\tau_{HN})^\alpha]^\gamma} \tag{4.6}$$

where τ_{HN} is a characteristic relaxation time, the exponents α and γ describe the spread and asymmetry of χ in frequency space, and χ_∞ is the purely real value of χ in the $\omega \to \infty$ limit. We previously introduced this function in the context of dielectric liquids (Section 1.2); it is a generalization of the standard Debye, Cole-Cole, and Davidson-Cole forms commonly used to fit relaxation data. Because it is the most general standard relaxation parametrization, the HN form is an unbiased and natural starting point for our analysis. The quadrature components of Equation (4.6) are

$$\begin{aligned}
\chi' &= \chi_\infty + \chi_0 \frac{\cos(\gamma\phi)}{\left[1 + 2(\omega\tau_{HN})^\alpha \cos\left(\frac{\pi\alpha}{2}\right) + (\omega\tau_{HN})^{2\alpha}\right]^{\gamma/2}} \\
\chi'' &= \chi_0 \frac{\sin(\gamma\phi)}{\left[1 + 2(\omega\tau_{HN})^\alpha \cos\left(\frac{\pi\alpha}{2}\right) + (\omega\tau_{HN})^{2\alpha}\right]^{\gamma/2}}, \\
\phi &= \arctan\left[\frac{(\omega\tau_{HN})^\alpha \sin\left(\frac{\pi\alpha}{2}\right)}{1 + (\omega\tau_{HN})^\alpha \cos\left(\frac{\pi\alpha}{2}\right)}\right]
\end{aligned} \tag{4.7}$$

These components readily give us a predicted EMF ratio:

$$R_{HN} = \frac{\chi''}{\chi'} = \frac{\sin(\gamma\phi)}{\cos(\gamma\phi) + \chi_\infty \left(1 + 2(\omega\tau_{HN})^\alpha \cos\left(\frac{\pi\alpha}{2}\right) + (\omega\tau_{HN})^{2\alpha}\right)^{\gamma/2}} \tag{4.8}$$

The temperature dependence of this prediction is contained in the relaxation time $\tau_{HN}(T)$. For modeling purposes we assume that τ_{HN} has a standard thermally-activated Arrhenius form, $\tau_{HN} = \tau_0 \exp(\Delta/k_B T)$; this turns out to be too simplistic for DTO (see Chapter 5), but it is a decent *a priori* assumption of the temperature dependence. Figure 4.1A shows the predicted EMF ratio for an HN susceptibility parametrization with $\alpha = 0.85$, $\gamma = 0.75$, and $\chi_\infty/\chi_0 = 0.001$, and Figure 4.1B illustrates the frequency dependence of R_{HN} at different temperatures.

Next we consider an EMF resulting from transport of the monopoles hypothesized to exist in DTO. In Section 2.3.2 we introduced the accepted equation of motion for monopole transport:

$$\frac{d\mathbf{M}}{dt} = Q_m n_m u \left(\mathbf{B} - \mu_0 \chi_m^{-1} \mathbf{M}\right)$$

Solving this equation in Fourier space gives an expression for χ that allows us to predict the emf ratio $R = \chi''/\chi'$. The historically-used but incorrect form for $\chi(\omega)$, which we call χ_B, has been used by some groups during attempts to analyze susceptibility data in past experiments [59][74]. This susceptibility, which neglects interactions and uses $\mathbf{B} = \mu_0 \mathbf{H}$ in its derivation, has a simple Debye form $\chi_B \propto 1/(1 + i\omega\tau)$ that predicts the following ratio:

$$R_B = \frac{\chi_B''}{\chi_B'} = \omega\tau \propto \omega$$

which is quite different from the HN parametrization prediction in Equation (4.8).

However, interactions are important in this system, so we are more concerned with the monopole susceptibility that takes them into account. Using the proper macroscopic field expressions everywhere in our susceptibility deriva-

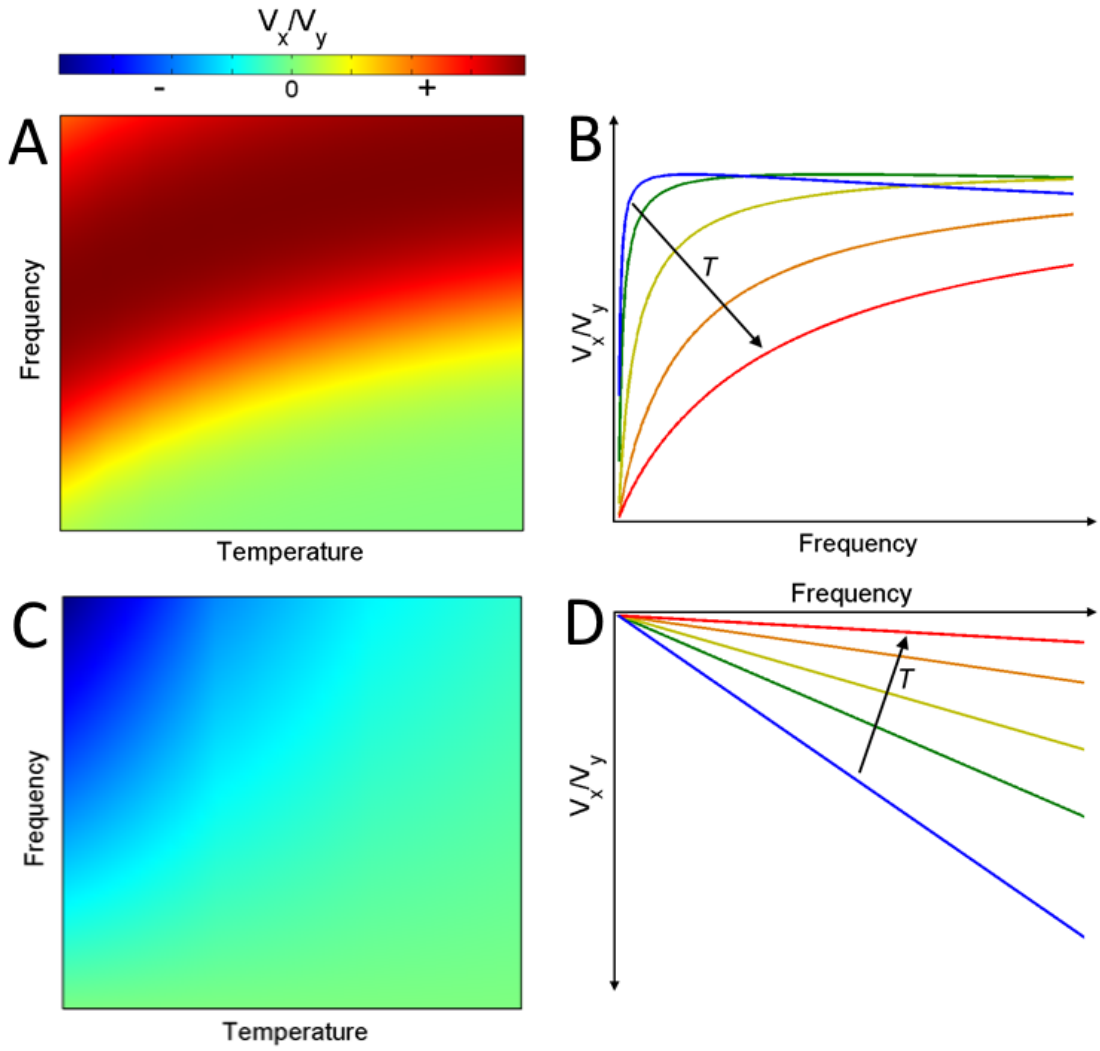

Figure 4.1: **(A)** Predicted EMF ratio for a HN susceptibility where τ_{HN} varies according to the simple Arrhenius expression $\tau_{HN}(T) = \tau_0 \exp(\Delta/k_B T)$. **(B)** Expected frequency dependence of R_{HN} at different temperatures. **(C)** Predicted EMF ratio for a susceptibility derived from a monopole transport model. The predicted R_{mpole} contrasts sharply with the HN prediction in (A). R_{mpole} has a different polarity, and it is linear in frequency. **(D)** Expected frequency dependence of R_{mpole} at different temperatures.

tion yields the result in Equation (2.17):

$$\chi_{mpole} \propto \frac{1}{1 - i\omega\tau}$$

The EMF ratio derived from $\chi_{mpole} = \chi'_{mpole} - i\chi''_{mpole}$ is given by $R_{mpole} = \chi''_{mpole}/\chi'_{mpole}$; this leads to the final monopole prediction:

$$R_{mpole} = -\omega\tau \propto -\omega \tag{4.9}$$

This result, shown in Figures 4.1C and D, is very different from what we derived for an HN parametrization. In addition to predicting an EMF ratio that is linear in frequency, a monopole transport model predicts that the EMF components V_x and V_y should have different polarities. This is a very definitive and concrete set of expectations, and it indicates that R is the first quantity we should examine during our AC data analysis.

CHAPTER 5

MEASUREMENTS AND ANALYSIS OF DTO DYNAMICS

5.1 Results of AC Measurements

We performed AC measurements on three different DTO tori; all tori exhibited the same behavior, so we present data from one torus in this chapter. In Section 4.2 we showed that the ratio of EMF components $R = V_x/V_y = \chi''/\chi'$ is an excellent quantity with which to test the predictions of different magnetization models. The measured DTO EMF ratio is shown in Figure 5.1; comparison with Figure 4.1 immediately shows that HN relaxation *without monopole transport* is the most promising parametrization of DTO behavior. Our observations conflict strongly with monopole theory predictions; the data have a polarity opposite from what would be consistent with monopole transport, and the isothermal curves are certainly not linear in frequency. On the other hand, the color plot in Figure 5.1A and constant-T curves in Figure 5.1B are very close to HN predictions. Figure 5.1A does also indicate that the temperature dependence of τ_{HN} differs from simple Arrhenius behavior, but nevertheless it strongly points at HN parametrization as the best way to proceed with the remainder of our analysis.

We therefore calculated the DTO susceptibility $\chi(\omega, T)$ from the observed EMFs using Equation (4.5) and then fit χ to the parametrization in Equation (4.6); the data and fits are shown in Figure 5.2. Fits were performed using a least squares method that minimized the total squared error in the real and imaginary susceptibility components. HN relaxation clearly describes our AC data well over the entire measured parameter space, and to our knowledge this is

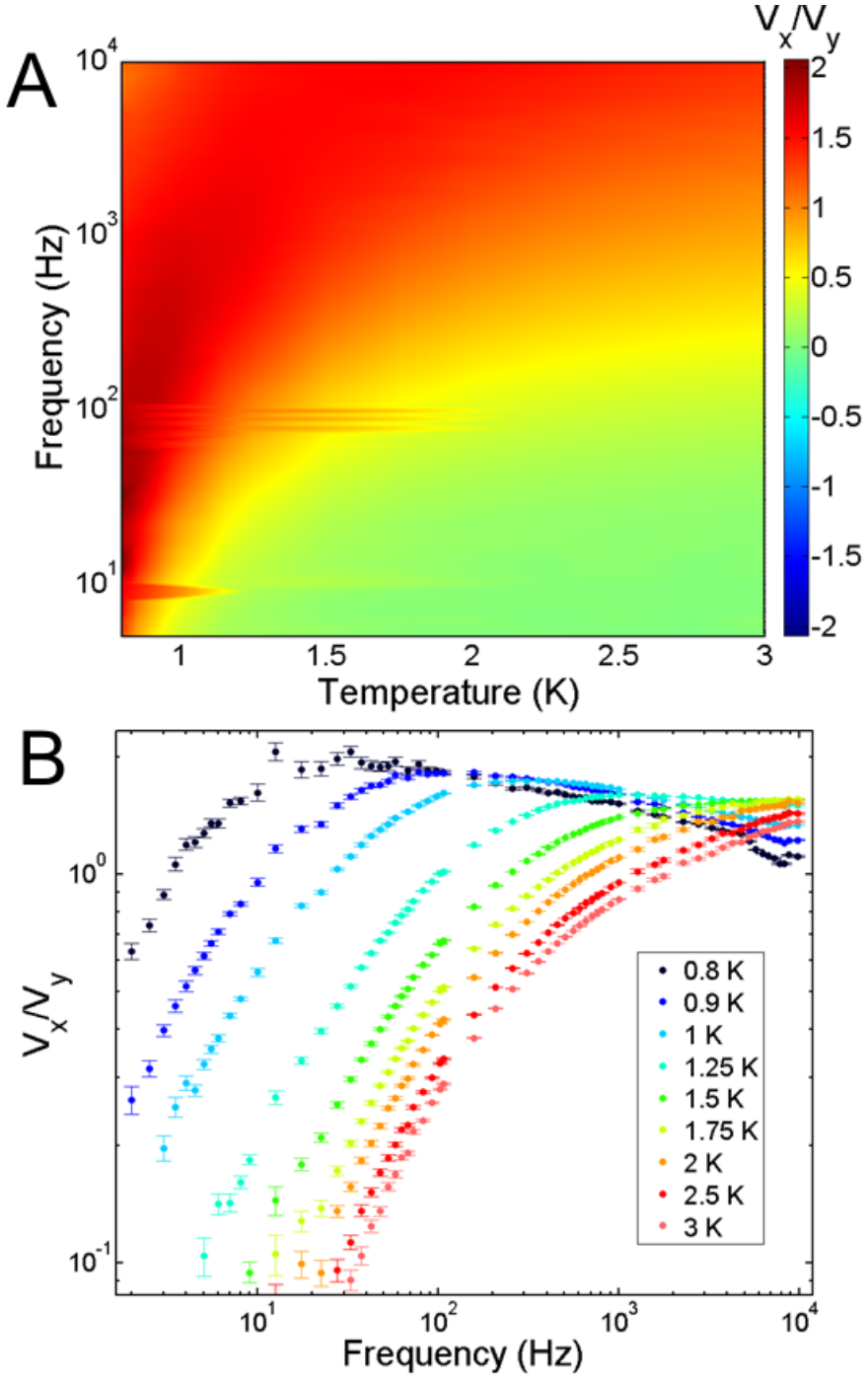

Figure 5.1: (A) EMF ratio V_x/V_y for DTO between 0.8 and 3 K at frequencies up to 10 kHz. **(B)** $R(\omega)$ curves at different temperatures. These results are consistent with expectations from a model with no monopole transport.

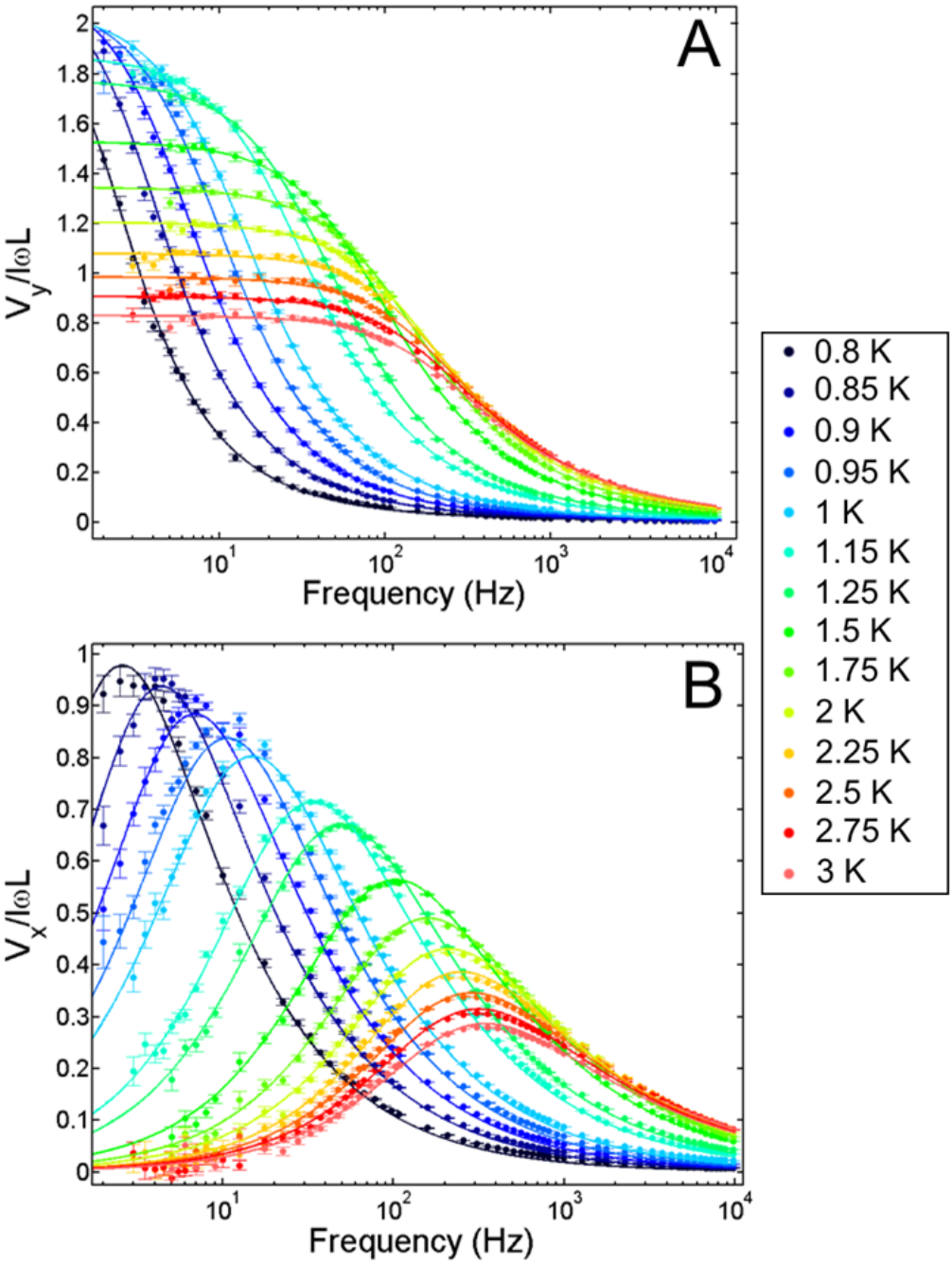

Figure 5.2: (A) Real and **(B)** imaginary parts of the DTO magnetic susceptibility calculated from our EMF data (symbols). The data are described very well by fits to an HN parametrization (lines) over the entire measured parameter space. Our susceptibility is very similar to what has been found during measurements on polycrystalline and single-crystal DTO samples.

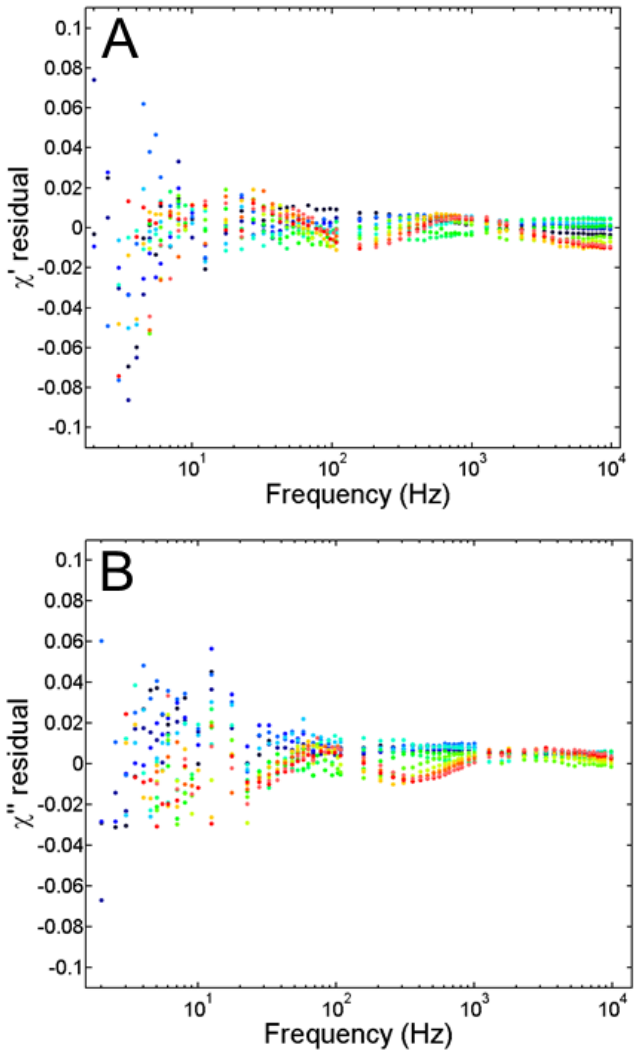

Figure 5.3: Residuals of fits to the **(A)** real and **(B)** imaginary parts of the magnetic susceptibility. Both components have residuals ~ a few percent or less of the signal size, quantitatively confirming the high quality of the HN description of $\chi(\omega)$.

the first time that a single self-consistent parametrization has successfully characterized both components of the DTO susceptibility over a wide temperature range. The quality of these fits is reflected in the small size of the fitting residuals (Figure 5.3); in both components they are a few percent or less of the measured signal. Below $f = 2$ Hz, noise levels became too large to be dealt with by experimentally-reasonable averaging times. Resolving the peak in χ'' is essen-

tial to getting fits that have physically-meaningful parameters, so we limit our analysis to $T \geq 0.8$ K, where the peak occurs at $f > 2$ Hz.

The values of the HN fit parameters are shown in Figure 5.4. The exponents α and γ are both less than 1 throughout the measured temperature range, indicating that the simplest relaxation parametrizations do not capture the full extent of DTO dynamics. α is relatively stable and remains at values ~ 0.9 below $T = 3$ K. γ has a substantially stronger temperature dependence, and it actually decreases at higher temperatures. This means that the asymmetry of $\chi(\omega)$ increases at higher temperatures; this has also been observed in single-crystal samples [61], and it may be a good test of the accuracy of microscopic models as the non-monopole theory of DTO develops (see Chapter 6). We note that uncertainties in α and γ are higher below 1 K because at these temperatures we do not have access to a large portion of the bandwidth below the χ'' peak frequency. Since the HN exponents are sensitive to the spread and asymmetry of the χ'' peak, this limited low-f resolution decreases the precision of their fitted values near 0.8 K.

τ_{HN}, on the other hand, is highly constrained by the position of the peak in χ'', so our fits give precise information about the relaxation time even at the lower end of our AC temperature range. τ_{HN} has a non-trivial temperature dependence; we can clearly see in Figure 5.4B that it does not follow an Arrhenius form (a line on a $\log(\tau)$ vs. $1/T$ plot) typical of simple thermally-activated processes. We will consider this in more detail in Section 5.3. The limiting susceptibility χ_∞ decreases from ~ 0.007 at 1 K to ~ 0.001 at higher temperatures. In zero field the thermodynamics of spin systems on a lattice predict that $\chi_\infty \sim 1/T$ [9], so the general behavior of $\chi_\infty(T)$ is in line with expectations. χ_∞ is less than

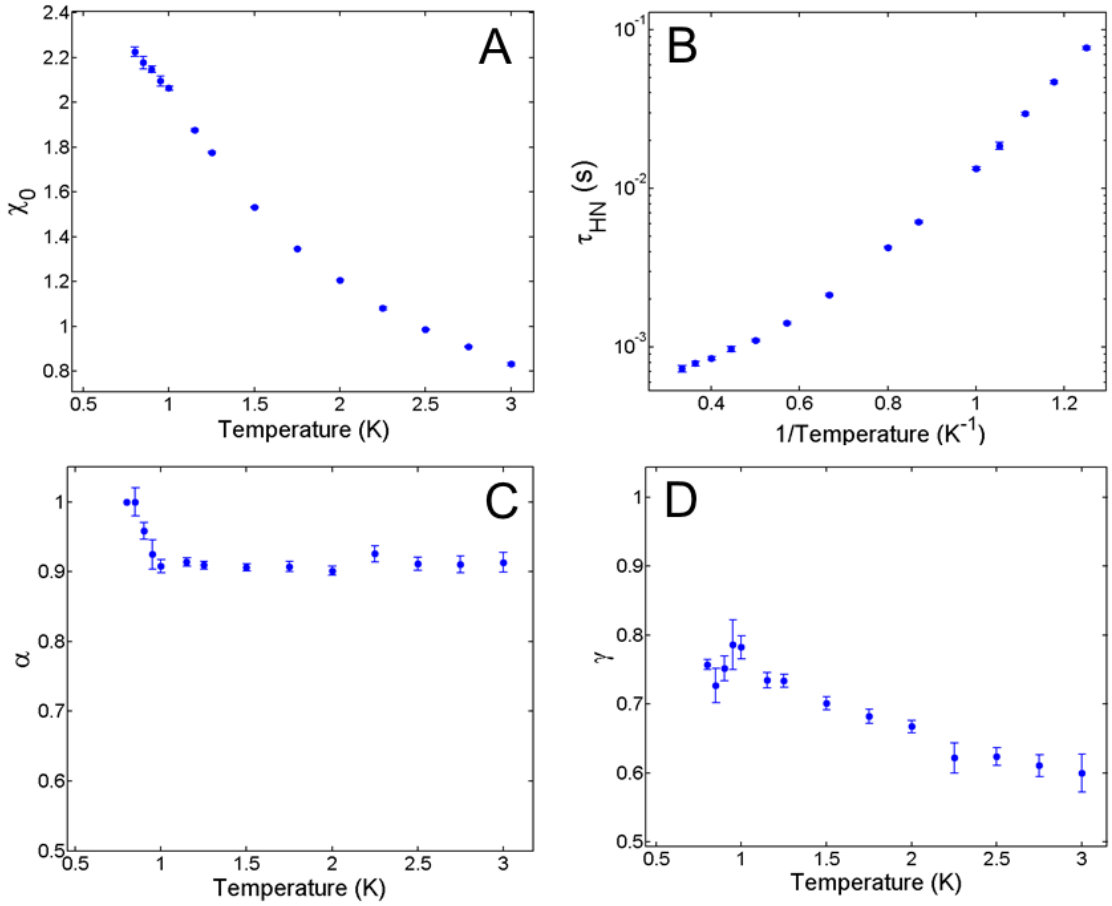

Figure 5.4: (A) Temperature dependence of χ_0, which gives the susceptibility in the $\omega \to 0$ limit. **(B)** Temperature dependence of τ_{HN}, a characteristic central relaxation time. τ_{HN} increases faster with decreasing temperature than would be expected for a standard thermally-activated process. **(C)** Temperature dependence of the HN exponent α, which characterizes the spread of χ variations in frequency space. α is stable at values ~ 0.9 throughout most of our measured temperature range. **(D)** On the other hand, γ shows significant temperature dependence. Both exponents are less than 1, indicating the presence of a complex landscape of excitations and dynamics in DTO.

0.5% of the full scale of χ' variations, so it plays a fairly insignificant role in DTO dynamics in our measurement bandwidth.

These parameter values allow us to show in a simple and striking manner that HN relaxation is a universal description of DTO dynamics. If a parametrization truly describes a set of data, there should be scaled variables

that collapse all isothermal data curves onto each other. For HN relaxation we start with the function in Equation (4.6) and separate the exponents:

$$\left(\frac{\chi' - i\chi''}{\chi_0}\right)^{1/\gamma} = \frac{1}{1 + (i\omega\tau_{HN})^{\alpha}} \tag{5.1}$$

where for simplicity we ignore the effects of the small χ_∞. Using complex algebra identities, we can write the LHS of Equation (5.1) as

$$G(\gamma, \chi, \chi_0) = \frac{1}{\chi_0^{1/\gamma}} \left((\chi')^2 + (\chi'')^2\right)^{1/2\gamma} \left[\cos\left(\frac{1}{\gamma} \arctan\frac{\chi''}{\chi'}\right) - i \sin\left(\frac{1}{\gamma} \arctan\frac{\chi''}{\chi'}\right)\right] \tag{5.2}$$

G is an effective scaled susceptibility, and its real and imaginary components give scaled forms of χ' and χ'':

$$\begin{aligned} \mathrm{Re}\left[G(\gamma, \chi_0, \chi)\right] &= \chi_0^{-1/\gamma} \left[(\chi')^2 + (\chi'')^2\right]^{1/2\gamma} \cos\left[\frac{1}{\gamma} \arctan\left(\frac{\chi''}{\chi'}\right)\right] \\ \mathrm{Im}\left[G(\gamma, \chi_0, \chi)\right] &= \chi_0^{-1/\gamma} \left[(\chi')^2 + (\chi'')^2\right]^{1/2\gamma} \sin\left[\frac{1}{\gamma} \arctan\left(\frac{\chi''}{\chi'}\right)\right] \end{aligned} \tag{5.3}$$

To find an appropriate scaled frequency variable, we start by evaluating the RHS of Equation (5.1):

$$H(\alpha, \omega\tau_{HN}) = \frac{1 + (\omega\tau_{HN})^{\alpha} \left(\cos\frac{\pi\alpha}{2} - i \sin\frac{\pi\alpha}{2}\right)}{1 + 2(\omega\tau_{HN})^{\alpha} \cos\frac{\pi\alpha}{2} + (\omega\tau_{HN})^{2\alpha}} \tag{5.4}$$

Since α is relatively stable at values ≈ 0.91 (Figure 5.4C), the values of $\pi\alpha/2$ do not vary much over our temperature range. We therefore define a variable $x \equiv (\omega\tau_{HN})^{\alpha}$ that should function well as a scaled frequency.

Figure 5.5 shows that the scaled variables G and x yield excellent data collapse when we use the parameter values in Figure 5.4. The separate isothermal curves of Figure 5.2 collapse onto a single Cole-Cole function with $\alpha = 0.91, \gamma = 1$. Susceptibility curves that differ by ~ two orders of magnitude in their characteristic timescales can now be described by two universal scaled variables, and we confidently conclude that our data support the existence of universal HN relaxation without monopole transport in DTO.

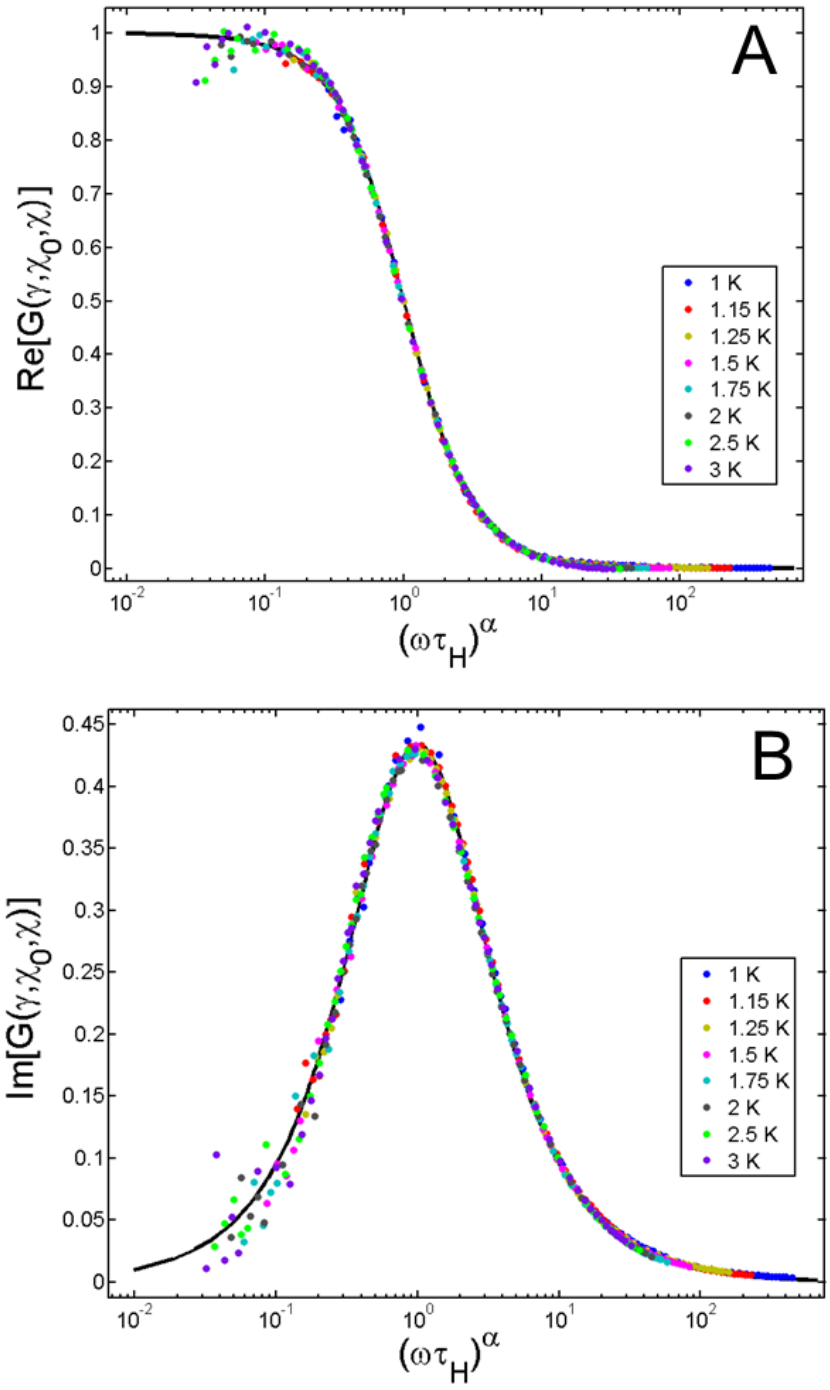

Figure 5.5: Plotting the scaled susceptibility $G(\gamma, \chi_0, \chi)$, which is defined in the main text, against the scaled frequency $(\omega\tau_{HN})^{\alpha}$ collapses our **(A)** real and **(B)** imaginary susceptibility data (colored symbols) onto a single function. The collapsed function (black lines) is a Cole-Cole function with $\alpha = 0.91$.

5.2 Results of DC measurements

HN frequency-domain relaxation and KWW time-domain relaxation are complementary descriptions of the same physical phenomena [14]. The strong evidence in support of HN relaxation in Section 5.1 therefore leads directly to the expectation of KWW relaxation in DTO time-domain responses. Figure 5.6A shows the observed DTO relaxation at times $t \geq 200$ ms after turning off a 25-mA current (recall that DTO signals dominate the EMF at these times; see Section 3.3.2), along with fits to the KWW stretched-exponential function given by

$$V(t) = V_0 \exp\left(-\left(\frac{t}{\tau_{KWW}}\right)^{\beta}\right) \tag{5.5}$$

where τ_{KWW} is a characteristic relaxation time and $\beta \leq 1$ is a "stretching exponent". The KWW fits are excellent parametrizations of the data; this is confirmed by the small residuals shown in Figure 5.6B.

The range over which we could achieve reliable DC fits was set by our voltage and time resolution. At low temperatures, the magnetization relaxation becomes so slow that the signal from $d\mathbf{M}/dt$ becomes difficult to resolve above our noise without large amounts of averaging. Long low-temperature relaxation times also mean that measurements must be taken for ~ several minutes or more after current changes; measurements of this length can be affected significantly by drift noise (Section 3.3.2). We were able to readily resolve signals down to ~ 575 mK with the high precision needed for reliable fits. The averaging necessary to bring this lower temperature bound down to ~ 525-550 mK is probably achievable within our storage dewar's liquid helium hold time. At 500 mK, however, the times required to resolve full signal decays become long enough that drift noise diminishes the quality of our fits.

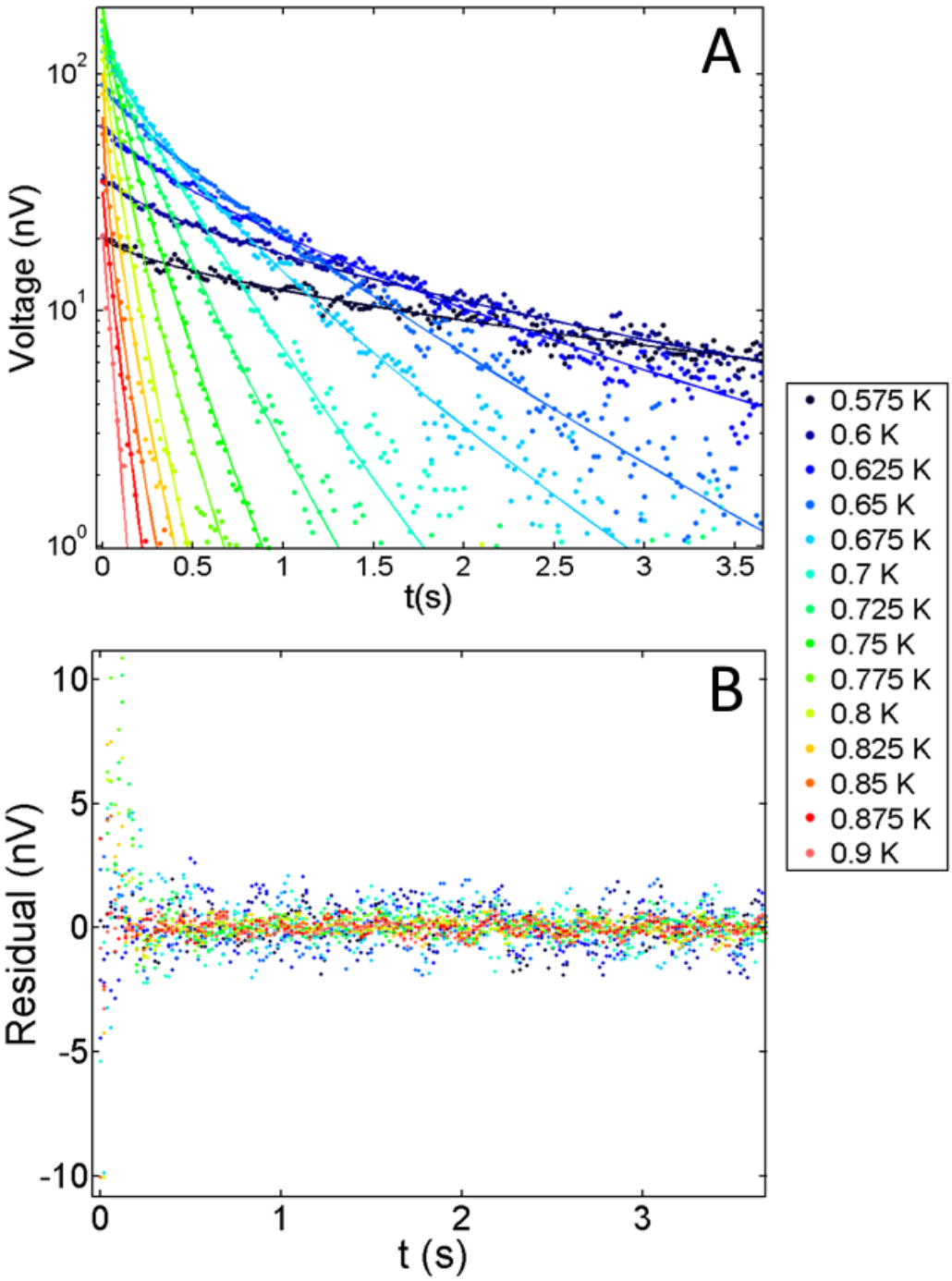

Figure 5.6: **(A)** Observed DTO relaxation (symbols) after turning off currents of 25 mA. KWW fits (lines) provide an excellent description of the data over our entire temperature range; this is confirmed by the small fitting residuals in **(B)**. The residuals are a few percent or less of the signal size throughout the measured time range.

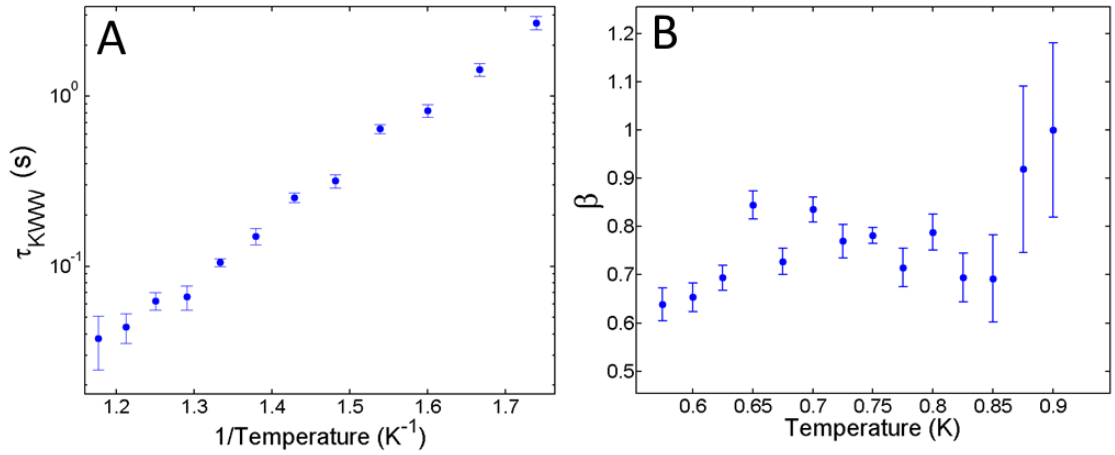

Figure 5.7: Temperature dependence of **(A)** the characteristic relaxation time τ_{KWW} and **(B)** the KWW stretching exponent β. β increases weakly at low temperatures, but stabilizes at ~ 0.8 above 700 mK. $\beta < 1$ at the temperatures where we know it with good precision, indicating that DTO can not be described by a single microscopic relaxation time.

These observations reflect the rapid divergence of the relaxation time (Figure 5.7A) below 1 K. A relatively modest temperature change from 750 mK to 600 mK increases τ_{KWW} by more than an order of magnitude, and this trend becomes even more severe at lower temperatures. At high temperatures we encounter the opposite problem: DTO relaxation becomes so fast that we are only able to take a few nanovoltmeter readings (which have a hard lower bound on their time resolution) before the signal decays below our noise level. At temperatures above 900 mK we lose the ability to distinguish between simple Debye and more complex KWW behavior; this fixes the upper bound of our fitting range.

In Section 1.2 we noted that $\beta = 1$ corresponds to Debye relaxation appropriate for a single microscopic relaxation time, while more complex dynamics lead to $\beta < 1$. The observed values of $\beta(T)$ (Figure 5.7B) indicate that DTO falls into the latter category; $\beta < 1$ at the temperatures where we know it with good precision. This is consistent with our frequency-domain measurements,

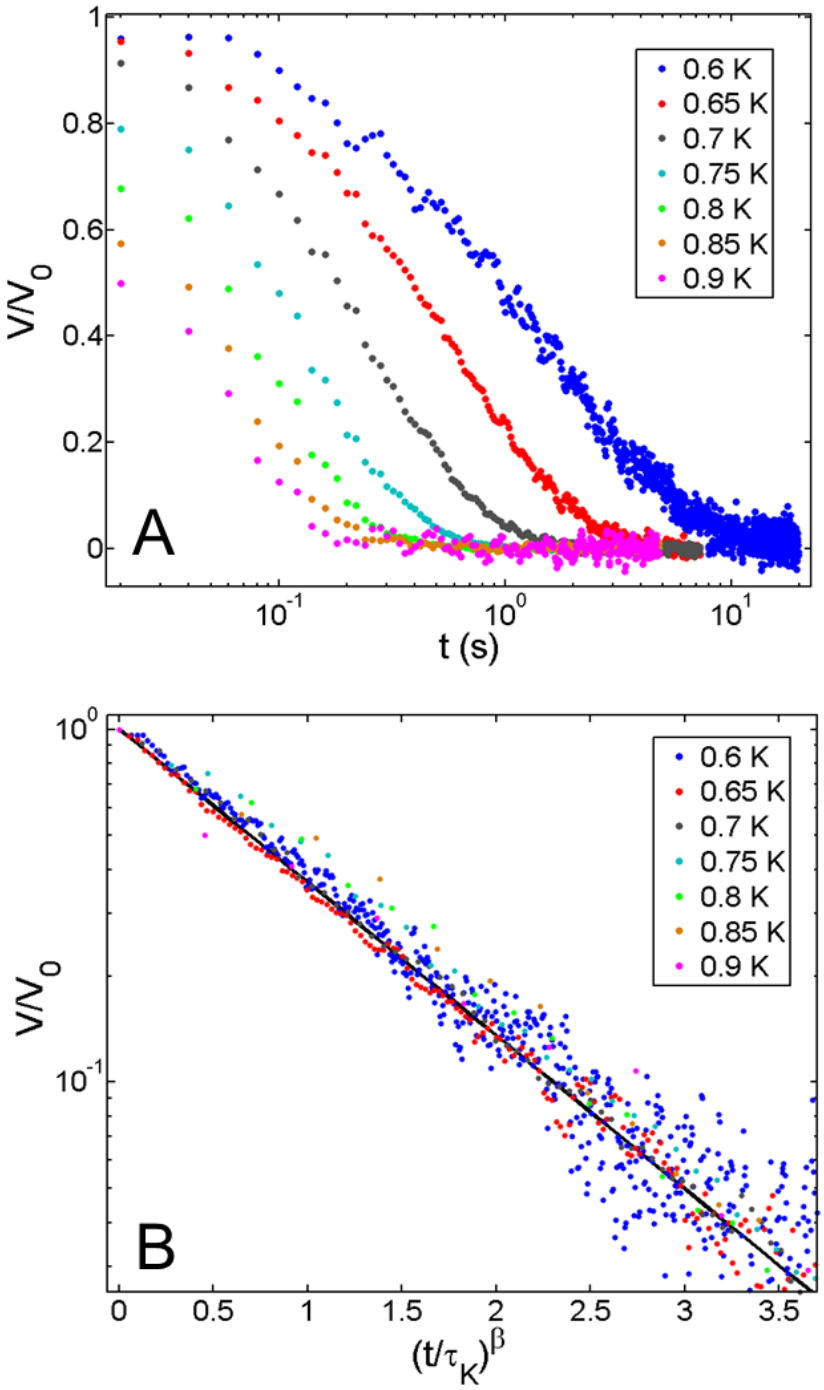

Figure 5.8: **(A)** DTO relaxation at temperatures between 600 mK and 900 mK. The curves have characteristic timescales spanning ~ two orders of magnitude in time. **(B)** These disparate data collapse onto a simple exponential function (black line) when we use scaled KWW variables.

where we found that the HN exponents α and γ were both less than 1. Our DC and AC measurements both show that the simplest relaxation models are inadequate descriptions of DTO dynamics; we must consider full generalized relaxation functions to achieve good descriptions of the data over a wide range of temperatures, times, and frequencies.

We can demonstrate the quality of the KWW description of DTO by using scaled time and voltage variables to collapse the isothermal responses onto a single function. In the case of KWW relaxation the arithmetic is simple; with a scaled voltage $v \equiv V/V_0$ and a scaled time $x \equiv (t/\tau_{KWW})^{\beta}$ we expect that the data will collapse onto a simple exponential function $v = \exp(-x)$. Figure 5.8 shows that this is the case for DTO dynamics; relaxation curves with timescales separated by orders of magnitude in time collapse onto the same simple exponential function when we use the parameter values in Figure 5.7. This shows that the stretched-exponential function is an excellent parametrization of time-domain DTO dynamics.

Stretched-exponential relaxation has been previously observed in single-crystal rods of DTO [63]. This type of relaxation is at odds with DSIM and monopole simulations, which predict behavior close to Debye relaxation and explicitly rule out stretched-exponential relaxation [50]. The authors in [63] attributed their observations to the presence of open boundary conditions in their sample; these conditions give simulation results that differ from the findings of the studies in periodic boundary conditions in [50]. However, our sample topology is a physical realization of periodic boundary conditions, so we conclude that KWW relaxation in DTO is robust even in a closed topology. Therefore, our DC experiments, like the AC experiments in Section 5.1, directly contradict the

predictions of the DSIM and monopole fluid theory.

5.3 A Unified Description of the measurements

The rapidly-diverging relaxation times in our experiment and ultraslow relaxation in previous investigations of DTO (Chapter 2) indicate that it may be approaching a glass transition. We have also shown that DTO exhibits KWW and HN relaxation in response to applied fields. These relaxation forms are found in most supercooled liquids (Section 1.2), which have relaxation times whose temperature dependence is given by the VTF function:

$$\tau(T) = \tau_0 \exp\left(\frac{DT_0}{T - T_0}\right) \tag{5.6}$$

To see if this also applies to DTO, we need to combine our measurements from our two different measurement techniques. In Section 1.2 we noted that the KWW and HN relaxation times are linked by the following relation [14]:

$$\ln\left(\frac{\tau_{HN}}{\tau_{KWW}}\right) = 2.6(1-\beta)^{1/2}\exp(-3\beta) \tag{5.7}$$

If our two types of experiments really do measure the same dynamics, we should be able to convert τ_{KWW} to τ_{HN} and find a single smoothly-varying curve after combining our AC and DC relaxation times. Figure 5.9A shows that we do indeed find such a curve for our combined measurements; AC and DC measurements give the same relaxation times between 800 and 850 mK, and we can describe both experiments with a single smooth curve $\tau_{HN}(T)$ between 575 mK and 3 K. Our two experimental techniques are complementary probes of the same DTO dynamics.

It is also clear from Figure 5.9A that DTO relaxation times have a decidedly

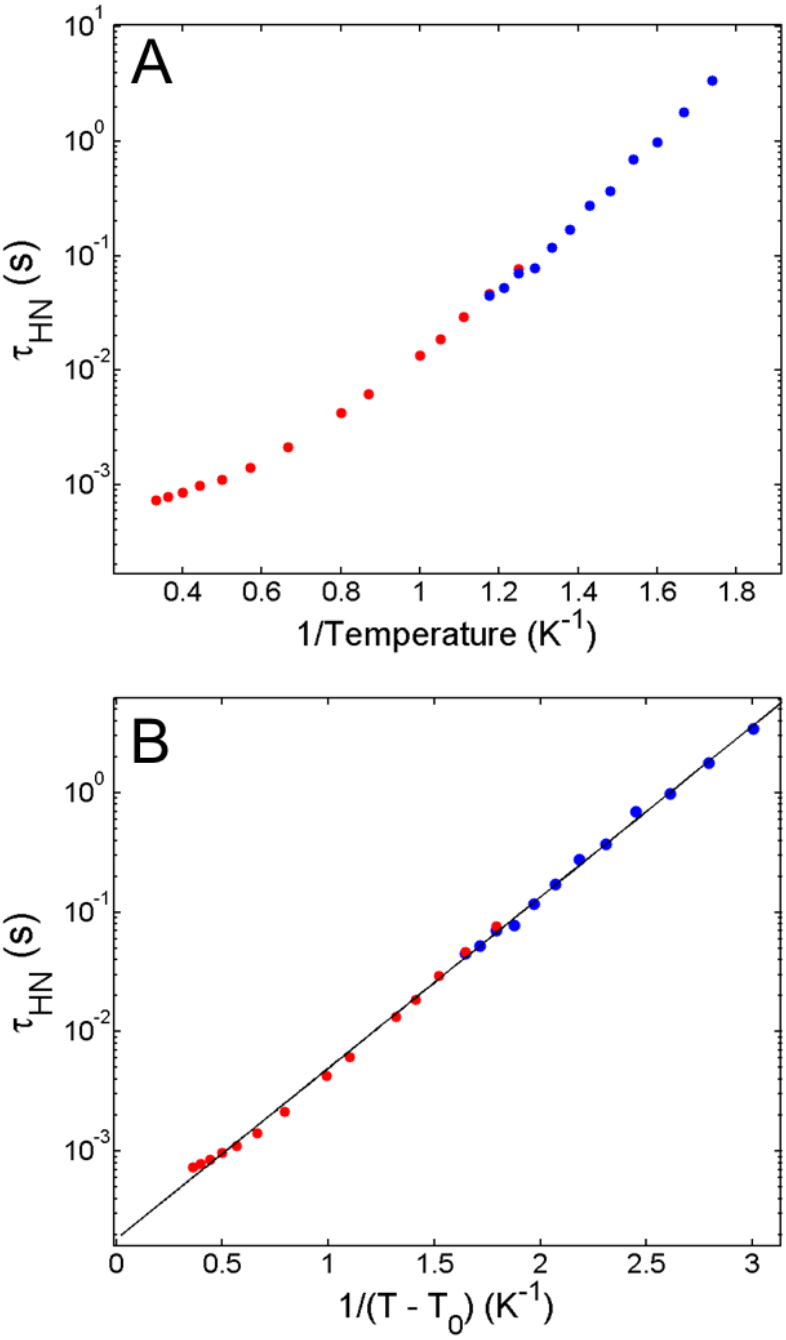

Figure 5.9: (A) Temperature dependence of τ_{HN} found from direct HN fits to AC data (red) and calculated from DC fitting parameters with Equation (5.7) (blue). AC and DC measurements give the same τ_{HN} at 800 and 850 mK, and the combined curve varies smoothly with temperature. $\tau_{HN}(T)$ clearly shows super-Arrhenius temperature variation. **(B)** $\tau_{HN}(T)$ (symbols) is fit well by a VTF parametrization (black line) with $T_0 = 242$ mK. The fit is excellent over more than three orders of magnitude in the relaxation time.

non-Arrhenius temperature dependence. An Arrhenius form $\tau_0 \exp(\Delta/k_B T)$ is a straight line on a log-linear plot of τ versus $1/T$; this clearly does not describe our data. Our results are instead parametrized very well by the VTF form in Equation (5.6). Figure 5.9B shows that a VTF fit is an excellent parametrization of the observed DTO relaxation time as it varies over more than three orders of magnitude. The line in this plot is generated using the best-fit parameter values $\tau_0 = (186 \pm 34)\,\mu$s, $D = 13.6 \pm 1$, and $T_0 = (242 \pm 23)$ mK. DTO dynamics are therefore completely analogous to the dynamics of standard supercooled liquids; both systems have KWW relaxation and HN relaxation, and their relaxation times have a VTF temperature dependence.

CHAPTER 6

CONCLUSIONS AND FUTURE DIRECTIONS

6.1 A Supercooled Magnetic Liquid in $Dy_2Ti_2O_7$

In Section 1.2 we described several phenomena common to supercooled liquids (Figure 1.2): a broad peak in the heat capacity below an ordering temperature, VTF relaxation times, HN relaxation, and KWW relaxation. Many groups have previously observed a broad peak in the specific heat of DTO at $T \sim 1.1$ K [40][41][42][43][44], which is slightly below the ordering temperature $T_{cw} \approx 1.2$ K that is predicted from high-T susceptibility measurements [36]. In Section 5.1 we found abundant evidence for HN relaxation in DTO, and in Section 5.2 we showed that DTO exhibits KWW relaxation in the time domain. Finally, we found that our entire set of AC and DC relaxation times is described well by a VTF temperature dependence. Taking everything together, we conclude that the low-temperature dynamics of DTO are representative of a *magnetic* supercooled liquid state directly analogous to the well-established dielectric glass-forming liquids. The data are completely inconsistent with the predictions of the theory of mobile Coulombic monopoles, indicating that the Dipolar Spin Ice model is an incomplete microscopic description of DTO physics. Our AC and DC data are very similar to what has been observed in previous AC susceptibility (Figure 2.10) and DC relaxation (Figure 2.11) experiments, so our analysis and conclusions likely apply to all previous studies of DTO dynamics.

Our VTF fit predicts that under arbitrary cooling protocols DTO must enter either an ordered state via a first-order transition or a glass state via a dynamical transition at temperatures $T \geq T_0 = 242$ mK. This is consistent with both short-

time and long-time thermal measurements at temperatures below 1.1 K, where C/T falls off steeply from its peak value. Measurements that waited for shorter times at low temperatures (favoring observation of a glass state) found that the heat capacity begins to flatten out from its steep decrease at temperatures ~ 400-500 mK [40][41][42][43], indicating that glass transition temperatures could typically fall near 400 mK. Measurements that waited for long times at low temperatures (favoring an ordering transition if such a transition exists) observed the beginning of what could be a sharp peak in C/T centered at temperatures at least as low as 340 mK [44]. All these observations are consistent with our postulated lower limit for the temperature range of a DTO liquid state.

The fragility parameter of our VTF fit is $D = 13.6$. Values of D near 10 describe materials that show significant departures from standard thermally-activated Arrhenius behavior; these are known as "fragile liquids" in the standard liquid terminology [2]. DTO therefore hosts a fragile magnetic liquid whose departure from Arrhenius behavior is comparable to commonly-studied glass-forming liquids such as glycerol and propylene glycol [2][4]. However, unlike these liquids the DTO state exists in an environment with little geometric disorder; the spins have highly-constrained directions and are positioned on an ordered lattice. This becomes especially clear when comparing DTO to the spin glasses (Section 1.3), which are the archetypal magnetic systems governed by positional and structural disorder. The frequency-domain spread of our measured AC relaxation (Figure 5.2) is much narrower than what is typically observed in spin glasses, indicating that DTO microscopic relaxation times are spread over a much smaller range. Furthermore, the gentle peak of $\chi'(T)$ (Figure 2.9) contrasts with sharp spin-glass cusps, and the weak field dependence of the magnetization freezing temperature is unlike anything seen in the

spin glasses [37].

We are therefore left to conclude that the supercooled liquid state in DTO likely derives not from structural disorder, but from some other mechanism that is robust even in an ordered environment. Analytical theories of glassy behavior in spins on an ordered lattice are still in a developmental stage (Section 1.4), and there is still debate about whether Many-Body-Localization (MBL) allows such behavior for general realistic systems. However, numerical simulations of disorder-free frustrated systems on hexagonal [30] and kagome [31] lattices have yielded some signatures of glass-forming liquids, including VTF relaxation time behavior and stretched-exponential relaxation. The work in [31] in particular seems very promising as a path to a model of DTO dynamics, since it directly applies the attractive theoretical ideas of hierarchical dynamics [32] to a geometry that is a component of the pyrochlore lattice. Performing similar numerical studies on Ising spins in a pyrochlore lattice may lead to accurate modeling of DTO; this would be equivalent to using the hierarchical relaxation time rules from [31] for the simulations in [35] and [52] that utilize single spin flips and spin loop circulation algorithms.

Simple phenomenological models of non-interacting hexagonal spin loops capture most of the features of DTO neutron scattering (Figure 2.12), so it is very possible that DTO dynamics can be modeled using spin clusters that interact via some effective potential. This would represent a return to a more dipole-based picture of DTO; this is an attractive strategy given the failure of monopole models. A spin cluster model would simplify our picture of DTO and perhaps allow it to be investigated with the analytical MBL theory. DTO therefore has the potential to unify deep theoretical ideas spanning several decades and greatly

advance our understanding of the still-mysterious glass transition.

6.2 Future Directions

There are several measurements that could further elucidate the dynamics of DTO and other related materials. The observed differences between spin glasses and DTO are a strong indication that DTO dynamics are not driven by structural disorder, but it would be very useful to subject this deduction to further tests. In our case, we could try to anneal the samples and then repeat the measurements reported in this work; comparing measurements before and after the annealing would reveal specifically the quantitative contribution of lattice defects to our results. Magnetic dilution via substitution of non-magnetic elements (in the spirit of Y-substitution in [58]) would also provide an interesting test, since this would presumably increase disorder as well as decrease the average magnetic interactions between Dy^{3+} ions.

Even more knowledge could be gained from detailed studies of DTO relaxation in the vicinity of our predicted VTF transition temperature $T_0 = 242$ mK. Long-time thermal measurements below 340 mK (the lowest temperature probed in [44]) would reveal the full nature of the sharp heat capacity increase that begins at ~ 400 mK; this could pinpoint any temperature where DTO enters into its predicted ordered state. Magnetization measurements in this temperature range would map out characteristic microscopic relaxation times and reveal the temperature dependence of VTF, KWW, and HN parameters during the approach to T_0. These complementary measurements would provide more detailed data against which theoretical models could be tested. At these tem-

peratures the relaxation time of DTO becomes ~ days, so such measurements would require great experimental stability and phenomenal patience; however, in principle they can be done.

Experiments on other pyrochlore materials would also provide important insights. Along with DTO, $Ho_2Ti_2O_7$ (HTO) is often cited as a canonical spin ice compound. Ho^{3+} ions have an angular momentum ($J = 8$) similar to that of Dy^{3+}, and an anisotropic crystal field breaks the angular-momentum-state degeneracy and enforces the ground state pair $|8, \pm 8\rangle$ [39]. Despite a ferromagnetic Curie-Weiss temperature $T_{cw} \approx 2$ K, HTO shows no evidence of magnetic ordering down to 50 mK in neutron scattering [81] or μSR measurements [82]. Furthermore, low-temperature neutron scattering measurements have revealed the pinch-point structure (Figure 2.5) characteristic of a $\nabla \cdot \mathbf{M} = 0$ phase [83]. HTO thus seems to be a clear example of a spin ice. However, heat capacity measurements on HTO reveal a large low-temperature Schottky-like peak not present in DTO; this is likely due to an enhanced hyperfine structure in the Ho^{3+} nuclear moments [84]. Subtraction of this nuclear contribution yields an electronic heat capacity with a broad peak just below 2 K [84]. This heat capacity looks very similar to what has been observed in DTO, and integration of the data yields a residual entropy close to the Pauling ice value [85]. It will be very useful to apply our techniques to HTO; it is similar in most respects to DTO, but its strong hyperfine interactions introduce an interesting new wrinkle into the problem.

DTO and HTO are considered to be relatively classical Ising systems because their magnetic ions have large Ising angular momenta with negligible superexchange couplings and very weak transverse exchange couplings [86]. There is considerable theoretical interest in other magnetic systems where quantum dy-

namics may be more significant. Exotic quantum liquids have been predicted for frustrated magnetic materials where quantum fluctuations become important [87][88]; such states could conceivably occur in materials where the magnetic ions have small angular momenta (i.e. comparable to $\hbar$) and significant transverse exchange couplings. These conditions could yield magnetic configuration degeneracies with zero-point spin fluctuations even in the $T \rightarrow 0$ limit; such behavior would present a stark contrast to the strong T-dependence of the relaxation time in DTO. Many types of exotic quasiparticle and gauge-field descriptions of these quantum states have been proposed, and searches for them are ongoing in pyrochlores and other materials [88]. Our boundary-free measurement technique will be useful for the study of these liquid states, and the analysis strategy of Chapter 4 will test any transport models that derive from exotic theories of frustrated magnetic dynamics.

APPENDIX A

MACHINE DRAWINGS

This appendix contains drawings for the $Dy_2Ti_2O_7$ experiment, mixing chamber experimental insert, and high-current wire feedthrough assemblies. The DTO experiment drawings (Figures A.1 - A.7) are fairly specialized, but they will likely prove useful for future applications of our techniques to other frustrated magnetic materials. The mixing chamber insert (Figures A.8 - A.10) is simple and imposes few constraints on experiments, which are mounted on general-purpose hexagonal plates that mate with the insert. Sample mounting plates were machined from brass, and all other components of the DTO experiment and insert were machined from copper and then electroplated with gold.

To construct our cryogenic hermetic feedthrough (Figures A.11 - A.16), we machined a cap from Stycast 1266 and glued it to a stainless steel piece with additional Stycast 1266. This stainless steel piece mates with a 4K flange on top of our vacuum can. A macor shell protects the feedthrough assembly. Large-diameter superconducting wires connect to thinner wires at various solder points (Figure A.11); these thinner wires then travel into the vacuum can and interface with the experiment. There seem to be few commercially-available cryogenic hermetic feedthroughs, so our design will likely be very useful for future probes with high-current applications.

We also include drawings for the room-temperature feedthroughs (Figures A.17 - A.20) that we installed for our high-current circuitry. In the completed room-temperature assembly (comprised entirely of stainless steel parts), copper wires travel from hermetic feedthroughs to a rigid vertical tube via flexible bellows hoses. This tube connects to the dewar space via KF-16 flanges.

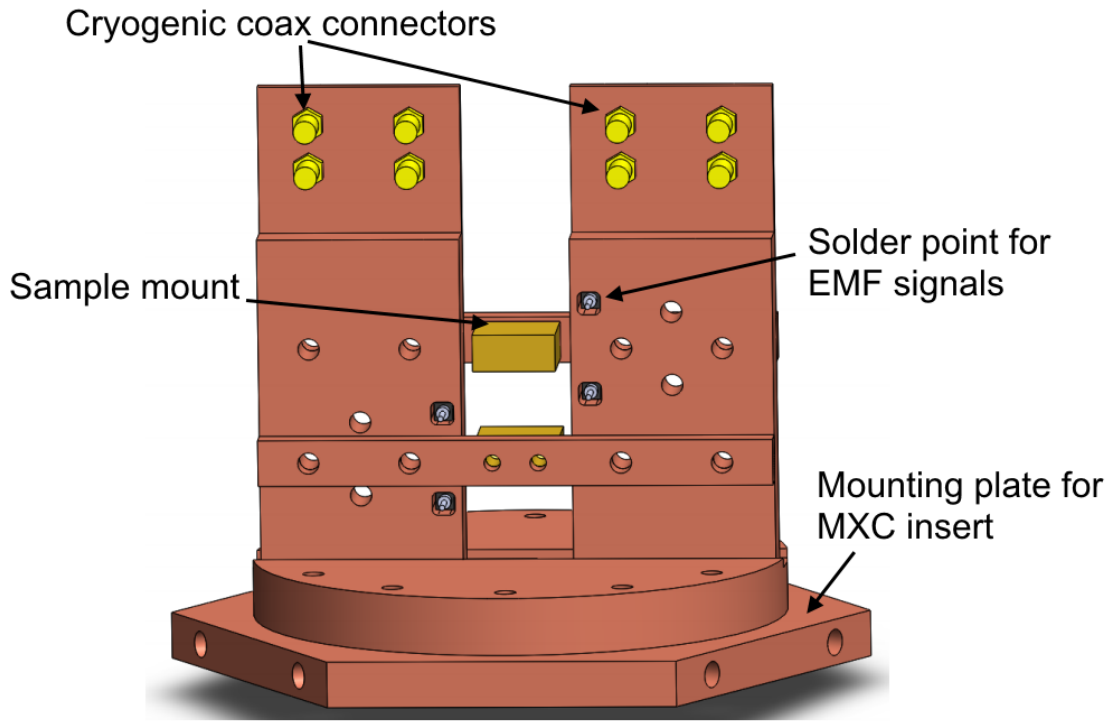

Figure A.1: The assembly used for our DTO experiments. Each assembly can hold two samples, which are mounted on brass plates with Lakeshore varnish. EMF measurement wires contact the STS wire leads at soldering pins; the STS wires ultimately terminate at niobium screw pads. Each assembly is mounted on a hexagonal plate that is fixed to the mixing chamber insert.

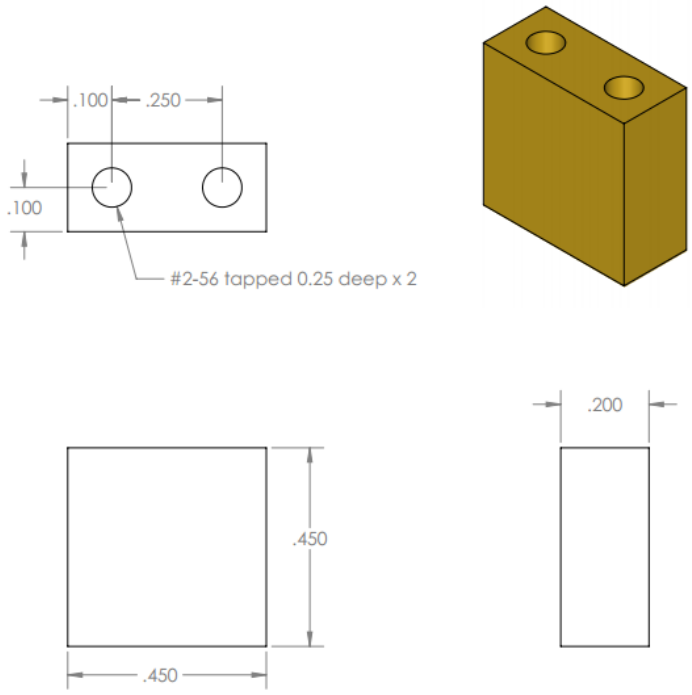

Figure A.2: Mounting plate for the samples.

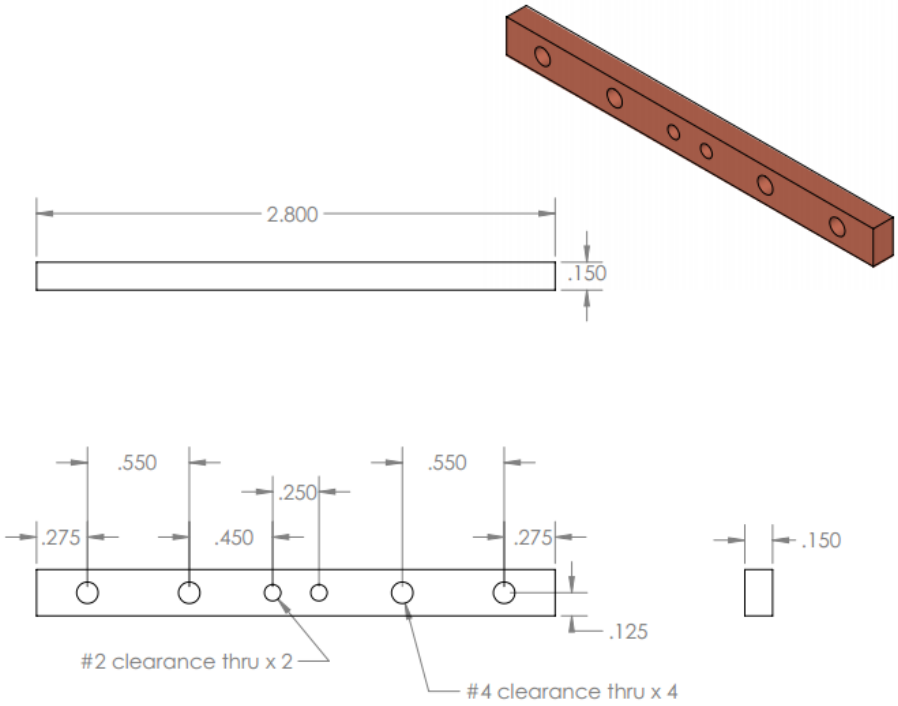

Figure A.3: Support rod for mounting the samples on the assembly.

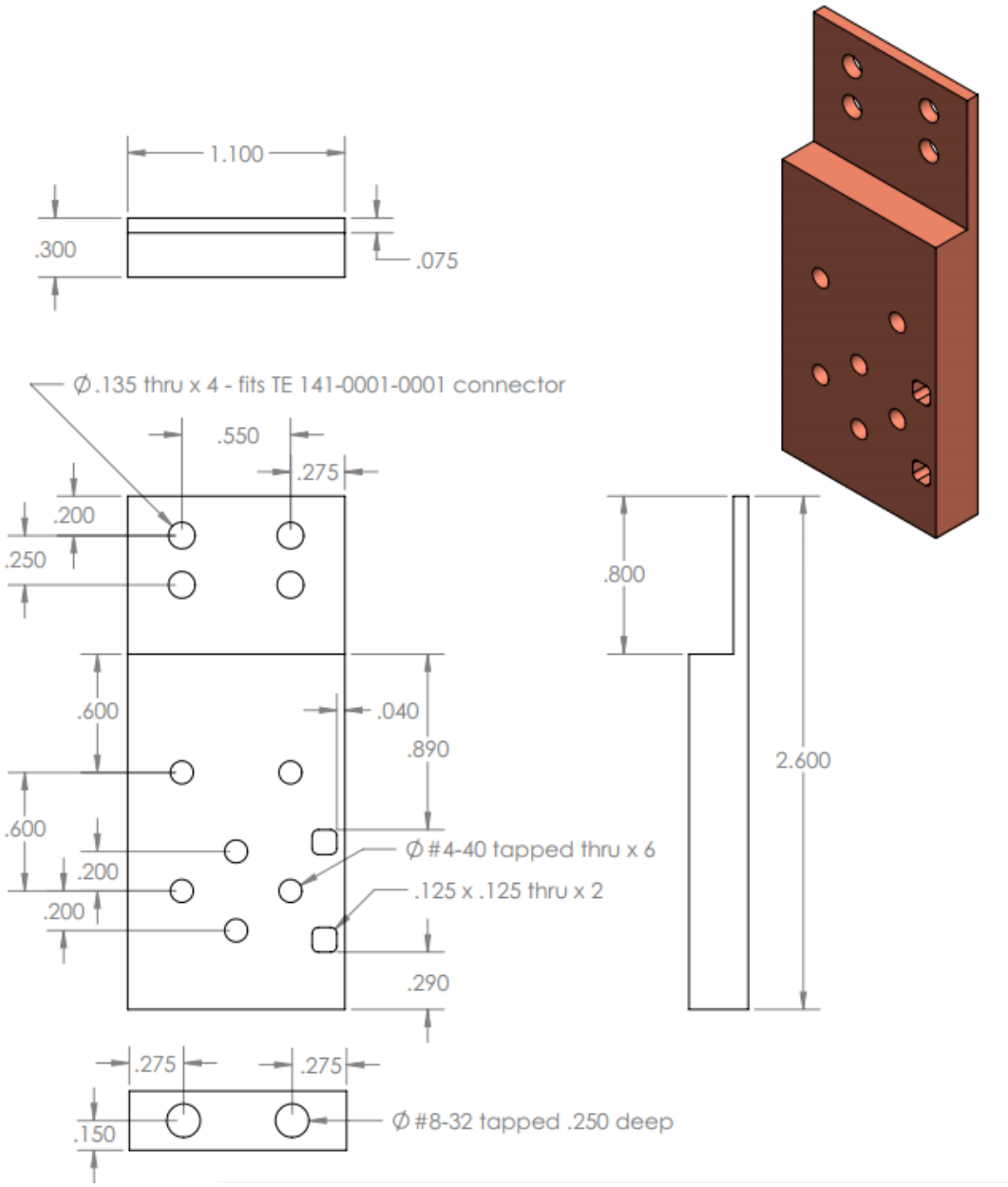

Figure A.4: Vertical piece that fixes coaxial feedthroughs, soldering pins, and the sample positions.

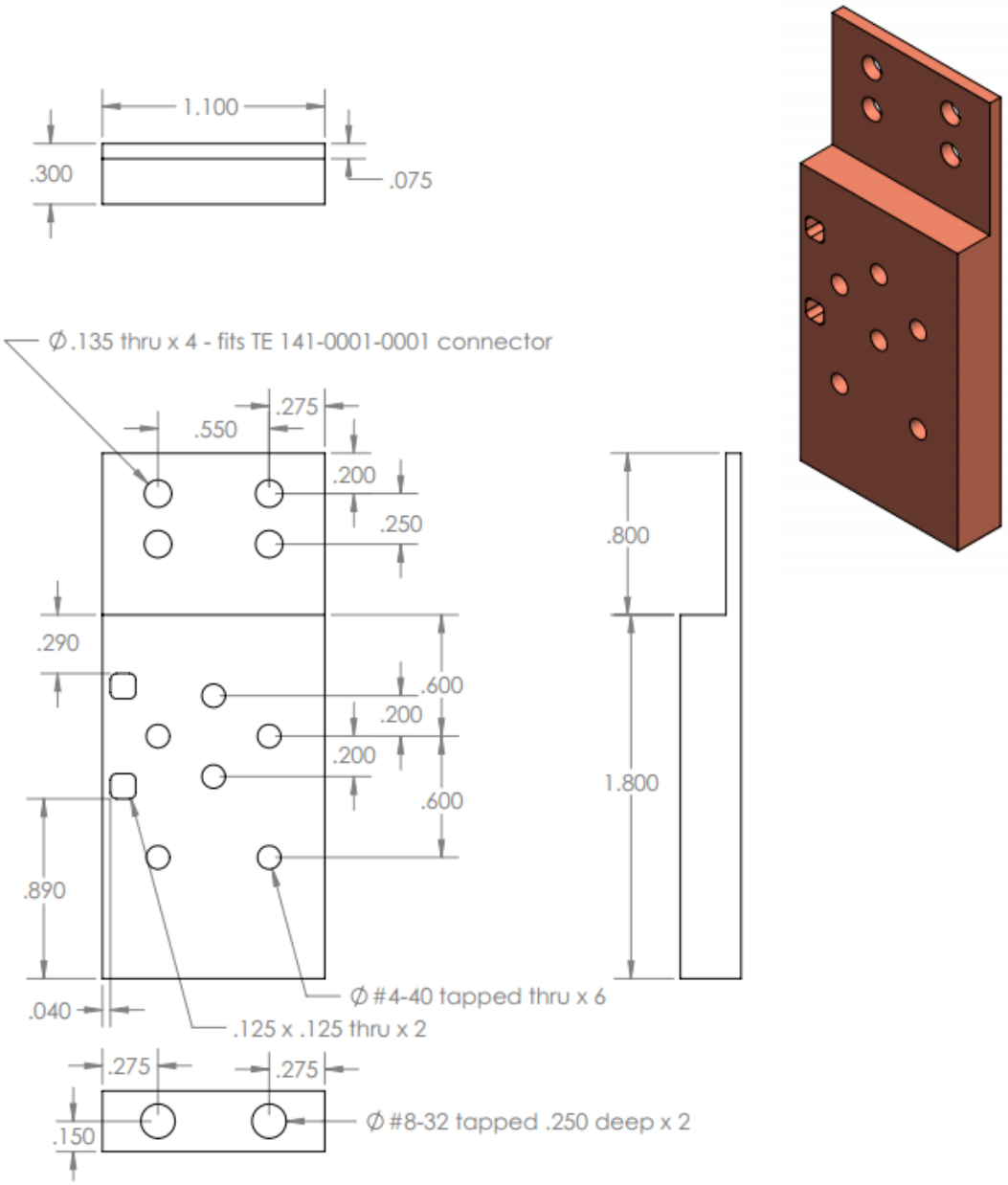

Figure A.5: Companion vertical piece that fixes coaxial feedthroughs, soldering pins, and the sample positions.

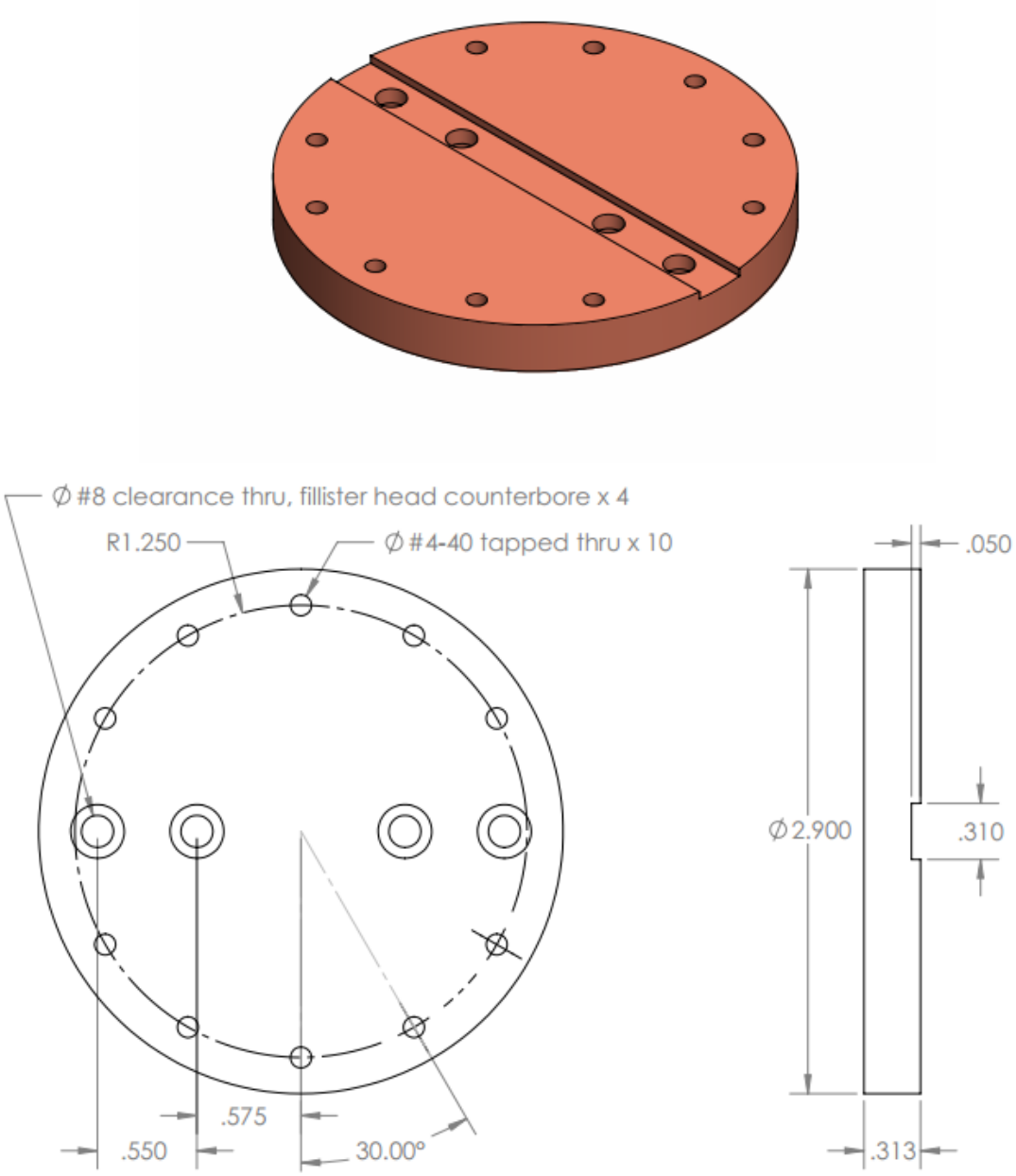

Figure A.6: Base piece of the DTO experiment assembly.

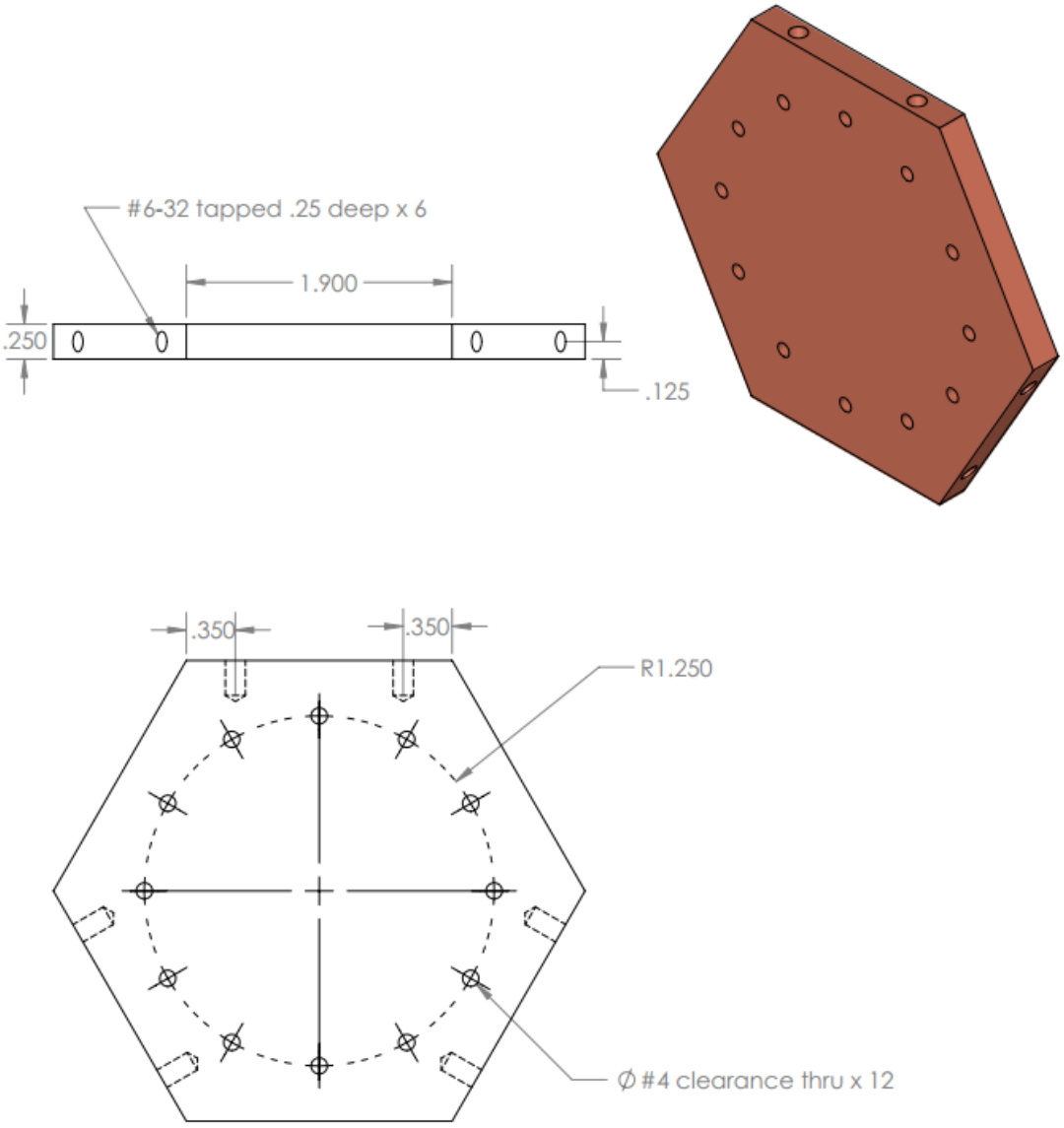

Figure A.7: Experimental mounting stage for the mixing chamber insert.

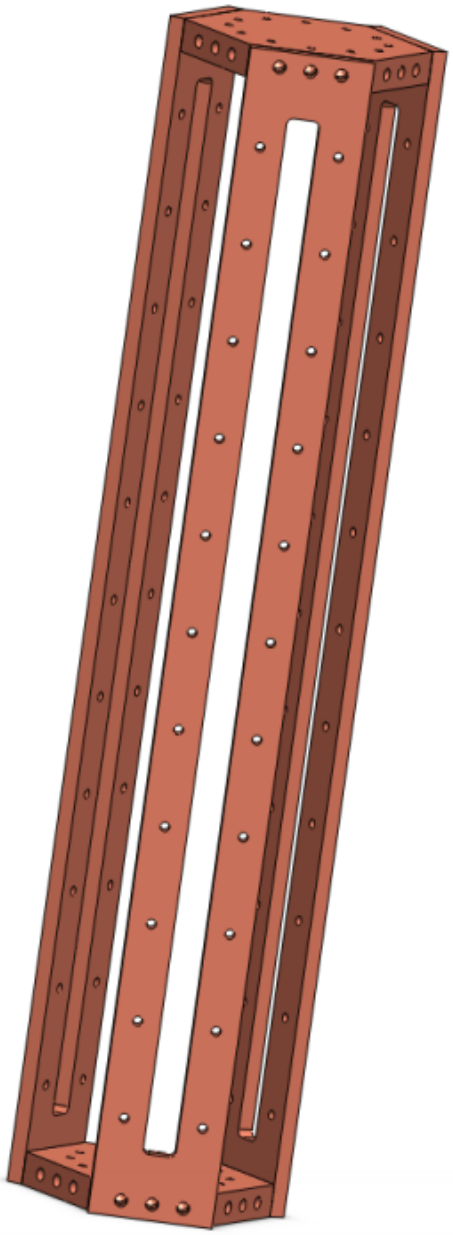

Figure A.8: Insert for general experiments on the Davis group dilution refrigerator. This insert attaches to the bottom of the mixing chamber plate.

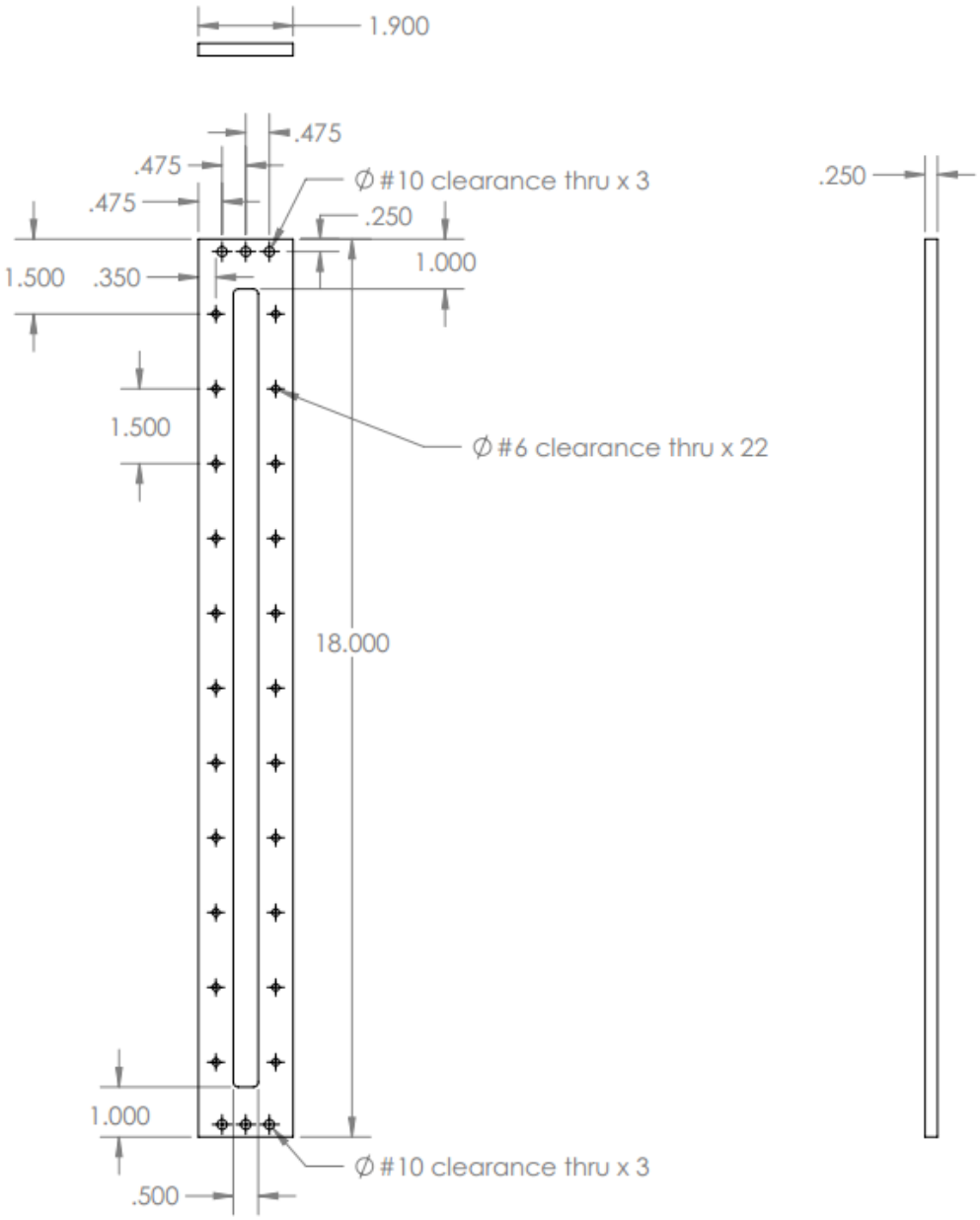

Figure A.9: Machine drawings for the vertical side pieces of the mixing chamber insert.

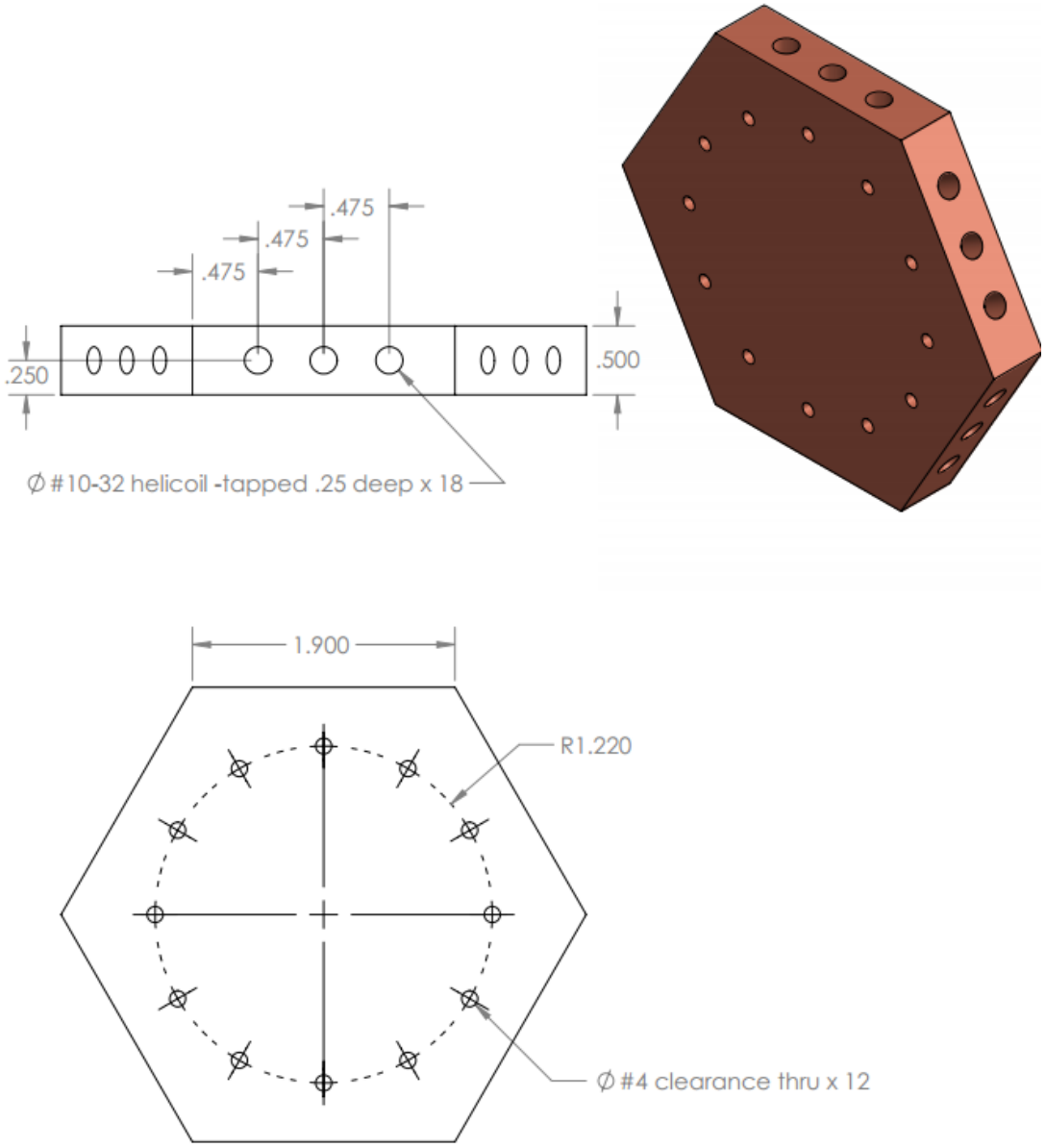

Figure A.10: Top and bottom pieces of the mixing chamber insert.

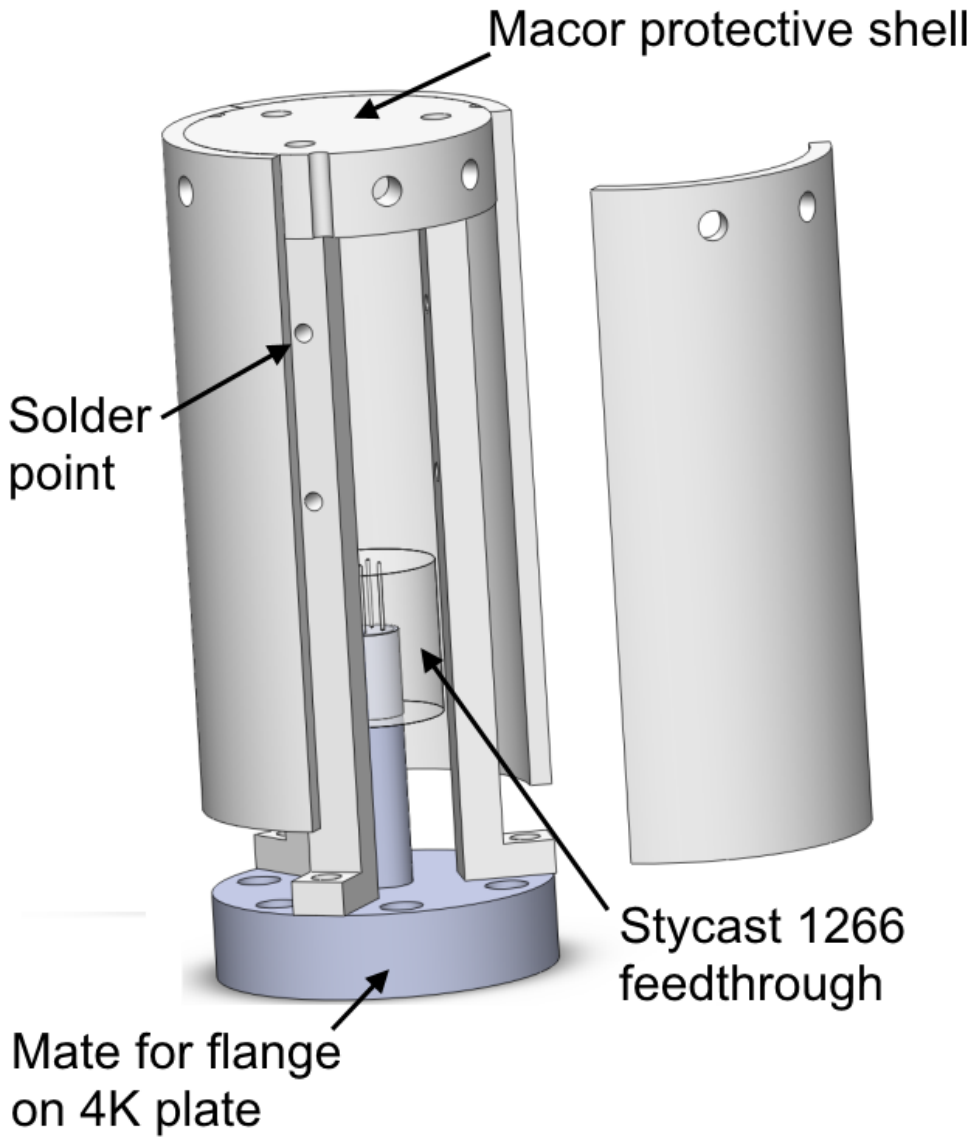

Figure A.11: Complete assembly for our cryogenic hermetic wire feedthrough.

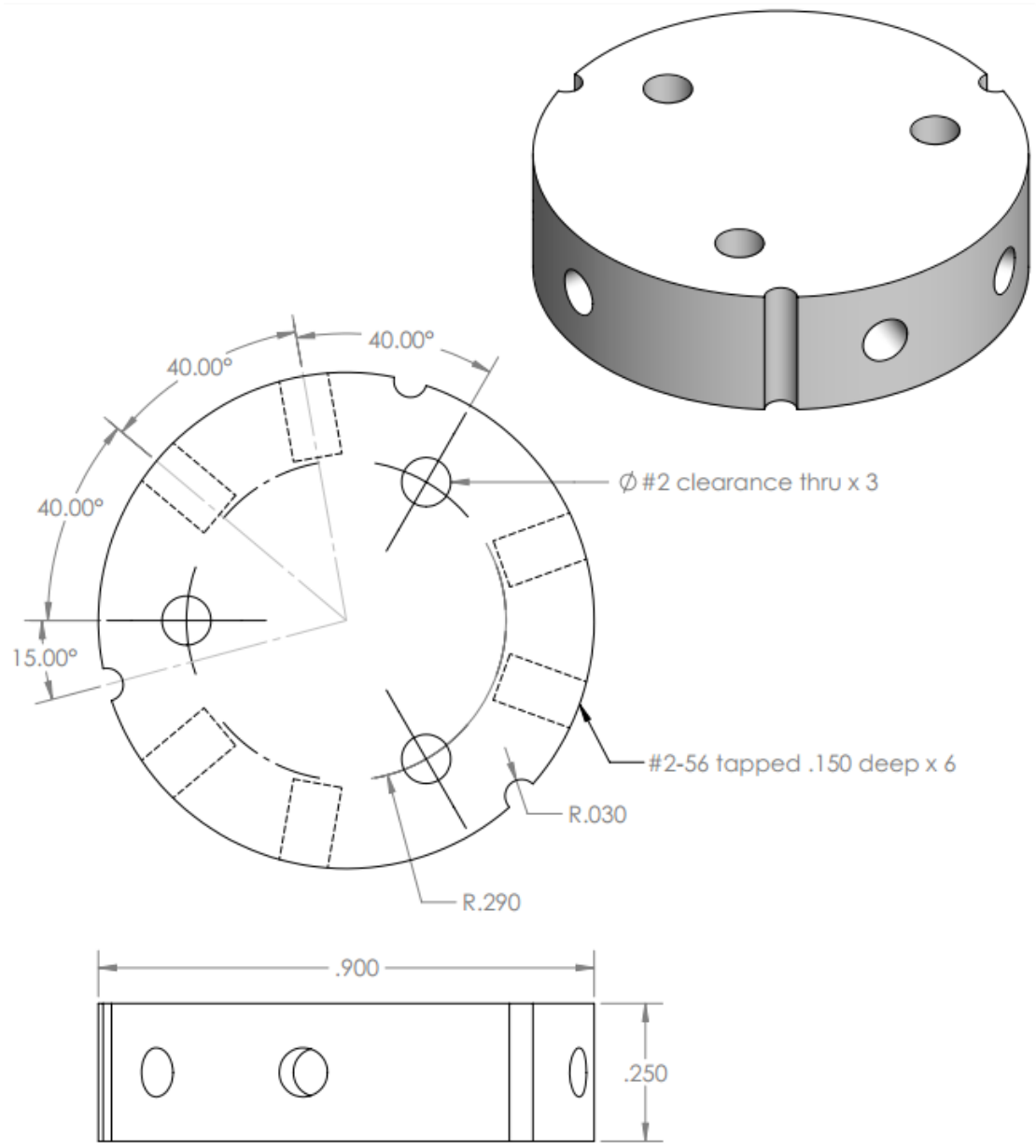

Figure A.12: Top piece of the protective macor shell for our cryogenic feedthrough.

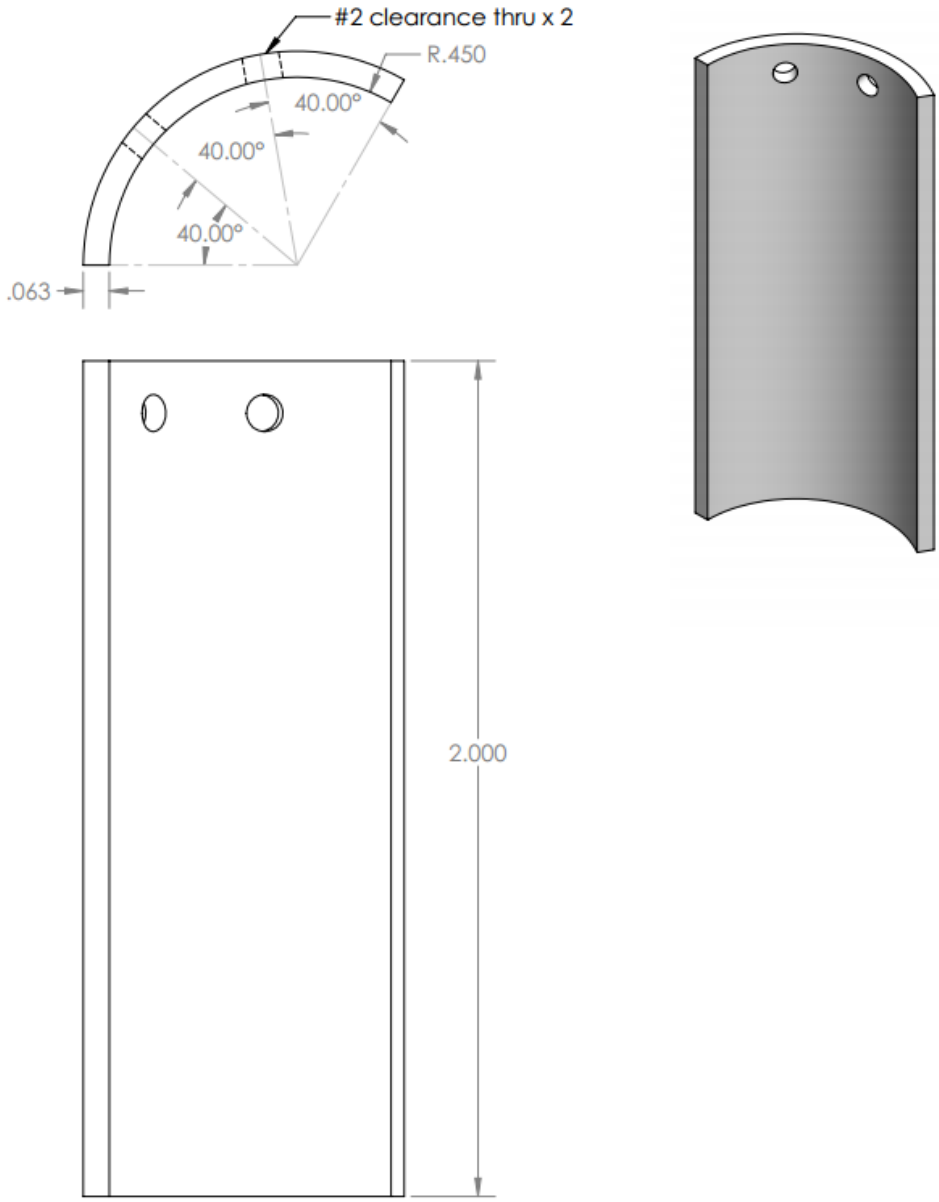

Figure A.13: Side pieces of the protective macor shell for our cryogenic feedthrough. Three of these pieces are needed for a complete shell.

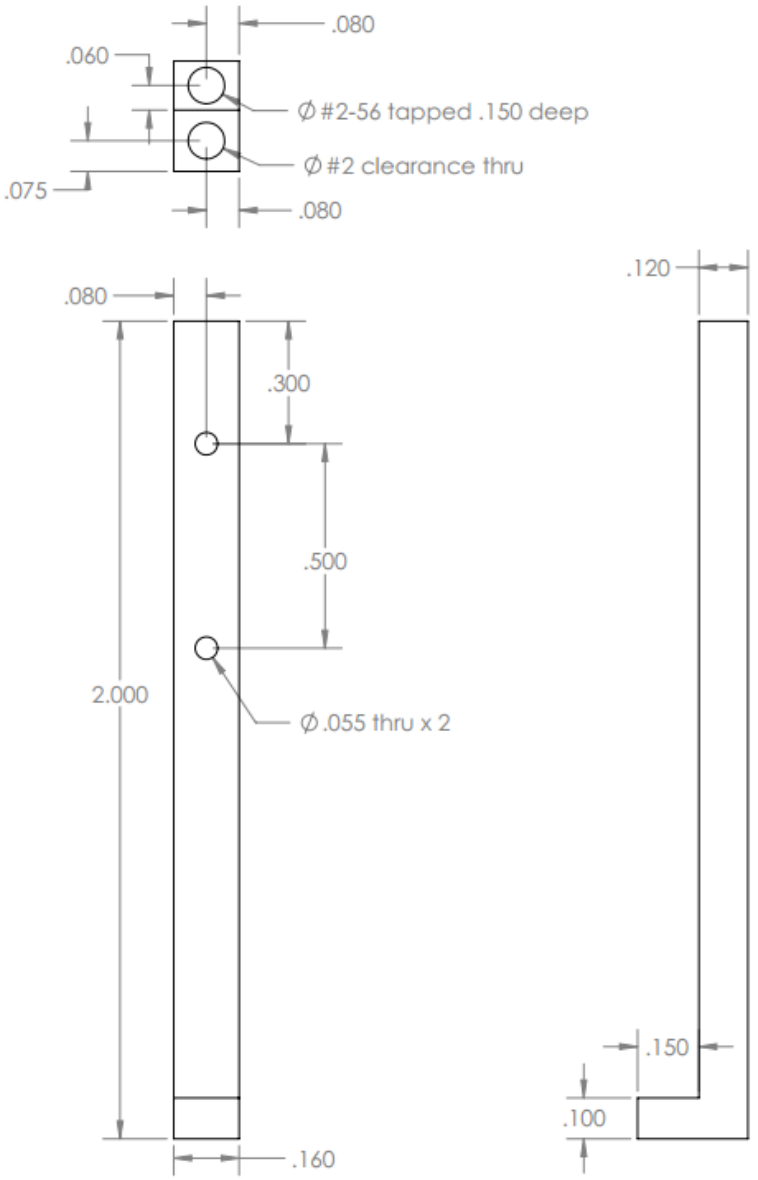

Figure A.14: Drawing of the vertical macor stands for our cryogenic feedthrough. Three of these pieces are needed for a complete assembly.

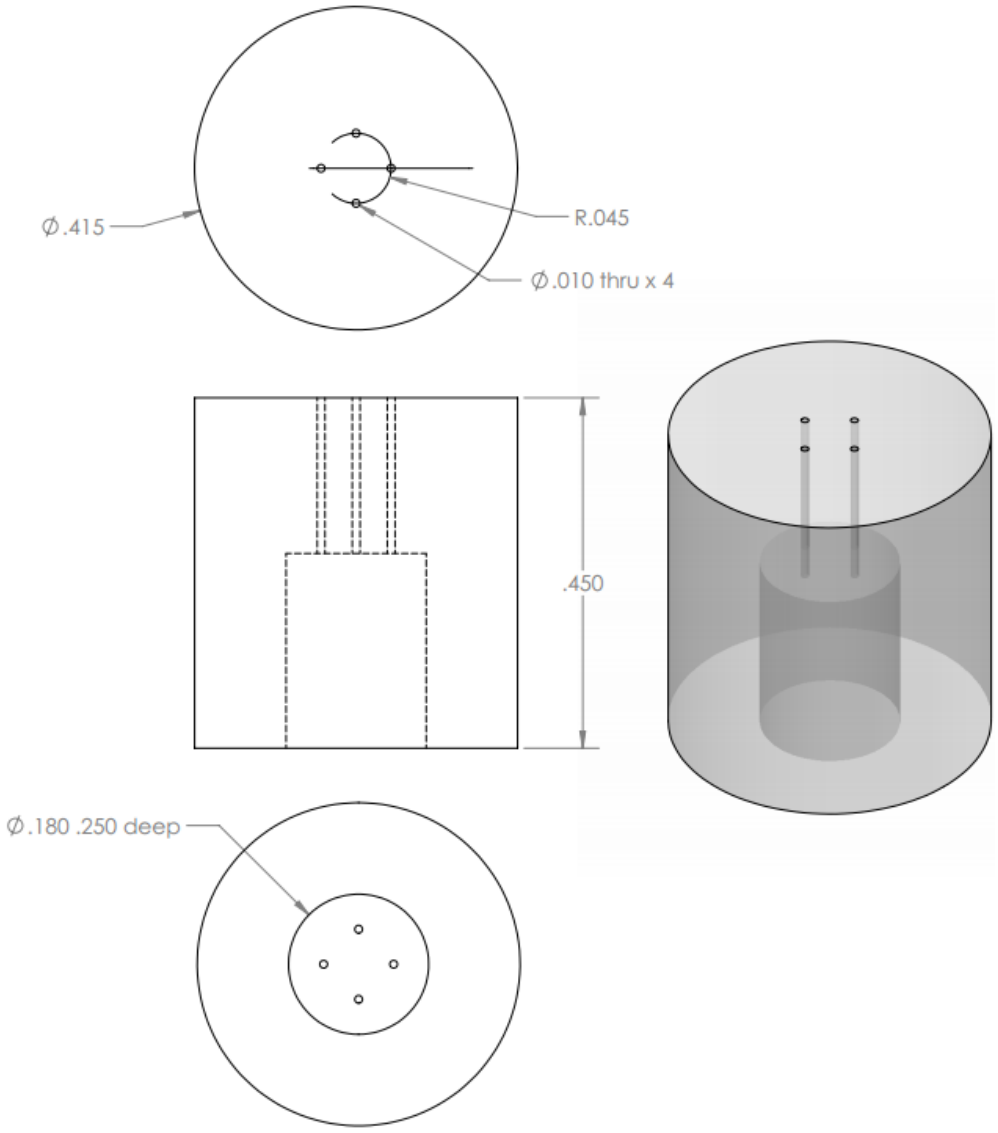

Figure A.15: Stycast cap for our cryogenic feedthrough. Each cap allows four wires to pass through into the vacuum space.

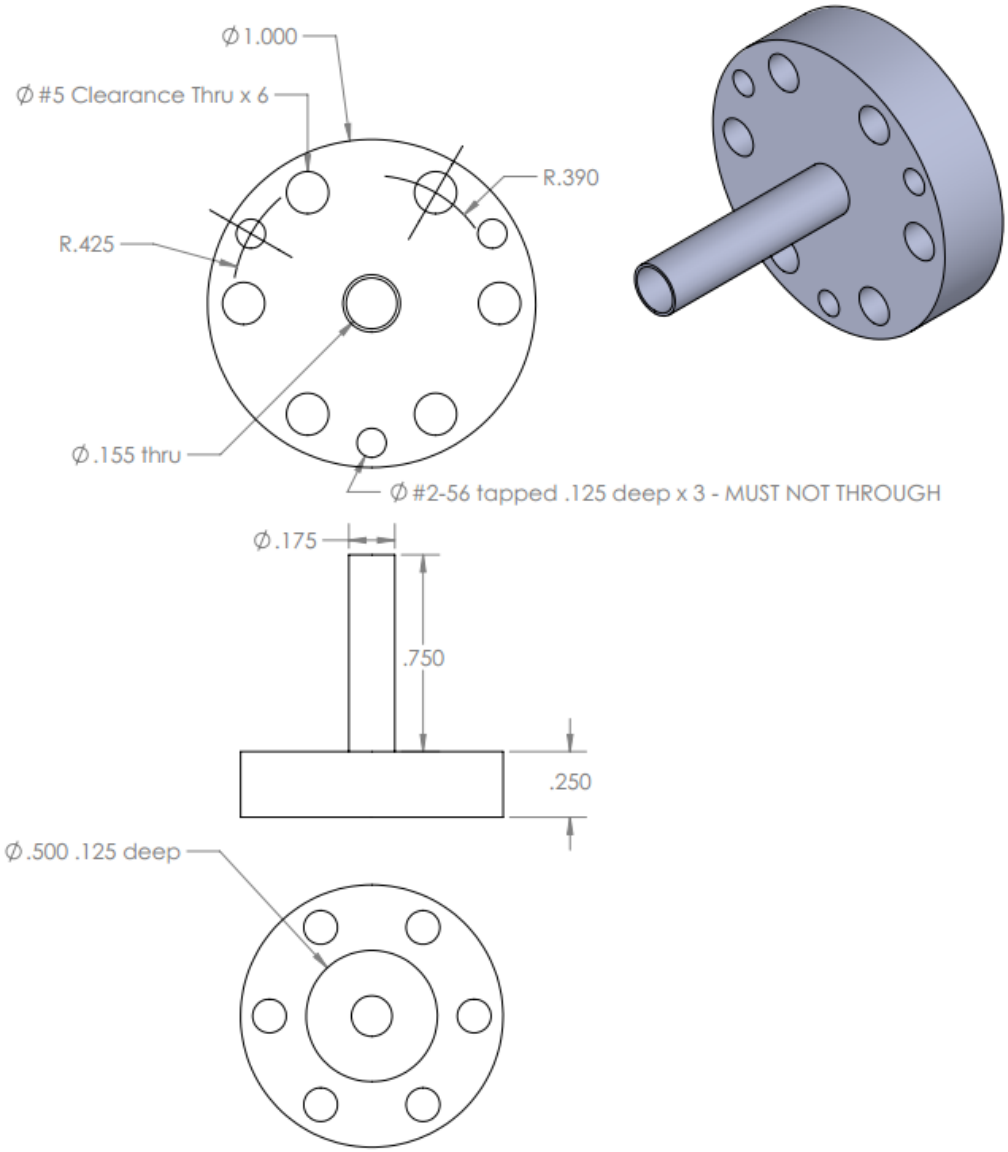

Figure A.16: Stainless steel flange that connects the cryogenic feedthrough to the 4K plate on the top of the vacuum can.

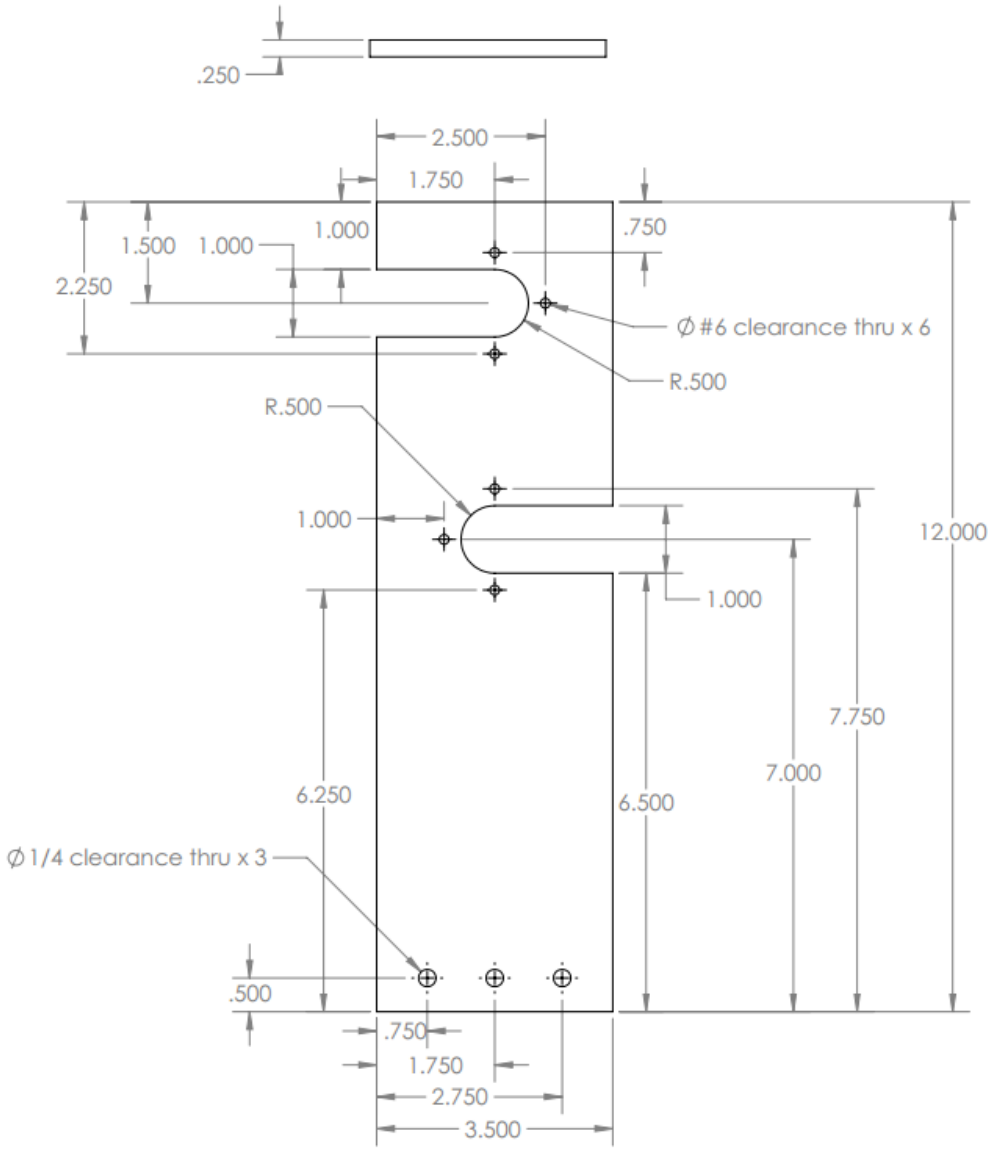

Figure A.17: Vertical stainless steel plate on which we mounted our room-temperature hermetic feedthroughs at the top of the cryostat. This plate holds two assemblies that each have six coaxial feedthroughs.

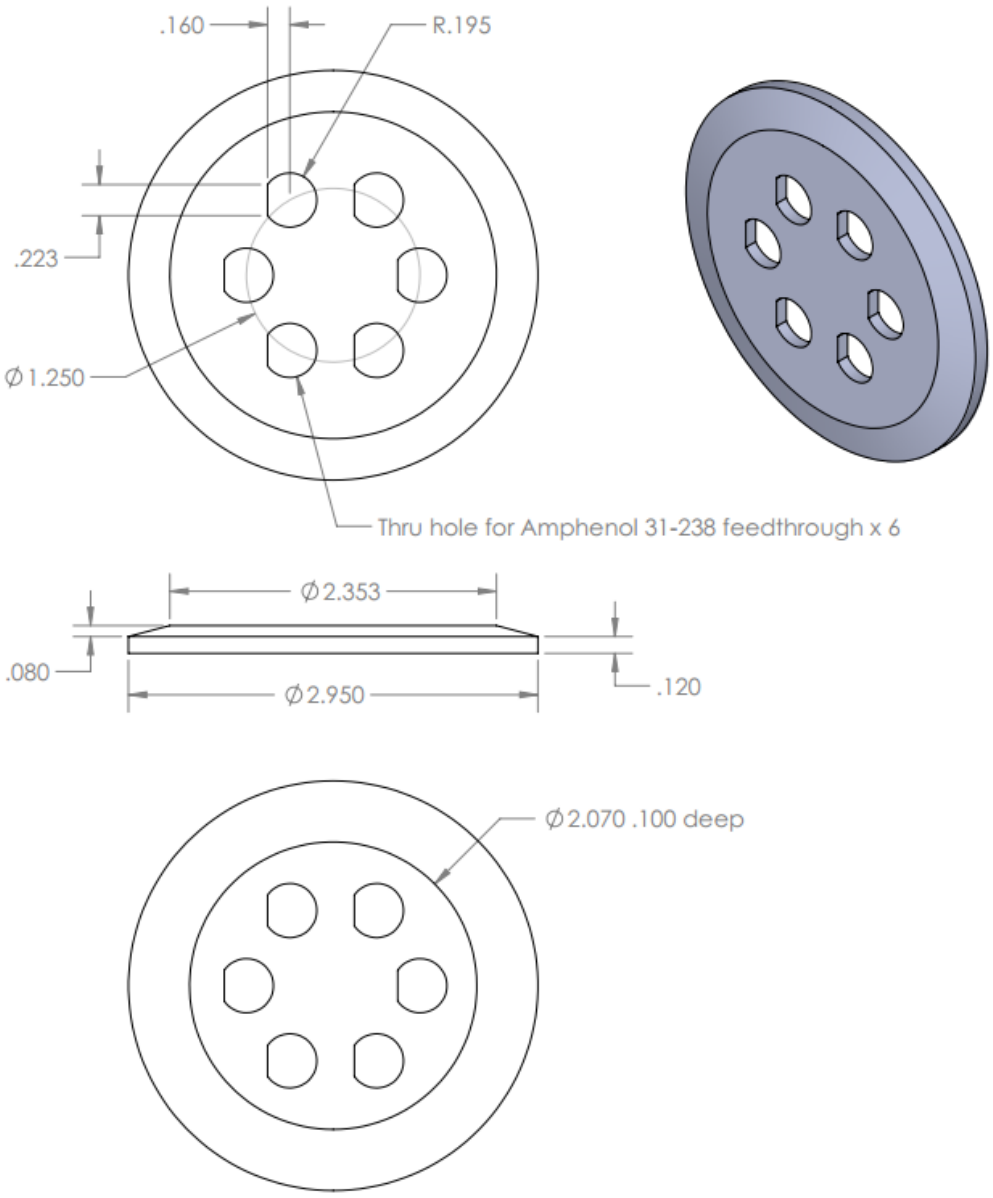

Figure A.18: Front of a room-temperature hermetic feedthrough assembly with holes for six coaxial feedthroughs.

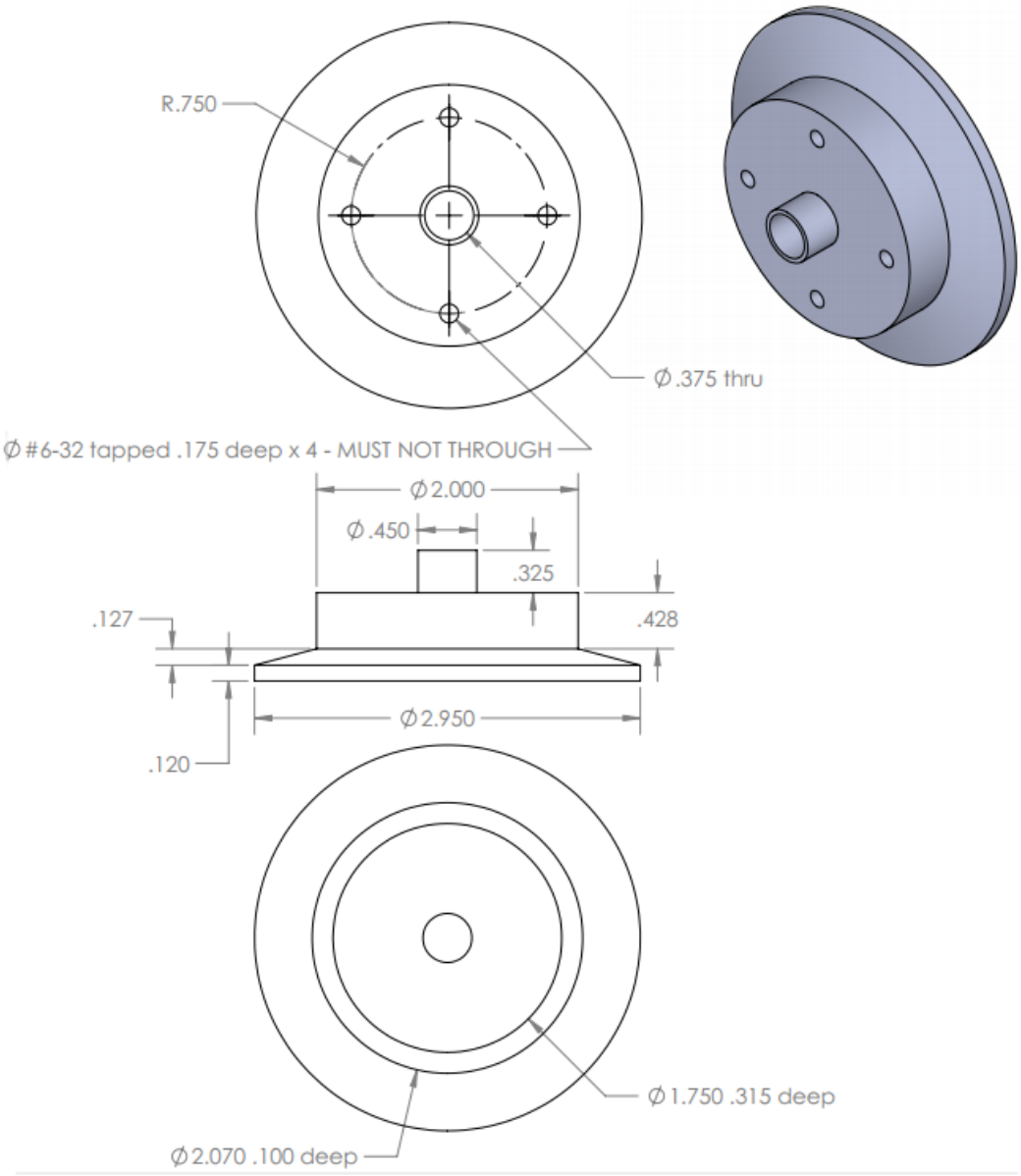

Figure A.19: Back end of a room-temperature hermetic feedthrough assembly. The front and back ends are sealed with a rubber o-ring. A flexible bellows hose is welded to the small-diameter protrusion.

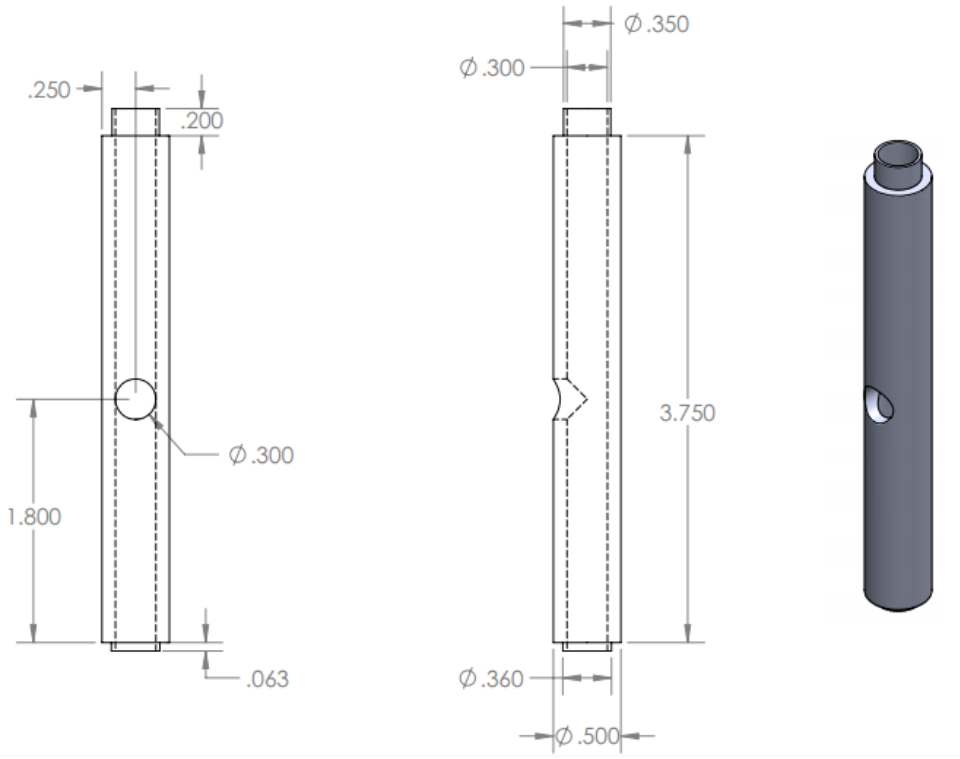

Figure A.20: Stainless steel tube at which the flexible bellows hoses terminate. The hoses, which come from the room-temperature hermetic feedthroughs, are welded to the top and middle of this piece. A KF-16 flange is welded to the bottom of the tube; this allows us to easily connect it to the dewar space.

BIBLIOGRAPHY

[1] A. Cavagna, "Supercooled liquids for pedestrians," *Phys. Reports*, vol. 476, p. 51124, 2009.

[2] R. Bohmer, K. Ngai, C. Angell, and D. Plazek, "Nonexponential relaxations in strong and fragile glass formers," *J. Chem. Phys.*, vol. 99, p. 4201, 2009.

[3] C. Angell, "Entropy and fragility in supercooling liquids," *J. Res. Nat. Inst. Stand. Technol.*, vol. 102, p. 171, 1997.

[4] V. Lubchenko and P. Wolynes, "Theory of structural glasses and supercooled liquids," *Ann. Rev. Phys. Chem.*, vol. 58, p. 235, 2007.

[5] M. Ediger, C. Angell, and S. Nagel, "Supercooled liquids and glasses," *J. Phys. Chem.*, vol. 100, p. 13200, 1996.

[6] G. Tarjus, S. Kivelson, Z. Nussinov, and P. Viot, "The frustration-based approach of supercooled liquids and the glass transition: A review and critical assessment," *J. Phys.: Condens. Matt.*, vol. 17, p. R1143, 2005.

[7] W. Kauzmann, "The nature of the glassy state and the behavior of liquids at low temperatures," *Chem. Rev.*, vol. 43, p. 219, 1948.

[8] S. Havriliak and S. Negami, "A complex plane representation of dielectric and mechanical relaxation processes in some polymers," *Polymer*, vol. 8, p. 161, 1967.

[9] H. Casimir and F. Du Pre, "Note on the thermodynamic interpretation of paramagnetic relaxation phenomena," *Physica*, vol. 5, p. 507, 1938.

[10] D. Davidson and R. Cole, "Dielectric relaxation in glycerol, propylene glycol, and n-propanol," *J. Chem. Phys.*, vol. 19, p. 1484, 1951.

[11] K. Cole and R. Cole, "Dispersion and absorption in dielectrics i. alternating current characteristics," *J. Chem. Phys.*, vol. 9, p. 341, 1941.

[12] S. Havriliak Jr. and S. Havriliak, "Results from an unbiased analysis of nearly 1000 sets of relaxation data," *J. Non-Cryst. Solids*, vol. 172, p. 294, 1994.

[13] R. Kohlrausch, "Theorie des elektrischen ruckstandes in der leidner flasche," *Annelen der Physik und Chemie (Poggendorff)*, vol. 91, p. 179, 1854.

[14] F. Alvarez, A. Alegria, and J. Colmenero, "Relation between the time-domain kohlrausch-williams-watts and frequency-domain havriliak-negami relaxation functions," *Phys. Rev. B*, vol. 44, p. 7306, 1991.

[15] K. Binder and A. Young, "Spin glasses: Experimental facts, theoretical concepts, and open questions," *Rev. Mod. Phys.*, vol. 58, p. 801, 1986.

[16] C. Mulder, A. van Duyneveldt, and J. Mydosh, "Susceptibility of the cumn spin-glass: Frequency and field dependences," *Phys. Rev. B*, vol. 23, p. 1384, 1981.

[17] S. Nagata, P. Keesom, and H. Harrison, "Low-dc-field susceptibility of cumn spin glass," *Phys. Rev. B*, vol. 19, p. 1633, 1979.

[18] D. Huser, L. Wenger, A. van Duyneveldt, and J. Mydosh, "Dynamical behavior of the susceptibility around the freezing temperature in (eu,sr)s," *Phys. Rev. B*, vol. 27, p. 3100, 1983.

[19] A. Dirkmaat, D. Huser, G. Nieuwenhuys, J. Mydosh, P. Kettler, and M. Steiner, "Frequency dependence of the ac susceptibility in the random anisotropy system dy(pv)o4," *Phys. Rev. B*, vol. 36, p. 352, 1987.

[20] C. Dekker, A. Arts, H. de Wijn, A. van Duyneveldt, and J. Mydosh, "Activated dynamics in a two-dimensional ising spin glass: Rb2cu(1-x)coxf4," *Phys. Rev. B*, vol. 40, p. 11243, 1989.

[21] L. Berthier and G. Biroli, "Theoretical perspective on the glass transition and amorphous materials," *Rev. Mod. Phys.*, vol. 83, p. 587, 2011.

[22] T. Castellini and A. a. Cavagna, "Spin glass theory for pedestrians," *J. Stat. Mech.*, vol. 2005, p. P05012, 2005.

[23] A. Morgownik and J. Mydosh, "The high-temperature spin-glass susceptibility: Determination of the local magnetic exchange," *Solid State Comm.*, vol. 47, p. 321, 1983.

[24] W. De Roeck and F. Hueveneers, "Scenario for delocalization in translation-invariant systems," *Phys. Rev. B*, vol. 90, p. 165137, 2014.

[25] D. Huse and R. Nandkishore, "Many-body localization and thermalization in quantum statistical mechanics," *Ann. Rev. Condens. Matt.*, vol. 2015, p. 1, 2015.

[26] P. Anderson, "Absence of diffusion in certain random lattices," *Phys. Rev.*, vol. 109, p. 1492, 1958.

[27] J. Hickey, S. Genway, and J. Garrahan, "Signatures of many-body localisation in a system without disorder and the relation to the glass transition," *arXiv*, p. 1405.5780, 2014.

[28] M. Schiulaz and M. Muller, "Ideal quantum glass transitions: Localization without quenched disorder," *AIP Conf. Proc.*, vol. 1610, p. 11, 2014.

[29] T. Grover and M. Fisher, "Quantum disentangled liquids," *J. Stat. Mech.*, vol. 2014, p. P10010, 2014.

[30] B. Chakraborty, D. Das, and J. Kondev, "Topological jamming and the glass transition in a frustrated system," *Eur. Phys. J. E*, vol. 9, p. 227, 2002.

[31] O. Cepas and B. Canal, "Heterogeneous freezing in a geometrically frustrated spin model without disorder: Spontaneous generation of two timescales," *Phys. Rev. B*, vol. 86, p. 024434, 2012.

[32] R. G. Palmer, D. Stein, E. Abrahams, and P. Anderson, "Models of hierarchically constrained dynamics for glassy relaxation," *Phys. Rev. Lett.*, vol. 53, p. 958, 1984.

[33] R. Roth, "Pyrochlore-type compounds containing double oxides of trivalent and tetravalent ions," *J. Res. Nat. Bur. Stand.*, vol. 56, p. 17, 1956.

[34] J. Gardner, M. Gingras, and E. Greeden, "Magnetic pyrochlore oxides," *Rev. Mod. Phys.*, vol. 82, p. 53, 2010.

[35] T. Yavors'kii, T. Fennell, M. Gingras, and S. Bramwell, "Dy2ti2o7: A test case for emergent clusters in a frustrated magnet," *Phys. Rev. Lett.*, vol. 101, p. 037204, 2008.

[36] H. Fukazawa, R. Melko, R. Higashinaka, Y. Maeno, and M. Gingras, "Magnetic anisotropy of the spin-ice compound dy2ti2o7," *Phys. Rev. B*, vol. 65, p. 054410, 2002.

[37] J. Snyder, B. Ueland, J. Slusky, H. Karunadasa, R. Cava, and P. Schiffer, "Low-temperature spin freezing in the dy2ti2o7 spin ice," *Phys. Rev. B*, vol. 69, p. 064414, 2004.

[38] D. Flood, "Magnetization and magnetic entropy of dy2ti2o7," *J. Appl. Phys.*, vol. 45, p. 4041, 1974.

[39] S. Rosenkranz, A. Ramirez, A. Hayashi, R. Cava, R. Siddharthan, and B. Shastry, "Crystal-field interaction in the pyrochlore magnet ho2ti2o7," *J. Appl. Phys.*, vol. 87, p. 5914, 2000.

[40] A. Ramirez, A. Hayashi, R. Cava, R. Siddharthan, and B. Shastry, "Zero-point entropy in 'spin ice'," *Nature*, vol. 399, p. 333, 1999.

[41] D. Morris, D. Tennant, S. Grigera, B. Klemke, C. Castelnovo, R. Moessner, C. Czternasty, M. Meissner, K. Rule, J.-U. Hoffman, K. Kiefer, S. Gerischer, D. Slobinsky, and R. Perry, "Dirac strings and magnetic monopoles in the spin ice dy2ti2o7," *Science*, vol. 326, p. 411, 2009.

[42] B. Klemke, M. Meissner, P. Strehlow, K. Kiefer, S. Grigera, and D. Tennant, "Thermal relaxation and heat transport in the spin ice material dy2ti2o7," *J. Low Temp. Phys.*, vol. 163, p. 345, 2011.

[43] R. Higashinaka, H. Fukazawa, D. Yanagishima, and Y. Maeno, "Specific heat of dy2ti2o7 in magnetic fields: Comparison between single-crystalline and polycrystalline data," *J. Phys. Chem. Solids*, vol. 63, p. 1043, 2002.

[44] D. Pomaranski, L. Yaraskavitch, S. Meng, K. Ross, H. Noad, H. Dabkowska, B. Gaulin, and J. Kycia, "Absence of pauling's residual entropy in thermally equilibrated dy2ti2o7," *Nat. Phys.*, vol. 9, p. 353, 2013.

[45] T. Fennell, O. Petrenko, B. Fak, S. Bramwell, M. Enjalran, T. Yavorsk'ii, M. Gingras, R. Melko, and G. Balakrishnan, "Neutron scattering investigation of the spin ice state in dy2ti2o7," *Phys. Rev. B.*, vol. 70, p. 134408, 2004.

[46] T. Fennell, O. Petrenko, B. Fak, J. Gardner, S. Bramwell, and B. Ouladdiaf, "Neutron scattering studies of the spin ices ho2ti2o7 and dy2ti2o7 in applied magnetic field," *Phys. Rev. B.*, vol. 72, p. 224411, 2005.

[47] L. Pauling, "The structure and entropy of ice and of other crystals with

some randomness of atomic arrangement," *J. Am. Chem. Soc.*, vol. 57, p. 2680, 1935.

[48] W. Giauque and J. Stout, "The entropy of water and the third law of thermodynamics. the heat capacity of ice from 15 to 273 degrees k," *J. Am. Chem. Soc.*, vol. 58, p. 1144, 1936.

[49] C. Henley, "Power-law spin correlations in pyrochlore antiferromagnets," *Phys. Rev. B*, vol. 71, p. 014424, 2005.

[50] L. Jaubert and P. Holdsworth, "Magnetic monopole dynamics in spin ice," *J. Phys.: Condens. Matt.*, vol. 23, p. 164222, 2011.

[51] R. Youngblood and J. Axe, "Polarization fluctuations in ferroelectric models," *Phys. Rev. B*, vol. 23, p. 232, 1980.

[52] R. Melko, B. den Hertog, and M. Gingras, "Long-range order at low temperatures in dipolar spin ice," *Phys. Rev. Lett.*, vol. 87, p. 067203, 2001.

[53] S. Dunsiger, A. Aczel, C. Arguello, H. Dabkowska, A. Dabkowski, M.-H. Du, T. Goko, B. Javanparast, T. Lin, F. Ning, H. Noad, D. Singh, T. Williams, Y. Uemura, M. Gingras, and G. Luke, "Spin ice: Magnetic excitations without monopole signatures using muon spin rotation," *Phys. Rev. Lett.*, vol. 107, p. 207207, 2011.

[54] K. Matsuhira, Z. Hiroi, T. Tayama, S. Takagi, and T. Sakakibara, "A new macroscopically degenerate ground state in the spin ice compound dy2ti2o7 under a magnetic field," *J. Phys.: Condens. Matt.*, vol. 14, p. 2002, 2002.

[55] Y. Tabata, H. Kadowaki, Z. Hiroi, N. Aso, E. Ressouche, and B. Fak, "Kagome ice state in the dipolar spin ice dy2ti2o7," *Phys. Rev. Lett.*, vol. 97, p. 257205, 2006.

[56] R. Higashinaka, H. Fukazawa, K. Deguchi, and Y. Maeno, "Low temperature specific heat of dy2ti2o7 in the kagome ice state," *J. Phys. Soc. Japan*, vol. 73, p. 2004, 2004.

[57] M. Saito, R. Higashinaka, and Y. Maeno, "Magnetodielectric response of the spin-ice dy2ti2o7," *Phys. Rev. B*, vol. 72, p. 2005, 2005.

[58] J. Snyder, J. Slusky, R. Cava, and P. Schiffer, "Dirty spin ice: The effect of dilution on spin freezing in dy2ti2o7," *Phys. Rev. B*, vol. 66, p. 064432, 2002.

[59] L. Bovo, J. Bloxsom, D. Prabhakaran, G. Aeppli, and S. Bramwell, "Brownian motion and quantum dynamics of magnetic monopoles in spin ice," *Nat. Comm.*, vol. 4, p. 1535, 2013.

[60] K. Matsuhira, C. Paulsen, E. LHotel, C. Sekine, Z. Hiroi, and S. Takagi, "Spin dynamics at very low temperature in spin ice dy2ti2o7," *J. Phys. Soc. Japan*, vol. 80, p. 123711, 2011.

[61] L. Yaraskavitch, H. Revell, S. Meng, K. Ross, H. Noad, H. Dabkowska, B. Gaulin, and J. Kycia, "Spin dynamics in the frozen state of the dipolar spin ice material dy2ti2o7," *Phys. Rev. B*, vol. 85, p. 020410, 2012.

[62] K. Matsuhira, Y. Hinatsu, and T. Sakakibara, "Novel dynamical magnetic properties in the spin ice compound dy2ti2o7," *J. Phys.: Condens. Matt.*, vol. 13, p. L737, 2001.

[63] H. Revell, L. Yaraskavitch, J. Mason, K. Ross, H. Noad, H. Dabkowska, B. Gaulin, P. Henelius, and J. Kycia, "Evidence of impurity and boundary effects on magnetic monopole dynamics in spin ice," *Nat. Phys.*, vol. 9, p. 34, 2013.

[64] S. Giblin, S. Bramwell, P. Holdsworth, D. Prabhakaran, and I. Terry, "Creation and measurement of long-lived magnetic monopole currents in spin ice," *Nat. Phys.*, vol. 7, p. 252, 2011.

[65] B. den Hertog and M. Gingras, "Dipolar interactions and origin of spin ice in ising pyrochlore magnets," *Phys. Rev. Lett.*, vol. 84, p. 3430, 2000.

[66] C. Castelnovo and S. Sondhi, "Magnetic monopoles in spin ice," *Nature*, vol. 451, p. 42, 2008.

[67] Y. Levin, "Electrostatic correlations: From plasma to biology," *Rep. Prog. Phys.*, vol. 65, p. 1577, 2002.

[68] C. Castelnovo, R. Moessner, and S. Sondhi, "Debye-huckel theory for spin ice at low temperature," *Phys. Rev. B*, vol. 84, p. 144435, 2011.

[69] L. Jaubert and P. Holdsworth, "Signature of magnetic monopole and dirac dynamics in spin ice," *Nat. Phys.*, vol. 5, p. 258, 2009.

[70] H. Takatsu, K. Goto, H. Otsuka, R. Higashinaka, K. Matsubayashi, Y. Uwatoko, and H. Hadowaki, "Ac susceptibility of the dipolar spin ice dy2ti2o7: Experiments and monte carlo simulations," *J. Phys. Soc. Japan*, vol. 82, p. 104710, 2013.

[71] I. Ryzhkin, "Magnetic relaxation in rare-earth oxide pyrochlores," *J. Exp. Th. Phys.*, vol. 101, p. 481, 2005.

[72] C. Jaccard, "Thermodynamics of irreversible processes applied to ice," *Phys. Kondenx. Mat.*, vol. 3, p. 99, 1964.

[73] I. Ryzhkin and R. Whitworth, "The configurational entropy in the jaccard theory of the electrical properties of ice," *J. Phys.: Condens. Matt.*, vol. 9, p. 395, 1997.

[74] S. Bramwell, "Generalized longitudinal susceptibility for magnetic monopoles in spin ice," *Phil. Trans. R. Soc. A*, vol. 370, p. 5738, 2012.

[75] F. Pobell, ed., *Matter and Methods at Low Temperatures*. Springer, 2nd ed., 1996.

[76] D. Betts, *Refrigeration and Thermometry Below One Kelvin*. Cambridge Univ. Press, 1989.

[77] N. Balshaw, ed., *Practical Cryogenics: An Introduction to Laboratory Cryogenics*. Oxford Instruments.

[78] C. Ho, M. Ackerman, K. Wu, T. Havill, R. Bogaard, R. Matula, S. Oh, and H. James, "Electrical resistivity of ten selected binary alloy systems," *J. Phys. Chem. Ref. Data*, vol. 12, p. 183, 1983.

[79] S. Bramwell, S. Giblin, S. Calder, R. Aldus, D. Prabhakaran, and T. Fennell, "Measurement of the charge and current of magnetic monopoles in spin ice," *Nature*, vol. 461, p. 956, 2009.

[80] D. Griffiths, *Introduction to Electrodynamics*. Addison Wesley, 3rd ed., 1999.

[81] M. Harris, S. Bramwell, D. McMorrow, T. Zeiske, and K. Godfrey, "Geometrical frustration in the ferromagnetic pyrochlore ho2ti2o7," *Phys. Rev. Lett.*, vol. 79, p. 2554, 1997.

[82] M. Harris, S. Bramwell, T. Zeiske, D. McMorrow, and P. King, "Magnetic structures of highly frustrated pyrochlores," *J. Mag. Mag. Mat.*, vol. 177, p. 757, 1998.

[83] T. Fennell, P. Deen, A. Wildes, K. Schmalzl, D. Prabhakaran, A. Boothroyd, R. Aldus, D. McMorrow, and S. Bramwell, "Magnetic coulomb phase in the spin ice ho2ti2o7," *Science*, vol. 326, p. 415, 2009.

[84] S. Bramwell, M. Harris, B. den Hertog, M. Gingras, J. Gardner, D. McMorrow, A. Wildes, A. Cornelius, J. Champion, R. Melko, and T. Fennell, "Spin correlations in ho2ti2o7: A dipolar spin ice system," *Phys. Rev. Lett.*, vol. 87, p. 047205, 2001.

[85] A. Cornelius and J. Gardner, "Short-range magnetic interactions in the spin-ice compound ho2ti2o7," *Phys. Rev. B*, vol. 64, p. 060406, 2001.

[86] J. Rau and M. Gingras, "How quantum are classical spin ices?," *arXiv*, p. 1503.04808, 2015.

[87] L. Balents, "Spin liquids in frustrated magnets," *Nature*, vol. 464, p. 199, 2010.

[88] M. Gingras and P. McClarty, "Quantum spin ice: a search for gapless quantum spin liquids in pyrochlore magnets," *Rep. Prog. Phys.*, vol. 77, p. 056501, 2014.